TRAUMA-INDUCED ALTERATIONS OF CEREBRAL VESSEL MECHANICS AND MICROSTRUCTURE

by

Matthew Israel Converse

A dissertation submitted to the faculty of
The University of Utah
in partial fulfillment of the requirements for the degree of

Doctor of Philosophy

Department of Mechanical Engineering

The University of Utah

August 2018

The University of Utah Graduate School

STATEMENT OF DISSERTATION APPROVAL

The dissertation of **Matthew Israel Converse**

has been approved by the following supervisory committee members:

Kenneth L. Monson	, Chair	**12/21/2017** Date Approved
Brittany Coats	, Member	**12/21/2017** Date Approved
Michael W. Czabaj	, Member	**12/21/2017** Date Approved
Jeffrey A. Weiss	, Member	**12/21/2017** Date Approved
S. Michael Yu	, Member	**12/21/2017** Date Approved

and by **Timothy A. Ameel** , Chair/Dean of

the Department/College/School of **Mechanical Engineering**

and by David B. Kieda, Dean of The Graduate School.

ABSTRACT

The cerebrovasculature is essential to maintaining health of the brain; however, traumatic brain injuries (TBI) can injure or cause dysfunction of the vasculature, putting neural tissue at risk. While dysfunction is a known consequence of the post-trauma biochemical cascade, stretch-induced structural damage to the vascular extracellular matrix (ECM) may also contribute. The objective of the present work is to characterize potentially treatable damage to the cerebrovascular ECM in TBI. Three *in vitro* studies characterize mechanical and structural alterations of isolated ovine middle cerebral arteries following a single overstretch. Results serve to guide a subsequent *in vivo* investigation of vascular damage in closed-head injury. In the first *in vitro* study, mechanical testing revealed a significant increase in axial and circumferential compliance of the arterial wall following axial overstretch. Biaxial data were subsequently fit with a microstructurally-motivated constitutive model of damage. A second study employed a recently developed collagen hybridizing peptide (CHP) to characterize molecular-level collagen damage, the first ever such study in blood vessels. Imaging and quantification of CHP showed that overstretch produced damage among fibers aligned with the direction of loading, that damage increased with overstretch severity, and that damage initiated just after the vessel reached maximum stiffness. These findings held true for both axial and circumferential overload. A third study investigated subfailure disruption of the intima as this has been implicated in the increased risk of stroke following blunt trauma. As with

collagen, intimal disruption occurred just after reaching maximum stiffness. Additional analysis showed that disruption included failure of both the internal elastic lamina (IEL) and endothelium. The threshold of failure did not change over four stages of development. In a final study, preliminary *in vivo* investigations were conducted to detect structural damage to the vascular wall in an ovine closed-head injury model. After significant refinement of procedures, cortical hemorrhage in the absence of skull fracture was successfully achieved by a left temporal blow with a captive bolt stunner. Neither collagen nor elastin damage was found among neighboring cortical vessels; however, investigations were limited. The combined *in vitro* studies of this dissertation elucidate the mechanical and microstructural changes to the vascular wall that may occur in head trauma. Additional work is needed to better detect and characterize the contribution of such damage in *in vivo* trauma.

To my incredibly supportive wife, Katie, who has made more sacrifices than I have to the completion of this work.

“Within the gospel of Jesus Christ there is room and place for every truth thus far learned by man or yet to be made known.”
James E. Talmage

TABLE OF CONTENTS

LIST OF TABLES

Tables

LIST OF FIGURES

Figures

ACKNOWLEDGMENTS

This work is the product of many people. Not just of scientific collaborators, but of many colleagues, family, and friends who have supported me along the way. To each I am indebted and for each I am grateful. I would like to particularly thank the following individuals and organizations for their valuable contributions:

- Dr. Ken Monson, my PhD advisor. I don't think I could have asked for a better mentor. He has demonstrated in word and deed that people are more important than projects, that optimism is the best anecdote to adversity, and that being teachable is the key to intelligence. He has always been there for me and I'm fortunate to call him my friend.
- Drs. Brittany Coats, Michael Yu, Jeff Weiss, and Michael Czabaj, my committee members. Each of them has been so supportive and giving of their time to mentor me along the way.
- Drs. Michael Yu and Yang Li, for developing and supplying CHP with led to the detection of collagen damage in Chapters 4 and 6.
- Dr. Kurt Albertine, Mar Janna Dahl, and their research team. In addition to providing the ovine tissue for the experiments in Chapters 4-5, they have graciously shared their surgery room, resources, and provided guidance for my studies in Chapter 6.
- Gary's Meats in Payson, UT and Tooele Valley Meats in Tooele, UT, for supplying lamb tissue for experiments conducted in Chapters 3-5.

- Dave Bell, who patiently mentored me when I was a new PhD student. He taught me how to carry out the experiments conducted in Chapter 3 and first observed intimal failure which led to the studies in Chapter 5.
- Ray Walther, Justin Ingram, Will Anderl, and Sameer Nandikar for their significant contributions to conducting/validating the experiments in Chapter 4.
- Kevin Nye, for conducting the experiments that led to my analysis in Chapter 5.
- Rumal Kaluarachi for technical assistance in Chapter 5.
- Stewart Yeoh, Farshad Mogharrabi, Abhidnya Patharkar, Noah Pearson, and Greg Boiczyk, for their hands-on assistance in conducting the experiments in Chapter 6.
- Nan-Wei Liu, for his friendship and example of being a life-long learner.
- My dear wife, Katie, to whom this dissertation is dedicated (though she probably isn't very interested in its contents). Somehow she let me drag her along for the ride. She has picked me up when I've been down, helped me find purpose in what I do, and given more of herself than I have to the completion of this work.
- My parents, Phil and Ruth Converse, who taught me the value of education and hard work. Their endless love and support have inspired me to do what I love.
- My in-laws, Mark and Susan Ross. They have kept me and my family afloat both physically and emotionally so that I could complete this work.
- My children, Maizie and Charlie, who are the motivation for what I do.
- Financial support was provided by an Integrated Sciences Award from the Primary Children's Medical Center Foundation and an internal seed grant from the University of Utah.

CHAPTER 1

INTRODUCTION

1.1 Motivation

Traumatic brain injury (TBI) is one of the major health care problems in the United States, contributing to nearly a third (30.5%) of all injury-related deaths [1]. An estimated 1.7 million people annually sustain a traumatic brain injury, and of these patients, approximately 50,000 die [1]. Those who do survive the initial head injury often suffer from neurological deficits.

While damage to the brain tissue is the fundamental concern in head injuries, nearly all significant TBIs include injury to the vasculature, and vascular damage puts neural tissue at risk. Vascular damage in head trauma is most commonly manifest as bleeding within the cranial vault, with contusion and intracranial hemorrhage being reported in 94% and 60% of fatally injured patients, respectively [2]. The incidence of subfailure vascular damage, or damage in the absence of hemorrhage, is more difficult to quantify; however, alteration of cerebral blood flow is a common outcome of all forms of head trauma [2-6].

The mechanisms behind nonhemorrhagic dysfunction, or the inability of vessels to properly regulate blood flow throughout the brain, are not well understood. While some dysfunction can be attributed to indirect effects from a perturbed biochemical

environment, experimental investigations suggest additional factors are also at play. Several animal models of TBI have been used to evaluate functional changes to intact vessels near sites of hemorrhage through the administration of vasoactive chemicals or pressure changes [7-15]. The majority of these have demonstrated dysfunction, suggesting changes to smooth muscle and endothelial cells. However, vessel behavior is the result of active (cells) and passive (extracellular matrix) elements working together. Therefore, damage to the extracellular matrix (ECM) likely also contributes to altered response.

Previous authors have suggested that damage to the ECM may directly contribute to vascular dysfunction [16]. However, to date, the majority of research on the effects of vessel deformation has focused on defining failure properties of the vasculature relevant to hemorrhage [17-21]. Little is known about the effect of subfailure deformations on vessel impairment. In the present work, the term 'subfailure deformation' denotes stretch levels that are below the ultimate failure of the tissue. In other words, subfailure damage may produce microstructural changes, but the tissue as a whole remains intact. In a blood vessel, subfailure damage could be synonymous with nonhemorrhagic levels of overstretch as the vascular wall likely remains impermeable to blood.

1.2 Hypothesis and objective

Given that vessels are torn and bleed in TBI, it follows that neighboring vessels also experience deformations that are severe yet insufficient to produce hemorrhage. We hypothesize that subfailure deformations in TBI disrupt structurally relevant constituents of the extracellular matrix and compromise a vessel's mechanical response**.** Little is

known about how vessels are injured or about how an initial event affects vascular function thereafter. This is a significant knowledge gap [3, 22] that inhibits the development of new preventive, diagnostic, and treatment strategies. Therefore, the objective of this study is to characterize vascular damage to the ECM produced by TBI. This will be done by a combination of *in vitro* and *in vivo* investigations in the sheep cerebrovasculature.

1.3 Overview of work

The overall goal of this work is to characterize damage to the cerebrovascular ECM produced by TBI. We accomplish this by first defining the nature of mechanical injury in experiments on isolated cerebral vessels. This investigation is broken down into three *in vitro* studies (Chapters 3-5) and their results serve to guide and interpret preliminary *in vivo* investigations in the fourth study (Chapter 6). In our first study (Chapter 3) we characterize the effect of a single subfailure axial overstretch on the mechanical properties of cerebral arteries while our second and third studies explore the effect on vessel microstructure. This includes defining relationships between overstretch magnitude and injury to the various structural components of the vessel wall, including the collagen (Chapter 4) and elastin (Chapter 5) microstructures responsible for vessel integrity. These *in vitro* investigations focus on axial (as opposed to circumferential) loading as it is hypothesized that blood vessels act as reinforcing fibers that align with the direction of loading. Although TBI occurs at a high rate, vessels are stretched quasi-statically as previous investigations have shown cerebral vessels to have no significant rate dependence over a strain rate range of more than four orders of magnitude [23].

Findings from these studies will then be used to identify and describe blood vessel damage in preliminary studies in a large animal model of TBI (Chapter 6). The animal model ultimately seeks to clarify the distribution of vessel damage over the cortical surface and its severity, and identify vessel types, sizes, and geometries that are most susceptible to injury. However, the scope of this initial investigation is to determine loading conditions that produce cortical hemorrhage in the absence of skull fracture and explore vascular damage in a few animals. These studies address important questions that will enable subsequent research addressing the persistence of vessel injury and the development of therapeutic strategies.

All studies are carried out in sheep cerebral arteries. Not only is this tissue readily available through a collaboration with a nearby lab (Albertine Lab, University of Utah), but advantages of this model over typical rodent models are numerous. These include a blunt impact to the intact head that results in coup and contrecoup contusion [24, 25], typical of human injury. The gyrencephalic brain of the sheep will also allow better translation of injury-related findings both from this study and from future studies directed at disease development and healing. The model is also important for direct study of blood vessels since the vessels on the brain surface are larger and more robust than those from smaller animals.

CHAPTER 2

BACKGROUND

2.1 Cerebral vessel anatomy

Blood is supplied to the brain through the two internal carotid and two vertebral arteries. The internal carotids enter the cranial cavity through the carotid canal while vertebral arteries enter the through the foramen magnum. Once there, these four arteries traverse the dura and arachnoid to enter the subarachnoid space where they are bathed in cerebral spinal fluid. The two vertebral arteries travel along the brain stem and unite to form the basilar artery. The basilar artery and two internal carotids anastomose to form the Circle of Willis. Originating from the Circle of Willis are the three paired arteries which supply blood to each hemisphere: the anterior, middle, and posterior cerebral arteries. These conducting arteries run along the cortical surface, branching and subdividing to form a complex network of smaller distributing arteries. These pass over and between the surfaces of various lobes of the brain (frontal, temporal, parietal, and occipital), following paths within and across sulci [26, 27]. Small penetrating vessels branch off from these pial, or surface, arteries at right angles, diving into the cortex and further subdividing until they join the capillary plexus [27-31].

Cortical capillaries drain into venules (small veins) that unite to form the cortical veins. These ultimately feed into the superior cerebral veins which drain the superior,

lateral, and medial surfaces of the hemispheres. Bridging veins traverse the arachnoid and dura, connecting the superior cerebral veins to the superior sagittal sinus. This large sinus follows the longitudinal fissure down the posterior surface of the brain where it meets with drainage from the deep sinuses. From there, blood drains through the base of the skull via the two internal jugular veins [32].

2.2 Cerebral vessel microstructure

The vasculature is generally divided into two main types: elastic and muscular. In general, elastic vessels are larger in diameter and lie closer to the heart. Among elastic arteries are the aorta, main pulmonary artery, common carotids, and common iliacs. In contrast, muscular arteries (coronaries, cerebrals, and femorals) are smaller and located along the periphery.

The location, orientation, and size of the main components within the vascular wall are now described in some detail. Emphasis is made on the most mechanically relevant constituents, such as collagen, elastin, and smooth muscle cells. The details of other components which do not contribute significantly to the vascular mechanical response (fibroblasts, fibrocytes, proteoglycans, etc.) can be found in other works [33].

2.2.1 Intima

The wall of veins and arteries is made up of three principal layers known as the intima, the media, and the adventitia (Figure 2.1). The intima is the innermost layer and forms the lumen – the cavity through which blood flows. Endothelial cells lie on the inner surface of the intima and are directly in contact with flowing blood.

2.2.2 Media

The media is the middle layer in blood vessels. It is separated from the intima by a fenestrated sheet of elastin known as the internal elastic lamina. The media is primarily made up of smooth muscle cells imbedded in a network of collagen and elastin (Figure 2.2). The smooth muscle cells are typically 100 μm long and about 5 μm in diameter [34]. These cells, along with the elastic bundles of collagen fibers, have a helical yet nearly circumferential orientation [33]. In elastic arteries the smooth muscle is organized into 5-15 μm thick concentric layers, each separated by a thin 3 μm fenestrated sheet of elastin [35]. The media of muscular arteries is still comprised of concentric layers of smooth muscle; however, there are few if any elastic fibers.

2.2.3 Adventitia

The adventitia is the outermost layer and consists primarily of thick bundles of collagen fibers. These fibers are arranged helically in two main fiber families with large deviations [36, 37]. At significant levels of strain, the fibers straighten and become stiff – preventing the artery from overstretching [38]. The adventitia comprises 10% of the vascular wall thickness in elastic arteries and 50% in muscular arteries [39].

2.3 Cerebral artery passive mechanics

In contrast to standard engineering materials (steel, aluminum, etc.) which undergo small, linear deformations prior to yield, most biological tissues exhibit a nonlinear behavior over large deformations. These deformations are commonly plotted on a stress-stretch curve where stretch (λ) is defined as the current length divided by the

reference length. The stress-stretch curve often begins with a nonlinear, nearly exponential region followed by a linear region and the yield point (Figure 2.3). The nonlinear portion is commonly referred to as the 'toe-region' and the slope of the linear portion just before the yield point is referred to as the 'maximum stiffness', 'maximum modulus', or 'tangential modulus.'

2.4 Mechanical changes following subfailure axial deformation

We now review what is known about the effect of supraphysiological axial deformations on the mechanical properties of blood vessels – specifically, subfailure levels of deformation. Emphasis is made on axial deformation because it is believed that as brain tissue deforms, vessels align axially with the direction of deformation. The literature relevant to this topic is reviewed with priority given to cerebral blood vessels. However, since minimal research has been done in this area, publications on similar soft tissues, namely ligaments and tendons, have also been surveyed. Then, in an effort to explain the mechanisms behind an altered soft tissue response, postdeformation microstructural changes are also examined in Section 2.5. Again, this is done primarily in blood vessels with supplementary findings from ligaments and tendons.

2.4.1 Blood vessels

2.4.1.1 Elastic properties

It appears that only one researcher has reported changes in vascular mechanical properties following subfailure axial deformation. Monson characterized the elastic properties of human cerebral arteries which had been surgically removed from adult

brains during temporal lobectomies [40]. He showed that the toe-region of the load-displacement curve elongated after the vessel was stretched beyond its *in vivo* length. In fact, this behavior was manifest repeatedly as the vessel was submitted to successive increases in displacement (Figure 2.4). Each curve in Figure 2.4 represents the first loading phase of a series of 10 cycles and each subsequent series was taken to a slightly larger target displacement. This process resulted in an elongation of the toe-region in every successive series, although the maximum modulus remained relatively constant throughout the test.

2.4.1.2 Viscoelastic properties

To date, no research has reported the effects of axial deformation on the viscoelastic properties of blood vessels.

2.4.2 Ligaments and tendons

Due to the scarcity of information on the effects of subfailure damage on vascular mechanical properties, relevant literature on ligaments and tendons has also been included. It is hoped that such literature will reveal valuable insights into the behavior of the vasculature since ligaments and tendons are composed of similar microstructural constituents.

2.4.2.1 Elastic properties

Multiple authors have reported changes in ligament laxity (elongated toe-region) and stiffness which can be compared with the observations in blood vessels by Monson

[40]. Specifically, authors have quantified the length of the toe-region, the maximum modulus, and failure properties.

2.4.2.1.1 Toe-region

One study by Panjabi et al. examined the behavior of rabbit ACLs following a single stretch to 80% of the tissue's ultimate tensile strength ($\lambda \approx 1.2$). This resulted in an elongated toe-region in the ligament [41]. Two other studies went a step further by examining changes in elastic behavior over multiple deformations, one in a rat MCL [42] and another in a rat spinal segment [43]. As did Monson [40], these studies showed increased tissue laxity following subsequent stretches of increasingly greater magnitudes. More recently this same result has also been reported in tendons [44].

2.4.2.1.2 Maximum modulus

The same two studies that examined ligament behavior over repeated deformations also commented on changes in the maximum modulus. Similar to Monson, these studies subjected the tissue to a series of deformations, each to an increasingly greater stretch level. Both papers reported a steady decrease in the maximum modulus with successive increases in strain [42, 43]. Panjabi et al. also reported a postdamage decrease in the rabbit ACL stiffness in two of his studies [41, 45], although changes were only statistically significant in the former paper.

2.4.2.1.3 Failure load, failure deformation, and energy until failure

Using rabbit ACLs, Panjabi et al. showed that the metrics of failure load, deformation at failure, and the energy until failure remained constant after a single subfailure stretch [41]. However, changes were seen in failure deformation and failure energy when the damage was induced at higher strain rates (see Section 2.4.3). At quasi-static deformation Provenzano et al. reported that the ultimate tensile strength (UTS) of the rat MCL decreased following successive increases in strain [42]. Since the UTS was measured as engineering strain, it could similarly be stated that they reported a decrease in the failure load. The reason for the contradiction between this and Panjabi's report of a constant failure load is unclear, especially since Panjabi never saw a change in failure load over a wide range of damage rates [45].

2.4.2.2 Viscoelastic properties

While no research has been done to date on how arterial viscoelastic properties change following damage, a few studies have examined this in ligaments [45, 46] and tendons [44]. During relaxation and cyclic tests these authors all showed a decrease in postdamage stress magnitudes. This, however, seems to correlate more with changes in elastic properties (elongated toe-region, decreased modulus) than changes in viscoelastic properties. One author did evaluate the rate of decay during relaxation tests. It was shown that the decay rate decreased following damage, and that it continued to decrease after subsequent distractions, each of greater magnitude [44].

2.4.3 Effect of rate on subfailure damage

While most of the previously mentioned studies were performed at relatively slow (or quasi-static rates), traumatic brain injuries, and for that matter ligament injuries, inherently occur at high strain rates. It is therefore imperative to understand how an increased strain rate may affect the preceding findings. To date, no one has investigated the effect that the rate of subfailure damage has on subsequent blood vessel properties; however, one author has done so in ligaments [45]. Two groups of rabbit ACLs were subjected to a single subfailure strain, one at a quasi-static rate (5%/s) and the other at a high strain rate (10,000%/s). Following overstretch, the mechanical properties of both groups were evaluated. Relative to the ligament that underwent a quasi-static damage, the high speed damage resulted in a more elongated toe-region, an increase in the failure deformation, a decrease in the energy until failure, but no change in the failure load.

2.4.4 Summary of changes in mechanical properties

The changes in soft tissue mechanical properties following quasi-static, subfailure overstretches are summarized in Table 2.1. In both blood vessels and ligaments/tendons the length of the toe-region increases after damage, but there is a discrepancy in how the maximum modulus is altered. Multiple ligament studies have reported a decrease in the maximum modulus while the one study on blood vessels reported no change. Possible explanations for this discrepancy may be differences in the failure rates, the data analysis approach, the levels of deformation, or inherent differences in the two tissues. Furthermore, only a single study has been done in blood vessels and one of the ligament studies could not show a statistically significant decrease in the maximum modulus. It

should also be noted that no research has been done to quantify changes to the viscoelastic or the failure properties of blood vessels following a subfailure distraction.

2.5 Microstructural changes following subfailure axial deformation

In order to understand the possible mechanisms behind postdamage changes in mechanical properties, it is essential to examine postdamage changes in microstructure – for it is structure that defines function. As with the previous section on mechanical properties, the review of microstructural changes in blood vessels is followed by a review of the relevant findings in ligaments.

2.5.1 Blood vessels

It is evident from the literature that subfailure levels of overstretch can result in microscale damage to the structure of the vascular wall. Stemper et al. showed that human common carotid arteries experience multiple structural subfailures prior to catastrophic failure [47-49]. All of the reported subfailures were manifest as tears in the intimal side of the artery while the adventitia remained intact (media was not visible). On average, these tears occurred at 60% of the failure stretch in older human specimens and 85% in younger porcine thoracic aortas.

While Stemper et al. did not examine the failure of specific microstructural constituents, a more recent study on rabbit ascending aortas did. Using light microscopy and histological stains, Austin showed severe damage to elastin and collagen fibers following 1000 cycles to a stretch level of 1.3 and mild damage with a stretch level of 1.06 [50]. ‘Severe damage’ was defined as “extensive or full-thickness tears or defects”

and ‘mild damage’ as “focal or superficial tearing, splitting, or discontinuities.” An aorta with severe damage is shown next to a control specimen in Figure 2.5. Although the author did not opine about which exact constituents were damaged, it is apparent from the image that ‘severe’ damage resulted in permanent deformation or even rupture of collagen and elastin fibers. While these findings do lend some insight into the thresholds at which structural damage occurs in arteries, the microstructures were only examined at the end of 1000 cycles. It is likely that repeat strain exposures produce microdamage in excess of what would have otherwise occurred from a single cycle [50].

2.5.2 Ligaments

In characterizing the mechanisms of TBI, it is no doubt more useful to first quantify the structural damage from a single insult than to study the effects of repeated injury. Since neither of the two preceding arterial studies correlated microstructural changes with single-insult damage thresholds, three ligament studies are now surveyed.

Provenzano et al. used macroscale changes in the ligament gauge length as an indicator of an altered microstructure [42]. They showed that strains above 5.14% induced a permanent increase in gauge length. This value also coincided with their observed threshold for changes in mechanical properties (6%). The authors speculated that the increased gauge length resulted from fiber damage and suggested that the collagen fibers may be torn or plastically deformed.

The work of Yahia et al. provides valuable insight into the precise damage thresholds of collagen fibers [51]. Using electron microscopy, they investigated threshold levels of collagen in the rabbit MCL. They observed no damage below 10% strain,

numerous broken thin collagen fibers (1 to 3 μm in diameter) at 10.5% strain, and ruptures of thick collagen fiber bundles (5 to 10 μm in diameter) at 20% strain. The initial threshold of broken collagen fibers (10.5% strain) also closely matched the 'yield' point in the ligaments that were stretched to 20% (Figure 2.6).

Panjabi et al. also studied rabbit ligaments (ACLs instead of MCLs) following overstretch to $\lambda = 1.2$ (previously detailed in Section 0). By correlating the findings of Yahia et al. with the effects of subfailure damage observed by Panjabi et al, it may be speculated that the rupture of collagen fibers (between $\lambda = 1.1 - 1.2$) is the microstructural mechanism behind the elongated toe-region and the decreased maximum modulus observed by Panjabi. However, recall that Provenzano et al. observed these same mechanical changes (in rat MCLs) at strains as low as 6% [42] – well below the range in which Yahia observed broken collagen fibers [51]. This means that, while the rupture of collagen fibers no doubt contributed to the altered mechanical properties in ligaments, it was not the sole mechanism.

A second study sheds additional light on microstructural changes which may cause altered mechanical properties. Using polarized light microscopy one author detected an increase in collagen disorganization in rat spinal ligaments following an axial distraction [43]. Surprisingly, it was also reported that a few specimens increased in stiffness near the maximum tangent modulus. This led the author to suggest that collagen fiber integrity in the direction of loading may not have been compromised but rather, that secondary microstructures (collagen cross-links, elastin, minor collagens, or circumferential collagens) may have been damaged.

2.6 Microstructural mechanisms behind an altered mechanical response

The postdamage increase in ligament gauge length observed by Provenzano [42] is a macrostructural mechanism that can explain the elongated toe-region reported in many of the ligament studies [40-45]. An increased gauge length essentially increases the zero-load point on the stress-stretch curve – shifting the entire curve to the right. If the gauge length continued to increase during the loading phase then this same mechanism would also explain the decrease in maximum modulus [41-43]; however, this has not been investigated. The increased gauge length after low level damage (< 10% strain) is likely due to secondary microstructural changes in collagen cross-links [43], the rupture of collagen fibrils [43], or even the growth of elastin fenestrae [52]. Increases in ligament gauge length following subfailure strains > 10% are likely aided by the additional rupture of large collagen fibers [51]. It is anticipated that these same general findings will hold true in blood vessels; however, they will likely occur at different thresholds since blood vessels have a different collagen/elastin ratio than ligaments.

Quantifying changes in blood vessel mechanical properties following subfailure damage is critical for understanding mechanical function, quantifying compromise with subfailure damage, and benchmarking normal functional behaviors to evaluate the efficacy of injury treatments. Additional investigations on the effects of subfailure axial deformations are needed in order to more clearly explain the mechanisms behind cerebrovascular impairment in TBI. Mechanical investigations should focus on changes in the elastic, viscoelastic, and failure properties as well as the effect of injury strain rate. Microstructural investigations should examine the rupture of collagen fibers and fibrils,

increases in elastin fenestrae, and macrostructural changes in vessel gauge length. Microstructural measures of collagen waviness, distribution, and orientation may prove to be useful metrics for such studies.

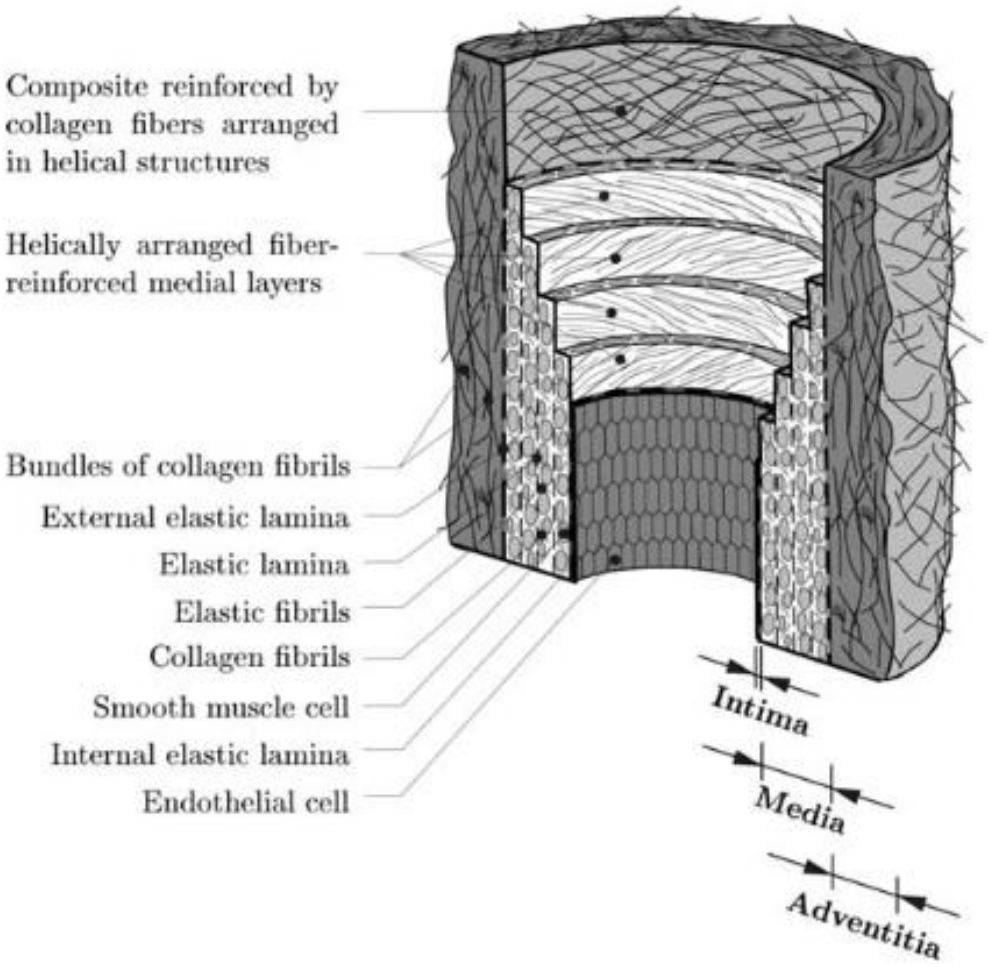

Figure 2.1: Idealization of a healthy elastic artery. It is composed of three layers: intima, media, and adventitia. Reproduced with permission [53].

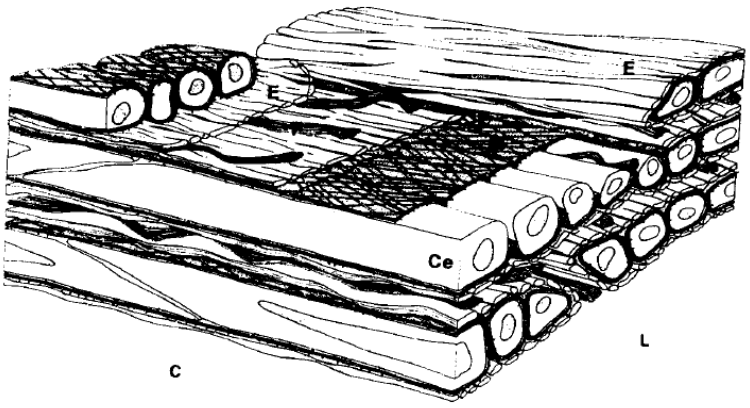

Figure 2.2: Schematic of the organization of elastin (E), smooth muscle cells (Ce), and collagen bundles (F) in the media of an elastic artery. Reproduced with permission [54].

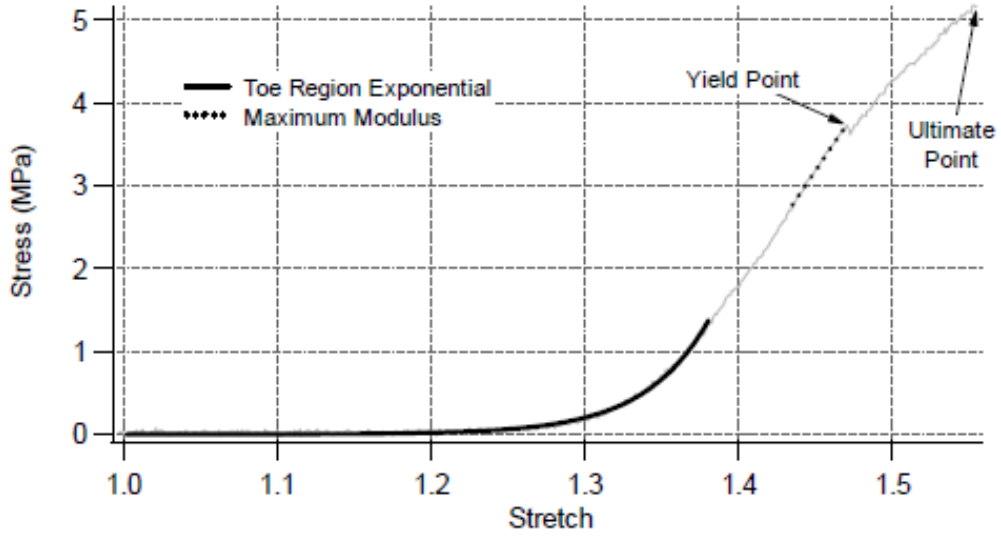

Figure 2.3: Parameterization of an example soft tissue stress-stretch curve. Reproduced with permission [40].

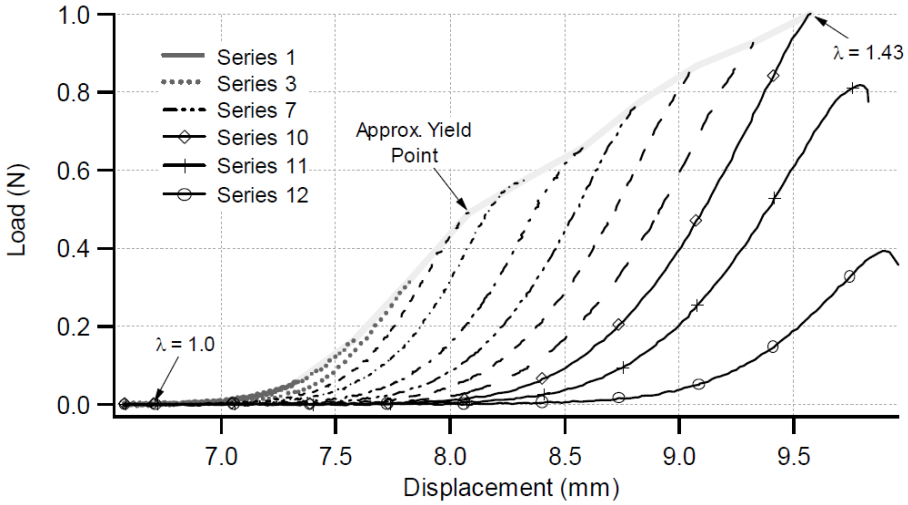

Figure 2.4: Load-displacement behavior of an artery subjected to successively increasing cycles up to failure. Only the intial loading ramp of each set of cycles is shown. Reproduced with permission [40].

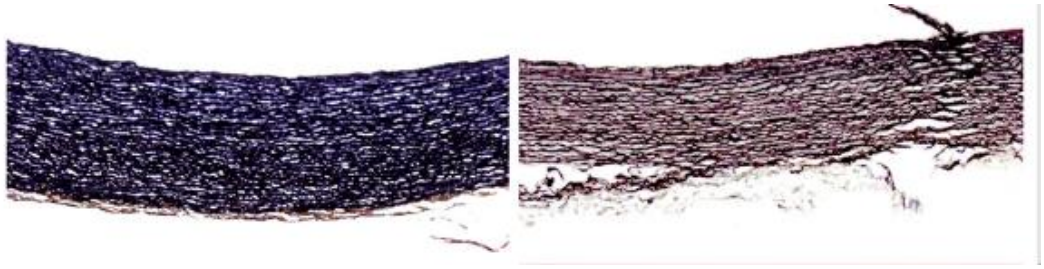

Figure 2.5: Aorta specimen with normal histologic appearance (left) and with severe tissue damage (right) Elastic fibers are stained in blue-black and collagen fibers yellow-orange. Reproduced with permission [50].

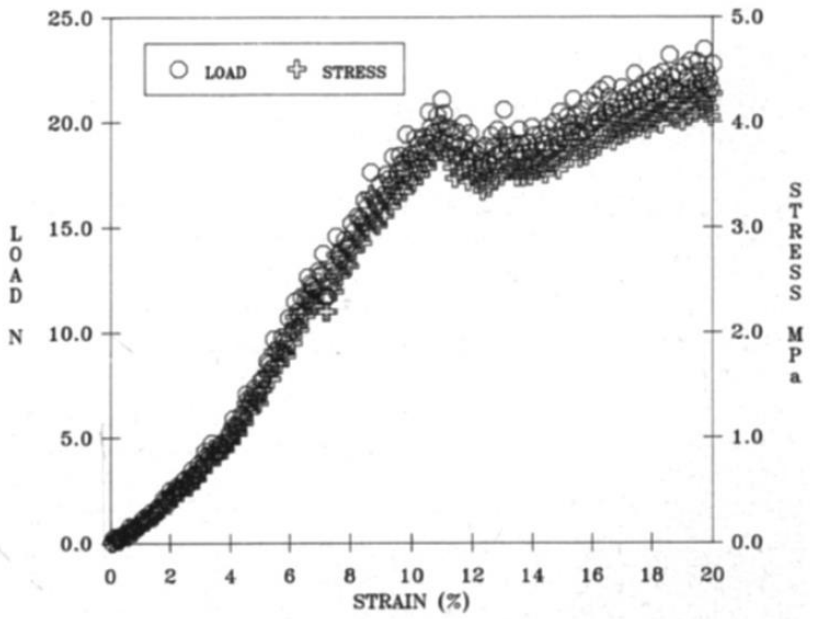

Figure 2.6: Load-strain curves for ligaments stretched to 20% strain. Microruptures of collagen fibers occurred at about 10.5% strain. This value coincides with the apparent 'yield' point of tissue. Reproduced with permission [51].

Table 2.1: Changes in the mechanical properties of blood vessels and ligaments/ tendons after a quasi-static, subfailure overstretch.

Quasi-static Failure Rate	Elastic		Visco-elastic	Failure Properties		
	Length of Toe-Region	Maximum Modulus	Decay Rate	Stretch at Failure	Load at Failure	Energy at Failure
Blood Vessels	Increase	Constant	no data	no data	no data	no data
Ligaments/ Tendons	Increase	Decrease*	Decrease	Constant	Decrease*	Constant

* denotes that at least one study found no statistically significant change

CHAPTER 3

BIAXIAL SOFTENING OF ISOLATED CEREBRAL ARTERIES FOLLOWING AXIAL OVERSTRETCH

3.1 Abstract

Arteries play a critical role in carrying essential nutrients and oxygen throughout the brain; however, vessels can become damaged in traumatic brain injury (TBI), putting neural tissue at risk. Even in the absence of hemorrhage, vessels can be distended beyond their physiological limit, compromising their mechanics. One recent investigation showed the effect of vessel elongation on axial mechanics; however, it did not address possible changes in circumferential mechanics that are critical to the regulation of blood flow. In order to address this in the present work, ovine middle cerebral arteries were isolated and overstretched axially to 10, 20, or 40% beyond the *in vivo* configuration. Biaxial changes were evaluated and data were fit with a recently proposed microstructurally-motivated constitutive model. Results showed a statistically significant decrease in circumferential stiffness and strain energy as well as an increase in vessel diameter following 40% overstretch ($p < 0.05$). These passive changes would lead to a decrease in vascular resistance and likely play a role in previous reports of cellular dysfunction. Furthermore, the constitutive model appropriately captured the direction of biaxial stress and stretch changes following overstretch in both axial and circumferential

loading; however, it was unable to properly model the magnitude of these changes across all levels of overstretch. We anticipate that our findings will increase understanding and ultimately serve to improve modeling of cerebrovascular mechanics following head trauma.

3.2 Introduction

Traumatic brain injury (TBI) is one of the major health care problems in the United States, contributing to nearly a third (30.5%) of all injury-related deaths [55]. An estimated 1.7 million people annually sustain a traumatic brain injury, and of these, approximately 50,000 die [55]. While damage to brain tissue is the fundamental concern in TBI, nearly all significant brain injuries include some element of injury to the blood vessels, and any injury or dysfunction of the vasculature puts neural tissue at risk. Visible lesions are common in head trauma, with contusion and intracranial hematoma occurring in 94 and 60%, respectively, of fatally injured patients in one reported series [2]. The incidence of nonhemorrhagic vascular dysfunction is more difficult to quantify, but alteration of cerebral blood flow is a common outcome of all types of head trauma [3-6, 56]. Although much of the observed nonhemorrhagic dysfunction in TBI is due to indirect effects associated with a perturbed biochemical environment, it is likely that any mechanically-induced changes in the vessel wall would also contribute [3].

In order to better understand the implications of overstretch on vessel mechanics, numerous investigations have characterized changes in the stress-stretch response following single or repeated overloads. These works, both experimental and computational in their nature, have demonstrated that overstretch softens, or increases the

compliance of, the arterial passive response in cases of both axial [40, 57-60]) and circumferential [60, 61] loading. However, as softening has been effectively attributed to collagen [62], it is no surprise that this phenomenon has also been reported in a number of soft tissues, namely, ligament [41-43, 46, 63], tendon [44, 64], intestine [65], and myocardium [66]. Limited work, however, has been done to understand softening in the cerebrovasculature. One recent investigation explored the effect of axial overstretch on the passive behavior of isolated middle cerebral arteries [57]. Also motivated to better understand head trauma, vessels were loaded axially as it is theorized to be their primary loading direction in TBI. The authors quantified the magnitude of stress softening and showed that this softening persisted over 60 min after injury. However, because mechanics are only studied in the axial direction, potential changes in the circumferential direction remain unknown. Subsequent work investigated the effect of overstretch on vascular smooth muscle cell function, with the authors finding a decrease in smooth muscle contractility [67]. Unfortunately, the study design did not enable the authors to determine what role changes in the extracellular matrix (ECM) may have played, further highlighting a need to understand alterations in the passive circumferential response following overstretch.

Based on a similar motivation and methodology as the aforementioned two studies, and given the critical role of circumferential loading in the regulation of blood flow, the objective of the present work is to investigate circumferential changes in cerebral artery mechanics following axial overstretch. Experiments are carried out in sheep middle cerebral arteries for comparison to previous studies. Furthermore, the resulting biaxial data are used to characterize softening with a structurally-motivated

constitutive model of damage. Given the previous findings of axial softening [57], and given that a reduction in axial stress increases the circumferential compliance of cerebral vessels [68, 69], we hypothesize that axial overstretch will also increase the circumferential compliance. Furthermore, we hypothesize that the softened biaxial response can be represented with a recently proposed pseudo-elastic constitutive model of vessel damage [60].

3.3 Methods

3.3.1 Specimen acquisition and preparation

Lamb heads were acquired from local slaughterhouses. Lambs (3-9 months) were sacrificed with either an electrical shock or mechanical impact to the spinal cord. Heads were transported to the lab on ice. Immediately thereafter, brains were removed, vessels dissected, and samples were stored in Hank's Buffered Saline Solution (HBSS; KCl 5.37, KH_2PO_4 0.44, NaCl 136.9, Na_2HPO_4 0.34, D-Glucose 5.55, $NaHCO_3$ 4.17; concentrations in mM) at 4 °C until the time of testing. Lack of calcium in the HBSS ensured a passive response of the vessel. Relatively straight segments of the MCA (approx. 5 mm in length) were dissected and side branches ligated with individual fibrils of unwound 6-0 silk suture. Vessels were then cannulated to two size-matched hypodermic needles with 6-0 silk suture and cyanoacrylate glue. In addition, 25 μm microspheres (Polysciences, Inc.; Polybead) were spread over the vessel surface to allow visual tracking of adventitial deformation during testing. All testing was done within 48 hrs of death [70].

3.3.2 Experimental apparatus

Mechanical tests were carried out on a horizontal platform which facilitated both circumferential and axial loading, while simultaneously recording vessel pressure and axial load. Specifically, one of the aforementioned hypodermic needles was attached to a 250 g capacity load cell (Honeywell, Model 31 Low) through an X-Y stage that allowed for needle alignment. The second needle was attached to the horizontal platform via a low friction sled supported by a voice coil actuator (Akribis, MGV52-25-1.0). Displacement of the actuator moved this second needle horizontally along the sled track, axially stretching the vessel. Specimens were viewed via a digital video camera (Pixelink, PL-A641) attached to a stereo microscope (Zeiss, Stemi 2000-C). Vessels were bathed in HBSS and perfusion was digitally controlled by a linear actuator (Ultra Motion, D-A0.25-AB-HT17075-4-P). Internal pressure was determined by averaging the signals of pressure transducers (Honeywell, 26PCDFM6G) located at each end of the vessel. Test control, as well as data and video acquisition, was accomplished using a custom LabVIEW program (National Instruments). Actuator positions were given by digital encoders (resolution 1.0 μm). Data from the encoders, load cell, and two pressure transducers were recorded at 100 Hz and images acquired at 3 Hz.

3.3.3 Mechanical testing procedure

3.3.3.1 Preconditioning and baseline characterization

Mechanical testing was similar to that described previously [68, 69]. Briefly, prior to mechanical characterization, each vessel was preconditioned by oscillating the internal pressure ($50 < p_i < 150$ mmHg) for five cycles while length was held constant at axial

stretch values up to 1.05 times the *in vivo* stretch. The axial *in vivo* stretch ($\lambda_{Z_{IV}}$) was estimated as the length at which pressure cycles had a negligible effect on the tensile load [71]. With the luminal pressure set to 0.25 mmHg, vessels were then stretched from a buckled state to 1.05*$\lambda_{Z_{IV}}$ and the reference unloaded length (L), corresponding to λ_Z = 1.0, was defined at the point where axial force became non-zero. Following this, the baseline (predamage) mechanical behavior of each vessel was characterized through a series of six quasi-static, biaxial sequences by cycling the pressure between 0-150 mmHg at three different axial stretches (1.05, 1.025, and 1.0*$\lambda_{Z_{IV}}$ named 'pre-P_{HI}', 'pre-P_{MED}', and 'pre-P_{LOW}', respectively) and cycling the length at three different constant pressures (150, 100, and 50 mmHg named 'pre-S_{150}', 'pre-S_{100}', and 'pre-S_{50}', respectively).

3.3.3.2 Injury

Beginning at *in vivo* stretch and pressure ($\lambda_{Z_{IV}}$, p_i =100 mmHg), vessels were then subjected to a single subfailure axial overstretch (rate ≈ 0.2 s^{-1}) and returned to their *in vivo* stretch. Controls were not overstretched, but were instead maintained at the *in vivo* configuration during this same period. The magnitude of overstretch was governed by the user-defined needle displacement; however, the precise local stretch was quantified after testing.

3.3.3.3 Postdamage characterization

Following overstretch, the six previously described biaxial sequences were repeated. The purpose of this was to better understand how vessels would behave following a traumatic injury. However, the precise axial stretch to which vessels would

return following deformation *in vivo* is unknown. Therefore, inflation tests were carried out at two sets of axial stretches: one in which the local axial stretch matched the predamage stretch ('post-P_{HI_L}', 'post-P_{MED_L}', and 'post-P_{LOW_L}') and a subsequent set that matched the predamage axial force ('post-P_{HI_F}', 'post-P_{MED_F}', and 'post-P_{LOW_F}'). In the three axial stretch tests, vessels were elongated up to the stretch that matched the corresponding predamage axial forces ('post-S_{150}', 'post-S_{100}', and 'post-S_{50}').

3.3.4 Data analysis

Experimental data were processed to generate stress-stretch curves for all of the biaxial sequences performed. Image processing software (National Instruments; Vision Assistant) was used to measure the current outer diameter (d_o) of the vessel, and measurements were interpolated to create a one-to-one correspondence with the other signals. The image corresponding to the unloaded configuration was used to measure the reference length (L) and reference outer diameter (D_o). Care was taken to measure the diameter in the same position along the midsection of the vessel in order to detect subtle changes after overstretch. In order to avoid end-effects [72], vessel stretch was measured using microspheres. An SAE J211 filter was applied to the pressure and force signals to reduce noise. Using an approach similar to that proposed by Wicker et al. [73], the volume of the vessel was estimated at six different configurations (combinations of λ_Z = 1.05, 1.025, 1.0*$\lambda_{Z_{IV}}$ and p_i = 50, 150 mmHg). The wall volume (V), outer diameter, and current length of the vessel (l) were then used to calculate the inner diameter (d_i) using Equation 3.1.

$$d_i = \sqrt{d_o^2 - \frac{4V}{\pi l}} \tag{3.1}$$

In a similar manner, D_o and L were used to calculate the reference inner diameter (D_i). Assuming the vessel to be a homogeneous cylinder, the midwall circumferential stretch (λ_θ) and axial stretch (λ_Z) were calculated using Equations 3.2 and 3.3.

$$\lambda_\theta = \left(\frac{d_i + d_o}{D_i + D_o}\right) \tag{3.2}$$

$$\lambda_Z = \left(\frac{l}{L}\right) \tag{3.3}$$

In vivo stretches were quantified using a single image from the 'pre-P_{LOW}' test (which was conducted at the axial *in vivo* stretch) taken at *in vivo* pressure (100 mmHg). Enforcing equilibrium in the two directions resulted in the mean circumferential (T_θ) and axial (T_Z) Cauchy stresses shown in Equations 3.4 and 3.5, respectively, with F_Z being the experimental axial force.

$$T_\theta = p_i \left(\frac{d_i}{d_o - d_i}\right) \tag{3.4}$$

$$T_Z = \frac{\lambda_Z}{A}\left(F_Z + \frac{\pi}{4} p_i d_i^2\right) \tag{3.5}$$

3.3.5 Damage quantification

In order to facilitate uniform quantification and modeling of damage, all stress-stretch data were discretized into 20 equally spaced points. Axial stretch test data below $\lambda_{Z_{IV}}$ were not sampled, as many vessels buckled (i.e., $F_Z < 0$) below this stretch. Inflation tests were sampled between pressure ranges of 50-150 mmHg.

To quantify the effect of overstretch, three parameters derived from the pre- and postdamage stress-stretch curves were compared for both loading directions: *in vivo*

stiffness, strain energy, and baseline stretch. These parameters were calculated for axial loading using the axial stretch tests conducted at *in vivo* pressure ('pre-S_{100}' and 'post-S_{100}') and for circumferential loading using the inflation tests conducted at the predamage axial *in vivo* stretch and tension ('pre-P_{LOW}', 'post-P_{LOW_L}', and 'post-P_{LOW_F}'). *In vivo* stiffness was defined by fitting a three-parameter exponential function to the stress-stretch data and calculating its derivative at the *in vivo* stretch ($\lambda_{\theta_{IV}}$ for axial stretch tests and $\lambda_{Z_{IV}}$ for inflation tests). Note that the term stiffness is used here as a measure of the resistance of the vessel structure to deformation, rather than as an intrinsic tissue property.

Strain energy was calculated as the area under the stress-stretch curve. Axial strain energy was calculated between the axial *in vivo* stretch and the maximum stretch experienced during the baseline characterization (1.05*$\lambda_{Z_{IV}}$ according to needle position), while circumferential strain energy was calculated between the stretches corresponding to 50 and 150 mmHg during the baseline inflation test.

Finally, baseline axial stress was defined as the axial stress corresponding to 1.03*$\lambda_{Z_{IV}}$ in the predamage axial stretch test (as done in [57]). Circumferential baseline stress was defined as the circumferential stress at 100 mmHg during the predamage inflation test. The corresponding stretch level at each of these stresses was defined as the baseline stretch (Figures 3.2 and 3.3). Percent change in each of the three metrics was calculated relative to the predamage test and the mean change in controls (due to the inflation and axial stretch cycles inherent to characterization) were subtracted from all groups.

One-way ANOVA, followed by a two-tailed t-test with a Bonferroni correction,

was used to determine significance of overstretch groups relative to controls, with $p < 0.05$ indicating statistical significance for ANOVA and $p < 0.0167$ for post hoc tests between groups.

3.3.6 Damage modeling

3.3.6.1 Pseudo-elastic damage model

Further analysis included fitting a recently proposed pseudo-elastic model of discontinuous softening [60] to the collected stress-stretch data. This model is based on the constitutive framework for arterial wall mechanics outlined by Holzapfel et al. [53], incorporates distributed fiber angles [38], and introduces a single damage variable, η, which serves to scale (soften) tissue stresses. The reader is referred to [60] for the complete description of the model; however, the most pertinent equations have been included here. As tissue damage has been found to be primarily related to the collagen fiber fabric [60], we neglect any possible damage to the noncollagenous matrix and apply damage only to the collagen fibers. The damage variable pertaining to the ith collagen fiber family, $\eta_i \in [0, 1]$, is, by definition, set equal to 1 on the initial, or predamage, loading curve and allowed to evolve to as low as 0 (representing 100% damage to the fiber family) according to Equation 3.6

$$\eta_i = 1 - \frac{1}{r_i}\,\mathrm{erf}\left[\frac{1}{m_i}\left(\bar{\psi}^{max} - \bar{\psi}^{0}\right)\right] \tag{3.6}$$

where erf() is the error function, $\bar{\psi}^{max}$ denotes the maximum of the strain-energy obtained in the deformation history, and $\bar{\psi}^{0}$ denotes the isochoric strain-energy of the undamaged material. Further, $r_i > 1$ characterizes the maximum damage that can be induced under loading, and $m_i > 0$ determines the dependence of the damage on the

deformation. In the present work, $\bar{\psi}^{max}$ was calculated at the peak of axial deformation during overstretch and $\bar{\psi}^{0}$ was associated with the *in vivo* configuration. The damage variable, η_i, scales fiber fabric stresses according to Equation 3.7

$$\overline{\boldsymbol{S}} = \mu\frac{\partial \bar{I}_1}{\partial \boldsymbol{C}} + \sum_i \eta_i \overline{\boldsymbol{S}}^0_{f,i} \tag{3.7}$$

where $\overline{\boldsymbol{S}}$ is the isochoric part of the second Piola-Kirchhoff stress tensor, $\mu > 0$ corresponds to the shear modulus of the isotropic, noncollagenous matrix in the reference configuration, and $\bar{I}_1 = tr(\overline{\boldsymbol{C}})$ is the first strain invariant of the modified right Cauchy-Green tensor $\overline{\boldsymbol{C}}$. $\overline{\boldsymbol{S}}^0_{f,i}$ is the second Piola-Kirchhoff stress tensor related to the fiber fabric on the predamage loading curve for the ith fiber family and is defined by Equation 3.8

$$\begin{gathered}\overline{\boldsymbol{S}}^0_{f,i} = 2k_1^i(\bar{I}_i^* - 1)\exp[k_2^i(\bar{I}_i^* - 1)^2]\frac{\partial \bar{I}_i^*}{\partial \boldsymbol{C}} \\ \bar{I}_i^* = \kappa_i \bar{I}_1 + (1 - 3\kappa_i)\bar{I}_i\end{gathered} \tag{3.8}$$

where $k_1^i > 0$ is a stress-like parameter, and $k_2^i > 0$ is a dimensionless parameter. The strain energy of a given fiber family only contributes to the overall strain energy when the fibers are extended, that is, $\bar{I}_i^* > 0$. The pseudo-invariants $\bar{I}_i = \overline{\boldsymbol{C}}: (\boldsymbol{a}_{0i} \otimes \boldsymbol{a}_{0i})$ correspond to the square of the stretches of the fibers in the fiber directions, with $\boldsymbol{a}_{0i}$ being (reference) direction vectors for each fiber family [53]. The dispersion parameter $\kappa \in [0, 1/3]$ describes the radial symmetry of the dispersion about the fiber direction [38], with the lower and upper bounds indicating no fiber distribution (highly anisotropic, single fiber) and an isotropic fiber distribution, respectively. Similar to Weisbecker et al. [60], we assumed the deformation process in our experiments to be isochoric; therefore, the volumetric part of the second Piola-Kirchhoff stress tensor was set to zero, $J = \det(F) = 1$, and the Cauchy stress tensor, σ, is obtained through a standard push-forward

operation (Equation 3.9).

$$\sigma = F\bar{\boldsymbol{S}}F^T \tag{3.9}$$

3.3.6.2 Model parameters

The experimental stress-stretch data were fit to two variations of the pseudo-elastic damage model. In a slight deviation from the general framework [53], we incorporated axial and circumferential fiber families, as opposed to only helical families, based on previous reports of primarily axial and circumferential fiber families in cerebral arteries [37, 74]. The first model consisted of a single axial (i = 1) and a single circumferential (i = 2) fiber family, each with distributed fibers. Therefore, the initial, or predamage, loading curve can be modeled with up to seven material parameters (μ, k_1^1, k_1^2, k_2^1, k_2^2, κ_1, κ_2) and the softened response with up to four damage parameters (r_1, r_2, m_1, and m_2). However, as data were collected around and beyond the *in vivo* stretches, where collagen begins to dominate the mechanical behavior [75], the shear modulus, μ, was set equal to zero. Further, as circumferential fibers in cerebral vessels have minimal dispersion [37, 74], κ_1 was also set to zero. Finally, in this first model damage was only allowed to accumulate in the axial fibers ($\eta_1 = 1$) as circumferential fibers undergo compression during axial overstretch. These simplifications reduced the first model to seven variables: two for the circumferential family (k_1^1, k_2^1) and five for the axial family (k_1^2, k_2^2, κ_2, r_2, m_2). Stress-stretch data were also fit to a second model which consisted of four fiber families similar to that proposed by Wicker et al. [74]: an axial, circumferential, and two symmetric helical fiber families (i = 3, 4) at an angle of $\pm\varphi$ from the circumferential direction of the artery. Addition of helical families eliminated

the need for any fiber dispersion ($\kappa_i = 0$), but allowed for the unique evolution of damage in the helical and axial fiber families with four damage variables (r_2, m_2, $r_{3,4}$, $m_{3,4}$) instead of just two as in the first model. Therefore, this second model consisted of 11 total variables: two for the circumferential family (k_1^1, k_2^1), four for the axial family (k_1^2, k_2^2, r_2, m_2), and five for the helical families ($k_1^{3,4}$, $k_2^{3,4}$, φ, $r_{3,4}$, $m_{3,4}$).

3.3.6.3 Normalization of stress-stretch curves

In order to properly model the evolution of collagen damage with overstretch, the model had to be fit simultaneously to postoverstretch data from more than one sample (as each sample was subjected to only one level of overstretch). However, given the inherent biological variability in the predamage response of all samples, biaxial stress and stretch data were scaled, or normalized, so that their predamage *in vivo* configurations aligned at the population mean. Previous work in our lab has shown that normalization relative to the *in vivo* stretch can reduce intersample mechanical variability [68], possibly attributable to the improved signal-to-noise ratio when collecting *in vivo* rather than unloaded measurements. Scaling factors were calculated for each of the 16 samples according to Equation 3.10:

$$f_{\lambda_\theta} = \frac{\overline{\lambda_{\theta_{IV}}}}{\lambda_{\theta_{IV}}}$$

$$f_{\lambda_Z} = \frac{\overline{\lambda_{Z_{IV}}}}{\lambda_{Z_{IV}}} \tag{3.10}$$

$$f_{T_\theta} = \frac{\overline{T_{\theta_{IV}}}}{T_{\theta_{IV}}}$$

$$f_{T_Z} = \frac{\overline{T_{Z_{IV}}}}{T_{Z_{IV}}}$$

with the vinculum denoting the mean (*in vivo*) configuration for the entire population and λ and T referring to stretch and stress data, respectively. A total of eight scaling factors were calculated for each sample, four for inflation test data and four for axial stretch test data. Scaling factors for inflation test data were calculated using predamage inflation tests carried out at the axial *in vivo* stretch and pressure ('pre-P_{LOW}', 100 mmHg), while factors for axial stretch test data were calculated from the 'pre-S_{100}' tests with the *in vivo* configuration identified at the axial *in vivo* stretch. Normalized stress-stretch data were then calculated by multiplying all biaxial data (9 inflation tests: 3 pre- and 6 postdamage; 6 axial stretch tests: 3 pre- and 3 postdamage) by the corresponding scale factors. It can be shown mathematically that scaling of the data in this manner has no effect on metrics used to evaluate softening (Section 3.3.5).

3.3.6.4 Model fitting

The 16 normalized datasets used for constitutive model fitting consisted of biaxial data from the three postoverstretch axial stretch tests ('post-S_{150}', 'post-S_{100}', and 'post-S_{50}') as well as biaxial data from the three postoverstretch inflation tests that most evenly spanned the axial strain range used during characterization ('post-P_{HI_F}', 'post-P_{MED_F}', and 'post-P_{LOW_L}'). Only three of the six postoverstretch inflation tests were used in order to prevent biasing the model. The postoverstretch data from the control group (n=4 samples) served to fit 'predamage' material coefficients (k_1^i, k_2^i, and either κ_2 or φ), while datasets from the three overstretch groups (n=12 samples) served to fit damage variables (r_i and m_i). Using 'postoverstretch' data from the control group, rather than

'preoverstretch' data, eliminated any softening inherent to characterization of the vessel and forced the model to only fit softening due to overstretch. Both models were optimized using all four datasets simultaneously by employing a nonlinear regression routine 'fminsearchbnd' (Mathworks, MATLAB) to minimize the objective function *f* (Equation 3.11)

$$f = \sum_{j=1}^{N} \left[\left(\frac{t_{\theta\theta} - T_{\theta}}{T_{\theta}} \right)_j^2 + \left(\frac{t_{ZZ} - T_Z}{T_Z} \right)_j^2 \right] \tag{3.11}$$

where N represents the total number of data points, $t_{\theta\theta}$ and t_{ZZ} are the theoretical circumferential and axial stresses from the Cauchy stress tensor in Equation 3.9 and T_{θ} and T_Z are the experimental stresses from Equations 3.4 and 3.5. To restrict the parameter search space, all parameters had a lower bound of 0 except for r_i which, by definition, had to be great than or equal to one. Only the fiber orientation terms, κ_2 and φ, had upper bounds (1/3, π/2, respectively). Due to the large number of parameters in the 4-fiber model, and in order to ensure that the model converged on the optimal parameters, initial solutions were fed back into the optimization routine until additional looping ceased to decrease the output of the objective function. One sample from the highest overstretch group (40%) could not be returned to the predamage axial *in vivo* stretch without inducing buckling. Therefore, it was removed from all constitutive modeling. The objective function was weighted accordingly so that the model fit all four overstretch groups evenly. Finally, as there were only four samples per overstretch group, it did not seem appropriate to withhold data from the model development in order to validate the model. Therefore, model validation was not performed.

3.3.6.5 Softening metrics

In order to compare model and experimental results, the same (three) metrics used to describe the experimentally observed softening (Section 3.3.5) were applied to the two optimized models. One-way ANOVA, followed by a two-tailed t-test with a Bonferroni correction, was used to determine significance of model results relative to experimental results, with $p < 0.05$ indicating statistical significance for ANOVA and $p < 0.025$ for post hoc tests at each overstretch level.

3.4 Results

3.4.1 General observations

Sixteen arteries were successfully tested (four per stretch group), and had unloaded lengths of 3.83 ± 0.65 mm ($\mu \pm \sigma$), outer diameters of 1.10 ± 0.09, wall thickness of 81 ± 17 μm, and mean axial and circumferential *in vivo* stretches of 1.26 ± 0.03 and 1.21 ± 0.03, respectively. As expected, predamage axial and circumferential stress-stretch behaviors were nonlinear and previously established biaxial interactions were also observed (Figure 3.1), that is, decreasing the stretch in either the axial or circumferential directions made the vessel more compliant in the other [68, 69]. Furthermore, these general behaviors were also observed after damage (Figure 3.1). As hypothesized, in addition to softening in the axial direction, vessels softened circumferentially; however, softening was more significant in the axial than circumferential direction. Finally, the magnitude of change increased with overstretch severity.

3.4.2 Axial softening

Axial softening, characterized by a decrease in axial stress at the same axial stretch, was most apparent in axial stretch tests (Figure 3.1a). Though as inflation tests load the vessel axially, axial softening was also observed in these tests (Figure 3.1d), specifically, when the vessel was held at the predamage axial stretch ('post-P_{HI_L}', 'post-P_{MED_L}', and 'post-P_{LOW_L}'). However, in order to compare axial softening to that reported previously [57], axial softening was quantified on only the axial stretch tests carried out at *in vivo* pressure ('pre-S_{100}', 'post-S_{100}'; blue lines in Figure 3.1a, c). Doing so showed that softening in the axial direction was similar to that observed by Bell et al. for all three measures quantified. Specifically, we found a reduction in the axial *in vivo* stiffness (Figure 3.2b), a reduction in the axial strain energy (Figure 3.2c), and an increase in axial stretch at baseline axial stress (Figure 3.2d). Statistical analysis also showed that the mechanical behavior was significantly different from controls beginning at a 20% overstretch for all three measures, the same as that found previously [57]. Interestingly, the magnitude of change in strain energy was comparable to the previous investigation even though Bell et al. quantified strain energy over a much broader range (unloaded length up to maximum overstretch). In contrast, strain energy in the present work was only quantified from the *in vivo* stretch up to the maximum stretch during preconditioning (as stretch measurements below $\lambda_{Z_{IV}}$ were not reliable, and vessels were only stretched to the maximum overstretch level once).

3.4.3 Circumferential softening

As hypothesized, softening was also observed in the circumferential direction following a single axial insult; however, softening was most notable when characterized at the predamage axial stretch following overstretch and less so when characterized at the predamage axial tension (Fig 3.1b). For vessels returned to the predamage axial stretch (blue lines in Figure 3.3), softening was observed for all three measures. Specifically, we found a reduction in the circumferential *in vivo* stiffness (Figure 3.3b), a reduction in the circumferential strain energy (Figure 3.3c), and an increase in circumferential stretch at baseline circumferential stress (Figure 3.3d). All changes were statistically significant following a 40% overstretch in contrast to the lower threshold (20%) required for axial softening. Similar trends were observed for vessels returned to the predamage axial force (green lines in Figure 3.3); however, changes were more subtle and only statistically significant for the increase in circumferential stretch following 40% overstretch (Figure 3.3d).

3.4.4 Damage model

The pseudo-elastic damage model was found to appropriately capture the direction of stress-stretch changes following overstretch in the biaxial data; however, it was unable to properly model the magnitude of these changes across all levels of overstretch. This was true for both the 2- and 4-fiber models. Interestingly, despite having two fewer material parameters and two fewer damage parameters, the 2-fiber model performed similarly to the 4-fiber model (respective objective function values of $f = 16.3$ and 14.8; see also mean absolute errors in Tables 3.4 and 3.5). Both models, however,

struggled to capture the full nonlinearity of the vessel stress-stretch response and, in general, underestimated the degree of softening following higher levels of overstretch.

3.4.4.1 Normalization of stress-stretch data

Prior to fitting the damage model, all stress-stretch data were normalized to the population mean *in vivo* configuration. Normalization effectively aligned postdamage responses (according to predamage mechanics) so that the damage model could be optimized on all stretch groups simultaneously (Figures 3.4 and 3.5). Population stretches and stresses used to calculate the scaling factors (Equation 3.10) are provided in Table 3.1.

3.4.4.2 Model softening

The 2-fiber model did a reasonable job of fitting the postoverstretch datasets from the four stretch groups (Figures 3.6 and 3.7, left panels). In general, the model demonstrated characteristic axial stress softening in axial stretch tests (Figure 3.6a) and captured the circumferential softening in inflation tests (though softening was quite subtle until 40% overstretch, Figure 3.6c); however, the model couldn't fully capture the nonlinearity of these same curves. The model did capture the general shifting observed in the transverse loading data (Figure 3.7a, c), though, again, model changes were negligible for mild (10%) and medium (20%) levels of overstretch for vessel inflation (Figure 3.7c). Optimal parameters for this model are provided in Table 3.2.

The inability of the 2-fiber model to capture the nonlinearity of the primary loading responses (Figure 3.6a, c), led us to add two additional fiber families,

specifically, two symmetric helical families, similar to that done elsewhere [74, 76]. This 4-fiber model did a slightly better job of capturing the nonlinearity of the primary loading response in axial stretch tests (Figure 3.6b); however, most other fits were comparable to those of the 2-fiber model (Figures 3.6d, 3.7b, and 3.7d). Optimal parameters for the 4-fiber model are provided in Table 3.3.

The average absolute error of the 4-fiber model across all datasets was only slightly better than that of the 2-fiber model (18.0% compared to 19.5%). Optimization was fairly uniform across all stretch groups (Table 3.4), though the model fit circumferential stresses from inflation tests with the least amount of error (Table 3.5).

3.4.4.3 Softening metrics

In order to better compare model and experimental results, the same metrics used to describe the experimentally observed softening (Figures 3.2 and 3.3) were applied to the two optimized models. Figures 3.8, 3.9 and 3.10 provide visual comparisons of the softening observed in axial stretch tests at *in vivo* pressure (Figure 3.8), inflation tests at the predamage axial *in vivo* stretch (Figure 3.9), and inflation tests at the predamage axial *in vivo* tension (Figure 3.10). In general, comparisons showed that the both models captured the general softening trends in all directions; however, they often underestimated the degree of softening following the higher levels of overstretch. Errors were often the greatest for the 20% overstretch group.

3.4.4.4 Model biaxial response

Figures 3.6 through 3.10 and their related text addressed the ability of the model to capture the arterial response following various levels of overstretch; however, another important aspect is the ability of a model to represent multiaxial effects, that is, interactions between loading directions. By plotting pre- and postdamage data from axial stretch tests at different pressures and inflation tests at different axial stretches (Figure 3.11), we compared the biaxial effects of the model with those observed experimentally. In general, an increase of internal pressure in the model (with axial stretch held constant) was found to underestimate the increase in axial stress seen experimentally (Figure 3.11a, b, and c). This disparity held true both before and after overstretch in both models. Regarding the effect of axial stretch on circumferential stretch (with pressure held constant), the models reasonably represented the decrease in circumferential stretch (Figure 3.11d, e, and f); however, the lower slope in the predamage model response resulted in a less significant change in circumferential stress. This disparity between the pre- and postoverstretch biaxial response is significant enough that overstretch results in circumferential stress softening when the vessel is held at the axial *in vivo* stretch (black lines in Figure 3.11e and f) yet an increase in stress when evaluated at higher axial stretches (blue and red lines in Figure 3.11e and f) – the opposite of that observed experimentally (Figure 3.11d).

3.5 Discussion

The objective of the present work was to characterize circumferential softening of cerebral arteries following axial overstretch and test the feasibility of representing such

softening with a microstructurally-motivated constitutive model. All tests were carried out in passive cerebral arteries in order to isolate changes to the extracellular matrix. As hypothesized, axial overstretch was found to soften vessels circumferentially, though the degree of softening was not as significant as that occurring in the axial direction. To our knowledge, these results present the first characterization of circumferential softening following axial overstretch for any arterial tissue. In addition, the experimental data were used to fit a recently proposed pseudo-elastic model that represents individual families of collagen fibers with Fung-type strain energy functions. As previous works have only fit this model to biaxial data from uniaxial tension tests [60], we wanted to test the ability of the model to fit more physiologically relevant data from multiaxial loading. Results showed that while the model could capture the general biaxial softening, its inability to capture the nonlinearity of much of the data prevented it, in some instances, from properly representing the magnitude of the softening. It is unclear to what degree these discrepancies are due to the experimental methods used or to limitations of the damage model; however, this is discussed in Section 3.5.3. We anticipate that our experimental findings will increase understanding and ultimately serve to improve modeling of cerebrovascular mechanics in head trauma.

3.5.1 Experimentally observed circumferential softening

Three metrics were used to characterize the degree of circumferential softening: change in circumferential *in vivo* stiffness, change in circumferential strain energy, and change in circumferential stretch at the baseline circumferential stress. As the axial stretch to which a vessel would return following trauma is unknown, the circumferential

response was evaluated at two different configurations following overstretch. The first of these, returning the vessel to the same axial stretch, assumes a preservation in the geometry surrounding the vessel while the second, returning the vessel to the same axial tension, assumes a preservation in boundary loads. As overstretch softens the vessel axially, the latter of these inherently evaluates the vessel at a more elongated configuration than the former, which ultimately attenuated or eliminated the magnitude of circumferential softening (Figure 3.5). At this axial 'tension-matched' configuration, we found no change in the circumferential *in vivo* stiffness or in the strain energy, but did find an increase in circumferential stretch (diameter) following the most severe overstretch. In contrast, circumferential softening was more pronounced when evaluated at the axial 'stretch-matched' configuration, with statistically significant changes being found in stiffness, strain energy, and circumferential stretch. While changes were observed following stretches as mild as 20% beyond *in vivo*, they were only statistically significant at 40% (Figure 3.5). These three findings can be summarized as a reduction in the luminal pressure required to produce the same circumferential stretch for all stretches spanned in the physiological range of blood pressures (50-150 mmHg). Specifically, we found up to a 1.2% increase in circumferential stretch. This subtle change, according to Poiseuille's Law, would result in a 5% reduction in vascular resistance and an equal increase in blood flow. However, as passive mechanics make up just one part of the overall vessel response, it is premature to project what influence such a change might have on the vascular behavior *in vivo*.

One recent *in vitro* study from our lab explored active changes in rat middle cerebral arteries following axial overstretch [67]. Investigators found a reduction in the

potassium-evoked contractility of the vascular smooth muscle cells. However, as contractility was evaluated by measuring vessel diameters, the authors were unable to determine the relative contribution of active and passive constituents. One test group stretched quasi-statically to 30% beyond the axial *in vivo* stretch (roughly 85% to failure) showed close to a 3.5% decrease in contractility (see Figures 3.2a and 3.2c in [67]; 30, 40, and 60 mM concentrations). In comparison, our highest overstretch group (40% beyond *in vivo*, roughly 80% to failure) showed only a 1.2% increase in circumferential stretch, which would equate to a 1.2% decrease in contractility. As this accounts for one-third of the reported impairment, it suggests that passive changes do play a meaningful role in the observed change in contractility; however, cellular changes are still more significant. This comparison is preliminary, though, as the two studies were carried out in different species. One investigation of the effect of balloon angioplasty also hypothesized that damage to both active and passive constituents was involved in impaired contractile function. In addition to observing cell death, the authors surmised that "disruption of extracellular structures and their mechanical coupling to the cells during overstretch may also have been involved." Furthermore, they stated that it was "likely that increased resting diameter after both hyperdistension and ballooning was due to matrix disruption" [77]. Given our observations, we, too, believe that both cellular and ECM damage contribute to vascular dysfunction in overstretch.

3.5.2 Comparison of axial and circumferential softening

Following axial overstretch, artery mechanics were found to soften less in the circumferential than the axial direction. Percent reductions in *in vivo* stiffness and strain

energy were roughly half of that found for the axial direction, and percent increases in circumferential stretch were roughly one-tenth of that found for increases in axial stretch. This finding suggests that ECM softening following axial overstretch may be more likely to result in artery buckling than in a meaningful change in circumferential compliance. This may seem intuitive given that all fibers bearing the axial load (axial and helical) were overstretched while only some of the fibers bearing the circumferential load (helical but not circumferential) were overstretched. However, a different result was found in a study on the effect of circumferential overstretch on biaxial mechanics. Oktay et al. characterized the response of bovine coronary arteries before and after circumferential overdistension with a balloon catheter [61] and found the degree of axial and circumferential softening (measured by strain energy) to be similar. However, because the vessel was constrained at each end, balloon expansion likely elongated axially oriented fibers, too, causing more of a biaxial overload, rather than the purely uniaxial one in the present work.

3.5.3 Appropriateness of the damage model

The damage model was found to appropriately capture the direction of stress-stretch changes in the biaxial data following overstretch (Figures 3.6 – 3.11); however, it was not able to properly model the full nonlinearity of the vessel response (Figures 3.6 and 3.7) or match the precise magnitude of softening at all levels of overstretch (Figures 3.8, 3.9, and 3.10). Therefore, if the model is to be implemented, it should be done with the limitations addressed in Section 3.4.4 in mind. For example, as the model captured axial softening fairly well (Figure 3.8), it could potentially be used to understand the

likelihood of vessel buckling. However, because the model often underestimated the degree of circumferential softening, its implementation in a study of changes in blood flow following overstretch would yield conservative results. Other models can and should be explored for fitting these data; however, to our knowledge, the one implemented is the only existing model that would also yield microstructural insights.

It is unclear to what degree the model discrepancies are due to the experimental methods used or the limitations of the damage model. As other works have only validated the model against uniaxial tension tests [60], it is possible that the damage model needs to be developed further to better mimic the softening observed in multiaxial loading. However, two aspects of our experimental approach could also be contributing factors. First, the current model does not account for permanent deformations, yet the highest overstretch group (40%) likely had some residual axial strains [57]. However, given the linearity in softening across the various overstretch levels (Figures 3.2 and 3.3), we do not expect that would play much of a role in model errors. Second, the model was forced to optimize data from multiple vessels simultaneously. While efforts were made to scale the data accordingly, this normalization cannot account for all biological variability which is inevitably present in the tissue. Such variability can add noise and make it more difficult for the model to find an appropriate solution. While optimization was run using dozens of different initial guesses, given the many degrees of freedom, we cannot guarantee that a better solution does not exist. Fitting the model to individual vessels would require repeated overloads, which we intentionally avoided. These complexities, along with possible alternative approaches, are addressed further in Section 3.5.7.

3.5.4 Model parameters

3.5.4.1 2-fiber model

To our knowledge, 2-fiber models have not been previously used to model cerebral arteries; however, in general, the elastic coefficients we found for both fiber families, $k_1^{1,2}$ and $k_2^{1,2}$, were comparable to those reported previously for 4-fiber models of cerebral arteries from large animals [74, 76]. The one exception to this was the stiffness-like parameter for the axial fiber family, k_1^2, which was 1-2 orders of magnitude higher than those found previously; however, this was expected since the single axial family had to compensate for the absence of helical families. In addition, the value of the damage parameter, r_2, was comparable to those found in the original implementation of the model [60]. The second damage parameter, m_2, was an order of magnitude higher than in the previous report; however, the mean orientation and distribution of the fibers in the present study were quite different and may not be comparable. The main anomaly in the model was the predicted value of the dispersion parameter for the axial fiber family ($\kappa_2 = 0.308$), which denotes a nearly isotropic distribution of fibers ($\kappa_2 = \frac{1}{3}$ denotes pure isotropy). A value of roughly half that would provide a better approximation of distributions previously reported for cerebral artery adventitia (see Figure 7a in Wicker 2008 [74]).

3.5.4.2 4-fiber model

The inability of the 2-fiber model to capture the nonlinearity of the primary loading data (Figure 3.6a, c) and the nearly isotropic axial fiber dispersion led us to implement a 4-fiber family model. All elastic and damage parameters fell within the

ranges in previous reports [60, 74, 76]; however, the relative nonlinearity of the axial and helical fibers was different from one report [74]. This discrepancy is addressed in detail in Section 3.5.5.

3.5.5 Fiber-specific damage evolution and stress softening

3.5.5.1 Evolution of damage with overstretch

One of the motivations for fitting the experimental data to a constitutive model was to potentially glean insights into the relative contribution of specific fiber families in softening; therefore, a previously developed structurally-motivated model was implemented [60]. While the model did not fit the data as well as anticipated, its ability to capture the general softening phenomenon led us to still examine the fiber-specific mechanics. The effect of the two family-specific damage variables used by this model, r_i and m_i, is best summarized by plotting the evolution of damage variable, η_i, using Equation 3.6. As this variable directly scales fiber stresses (Equation 3.7), it provides the degree of softening for each fiber family as a function of stretch. However, as the 2-fiber model only allowed damage to evolve in the axial family (circumferential fibers undergo contraction during axial overstretch), it doesn't provide meaningful insights about the relative role of multiple fiber families in softening; nevertheless, observing the evolution of damage in this one family is insightful. The 2-fiber model showed that the percentage of damage among the distributed axial fibers was roughly 3, 8 and 80% ($\eta \approx 0.97$, 0.92, and 0.2) at 10, 20, and 40% overstretch, respectively (Figure 3.12a). Damage stopping at $\eta \approx 0.2$ suggests that the axial family never completely lost its ability to bear load. This should be expected as samples were not pulled to failure. Microstructural insights are

more enlightening, however, when multiple fiber families are allowed to independently incur damage, as was the case with the 4-fiber model. Results for this second model showed damage among axial fibers to evolve more rapidly with strain than helical fibers; however, axial damage plateaued around 25% overstretch while damaged helical fibers lost most of their load bearing capacity near 40% overstretch (Figure 3.12b). Though, as shown later, the relatively large exponential term for the helical family (Table 3.3) allowed these fibers to still bear meaningful loads following 40% overstretch (red lines in Figure 3.13b). The initial higher rate of damage accumulation among axial fibers seems physically reasonable as these are more aligned with loading than helical ones. However, the fact that damage to axial fibers ceased after 25% overstretch is likely an artifact of the stretch levels explored in the experimental data. This end behavior would likely change if data from additional levels of overstretch (20-40% or even >40%) were used in the optimization. Although the rate of damage accumulation may be expected to decay at higher stretches [78], it does not seem physically reasonable for damage to asymptote at a point other than $\eta=0$ ($r=1$). However, early plateauing of the damage evolution parameter was also observed in previous implementations of the model (see Figure 1 in [60]).

3.5.5.2 Fiber-specific contributions to stress softening

Further insights can be gleaned from the 4-fiber model by plotting the stresses related to individual fiber families during loading. Doing so showed that circumferential fibers played the dominant role in bearing circumferential stress in inflation tests (black lines in Figure 3.13a) while axial fibers bore the majority of the load in axial stretch tests (black lines in Figure 3.13b). In order to reveal which fibers were primarily responsible

for stress softening, fiber stresses were also plotted following each level of overstretch (dashed lines in Figure 3.13). The case of circumferential stress softening is trivial, as of the fibers bearing circumferential load (circumferential and helical fibers), only the helical ones are stretched during axial overstretch, and were, therefore, the only fibers allowed to incur damage in the model (recall that helically oriented fibers in the 2-fiber model are part of the axial family). Hence, circumferential fibers maintained the same mechanical response before and after overstretch while helical fibers softened (Figure 3.13b). This, by definition, makes helical fibers the only possible contributors to the previously reported circumferential stress softening (Figures 3.3 and 3.6c, d). However, the matter is less trivial for the case of axial stress softening as both axial and helical fibers bear axial load and both can reasonably undergo damage during axial overstretch. As expected from examination of the damage evolution (Figure 3.12), both fiber families soften following overstretch (Figure 3.13b). By calculating the relative contribution of each family in the total axial stress near the axial *in vivo* stretch (left edge of traces in Figure 3.13b), the axial fibers (solid lines) are the contributor, accounting for roughly 90, 63, and 48% of the total axial softening following 10, 20, and 40% overstretch, respectively (where total helical stresses are twice that shown in Figure 3.13b as there are two symmetric helical families).

The fact that the 4-fiber model found axial fibers to play the major role in axial softening around the *in vivo* configuration seems physically reasonable and is consistent with the established literature. Both helical and axial fiber families have been shown to reside in the adventitia of cerebral arteries [74] and are likely to be composed of the same type of collagen. As such, it is reasonable to assume that fiber mechanics are similar

between axial and helical fibers, making fiber-specific softening primarily a function of fiber deformation, given that axial fibers deform more than helical fibers during elongation would cause them to undergo more damage and play a larger role in softening. However, we hesitate to put too much emphasis in the family-specific damage evolution (Figure 3.12b) and stress softening (Figure 3.13) findings from our model. This is because the amount of damage that the model predicts for a specific fiber family is highly dependent on the material coefficients describing the predamage response. As discussed later in Section 3.5.7, our test methodology didn't allow us to fit the predamage response over a wide range of strains. Therefore, though the model fit the experimental data reasonably well, it is difficult to be confident in the structural implications of the resulting model parameters. Specifically, the 4-fiber model found the helical fibers to have a greater exponential increase in stress with stretch than the axial fibers. An opposite behavior was found in two previous reports in rabbit [74] and porcine [76] basilar arteries. While mechanics of the sheep MCA may very well differ from these, we expect that the mechanics are similar given the proximity of the basilar artery to the MCA in the cerebral circulation. Therefore, given these reasons, we recommend that additional tests be done to better characterize the predamage response prior to drawing firm conclusions about family-specific damage. Ultimately, model insights only provide hypotheses for structural changes, but in order to be conclusive, these hypotheses should be verified with histology.

3.5.6 Detecting arterial softening in head trauma

The primary motivation for this work was to better understand possible changes to the cerebrovasculature in head trauma. The reported axial and circumferential softening provides us with meaningful insights, and the resulting constitutive models provide a means to approximate such softening computationally; however, it remains difficult to predict the prevalence of axial overstretch in TBI as the degree to which vessels deform *in vivo* is unknown. While hemorrhage clearly indicates that some vessels undergo high strains, it is unclear how localized these strains are. Therefore, having now correlated vessel stretch with changes in mechanics in the present work (Figures 3.2 and 3.3), this relationship could potentially be used to estimate peak axial deformations in experimental models of head trauma by evaluating isolated vessel response postinjury. However, proving the existence of softening in models of head impact would likely be difficult for a number of reasons. The primary of these reasons is that quantification of softening requires a predamage evaluation of mechanics; however, vessels can only be excised and tested after impact. An alternative approach would be to use a noninvasive imaging modality to measure vessel geometry before and after impact; however, this too falls short as measures of axial tension and internal pressure would be unavailable. A final approach might be to acquire control vessels from separate animals; however, not only does this bring into play sample-to-sample variability, but, in addition, overstretch has been shown to increase the unloaded length of arteries [57]. Preliminary analysis on eight datasets (not reported) suggests that this latter factor alone is sufficient to hide otherwise measureable softening as the softened axial stress-stretch response is nearly completely recovered when the postdamage data are plotted relative to the unloaded length of an

overstretched and softened vessel. Therefore, other approaches, likely involving some form of histological evaluation of microstructural damage, are likely needed to assess the magnitude of vessel overstretch in actual head trauma.

3.5.7 Limitations and future work

Our experimental approach deviated from that of Weisbecker et al. [60] in a few important ways. First, instead of using uniaxial tension tests, we used a biaxial tension test as, admitted by the authors themselves, it "is better able to mimic the physiological loading conditions" [60]. Doing so allowed us to develop the model on experimentally collected, rather than theoretically calculated, transverse loading data. Second, instead of subjecting the same sample to successively increasing levels of overstretch, we subjected each vessel to only a single overstretch. This avoided the potential of continuous softening from repeated loading, as this has not been studied, to our knowledge, in cerebral arteries. However, these modifications also bring some limitations to the results of our damage model.

The primary limitation of our damage model is the limited amounted of data available for characterizing the predamage response. The predamage response was only characterized over the range of $1.0*\lambda_{Z_{IV}}$ to $1.05*\lambda_{Z_{IV}}$. Because of our choice to carry out biaxial tests, stress-stretch data were limited to that collected above the axial *in vivo* stretch; pressurized vessels readily buckle between the unloaded and *in vivo* stretches, invalidating the assumption of cylindrical shape and homogeneous deformation. In addition, because of our desire to avoid repeated overloading of individual vessels, predamage characterizations stopped at $1.05*\lambda_{Z_{IV}}$. Due to the limited range of predamage

stress-stretch data, initial attempts to fit material parameters (using the predamage response) independent of the damage parameters (fit using the postdamage responses) resulted in poor fits of the softened curves. We overcame this by fitting pre- and postdamage data simultaneously, which resulted in an acceptable and comparable quality of fit for all curves. However, we believe that fitting material and damage parameters independently of each other is more ideal, and therefore, suggest that material parameters be fit to baseline characterizations spanning a larger strain rage. This could be accomplished in a number of ways. One approach, which we believe to be the most ideal, would be to characterize vessel behavior at subphysiological pressures (i.e., < 50 mmHg). This would allow mechanics to be explored at stretches below the axial *in vivo* stretch without inducing buckling, and provide a more complete picture of the nonlinearity of the predamage response. A second approach would be to include data from the single axial overstretch in the model optimization. However, we do not anticipate this would improve results significantly as vessel response becomes linear soon after the *in vivo* stretch, no longer following the exponential behavior of the fiber model. A third option would be to return to the method used by Weisbecker et al. [60], that is, characterize the biaxial mechanics with two sets of uniaxial tests; however, the aforementioned limitations would then apply.

The choice to avoid repeated loading caused a second limitation in our work. In order to characterize softening following a range of overstretches, data from multiple samples had to be used simultaneously in order to quantify the evolution of damage with overstretch. Use of multiple samples brings with it the inherent variability of biological tissue. However, normalization of the data by each sample's *in vivo* configuration

produced predamage curves with surprisingly similar slopes (Figures 3.4b and 3.5b) and monotonic changes in the softened response with increasing levels of overstretch (see experimental response in Figures 3.6 and 3.7). While we have no reason to believe that normalization affected our results, this step could potentially be avoided by resolving the limitation discussed in the preceding paragraph. If the model could be optimized in two stages (material parameters followed by damage parameters), then unique material parameters could first be fit to the predamage response of all vessels in their original (un-normalized) state. This would then be followed by finding a single set of damage parameters for the entire dataset simultaneously. While this approach would obviate the need for normalization, it still doesn't resolve our original limitation of the noise inherent to fitting a single set of damage parameters to multiple samples having inherent biological variability. To the best of our knowledge, this can only be avoided by, again, returning to the approach of Weisbecker et al. [60], that is, overloading a single sample to multiple levels of overstretch. However, prior to doing this, the degree to which repeated loading introduces continuous softening should first be understood. In addition, future studies would also be enhanced by the inclusion of the unloading data in model fitting.

One final limitation of the study is that vessel overstretch was conducted at quasi-static rates. Vessel loading rates in head injury are not known; however, brain tissue strain rates have been estimated to range from 10 to 100 s^{-1} in conventional TBI [17, 18, 79, 80]. We have previously shown strain rate to have little significance on the mechanical, including failure, properties of human cerebral arteries and veins over four orders of magnitude (0.01 to 500 s^{-1}; [23]). However, as the effect of rate on subfailure damage has not yet been explored in arteries, we are unable to conclude how our results

might be different following higher rates of damage. One study in ligament, however, found greater softening following high rate subfailure overstretch [45].

3.6 Conclusion

In vitro experiments on cerebral arteries are crucial to better understanding changes in vascular mechanics that may occur in TBI. In this study, the effect of overstretch on passive biaxial mechanics was explored in isolated sheep middle cerebral arteries. Changes in vessel stiffness, strain energy, and stretch were evaluated following various levels of subfailure axial overstretch. In addition to previous reports showing an increase in axial compliance [57], we found vessels to soften in the circumferential direction. These passive changes may account for up a 5% decrease in vascular resistance and likely play a role in, though do not fully explain previous reports of, cellular dysfunction [67].

In addition to quantifying softening, experimental data were collected at various combinations of luminal pressures and axial stretches so that data could be fit with a constitutive model. A recently proposed pseudo-elastic damage model was implemented for two reasons. First, as the model had only been previously validated with data from uniaxial tensile tests, we wanted to test the ability of the model to fit data from more physiological, multiaxial loading tests. Second, as the model is, to our knowledge, the only existing structurally-motivated damage model for arteries, we hoped to elucidate stretch-induced changes in the collagen fiber fabric. Results showed that the model appropriately captured the direction of stress and stretch changes following overstretch in both axial and circumferential loading; however, it was unable to properly model the

magnitude of these changes across all levels of overstretch. Observations on fiber-specific mechanics and damage are made, though, as the model did not represent the data precisely, recommendations are made to determine whether errors are due to experimental methodology or limitations in the damage model itself. Regardless, our experimental results provide a first characterization of biaxial softening of cerebral arteries in axial overstretch, and the proposed parameters of the damage model provide a means for representing this behavior computationally for limited cases.

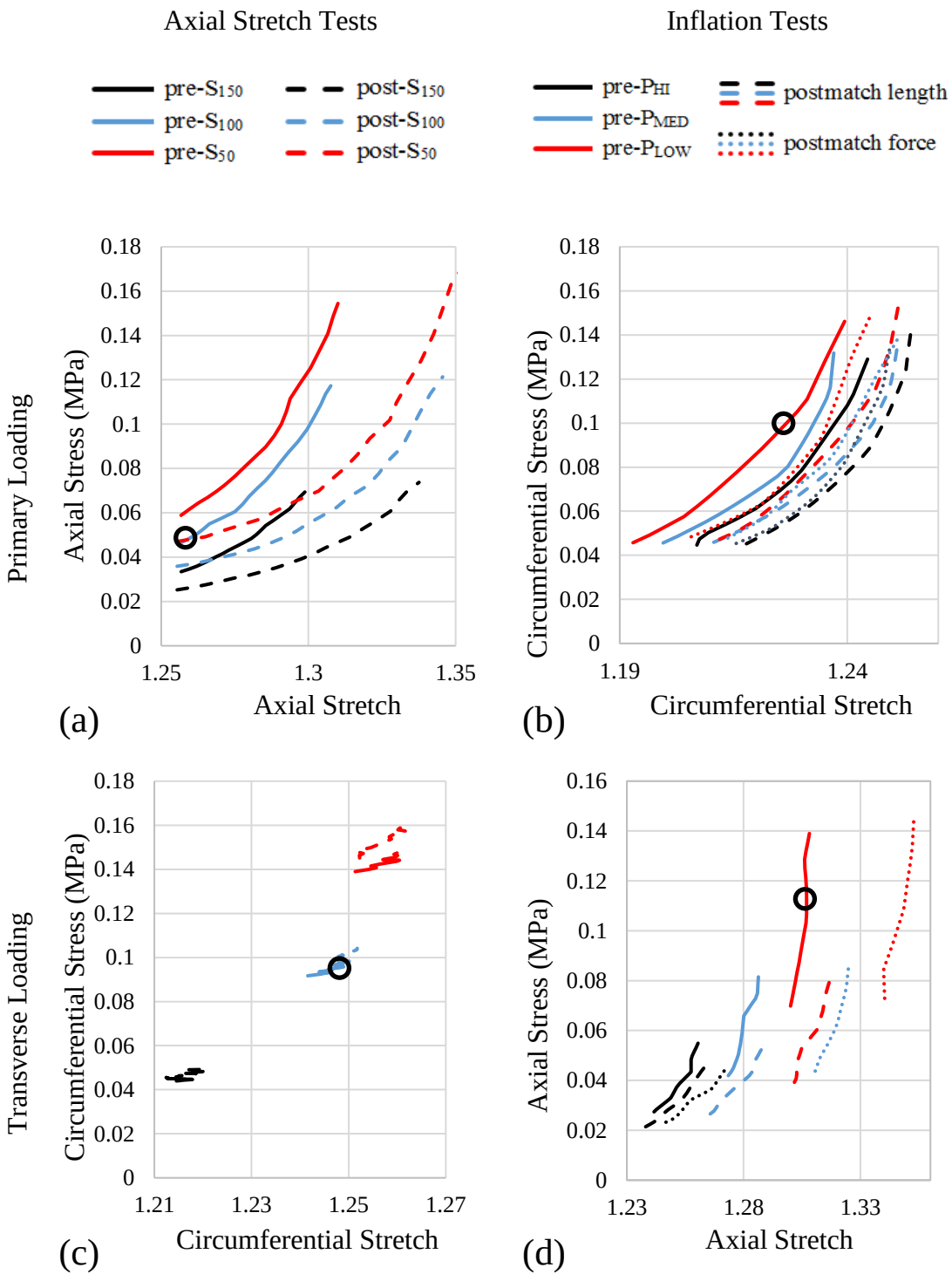

Figure 3.1: Representative pre- and postdamage Cauchy stress-stretch curves for axial stretch (a, c) and inflation (b, d) tests taken from a sample subjected to a single axial overstretch 22% beyond the axial *in vivo* stretch. The black circle in each graph marks the *in vivo* configuration.

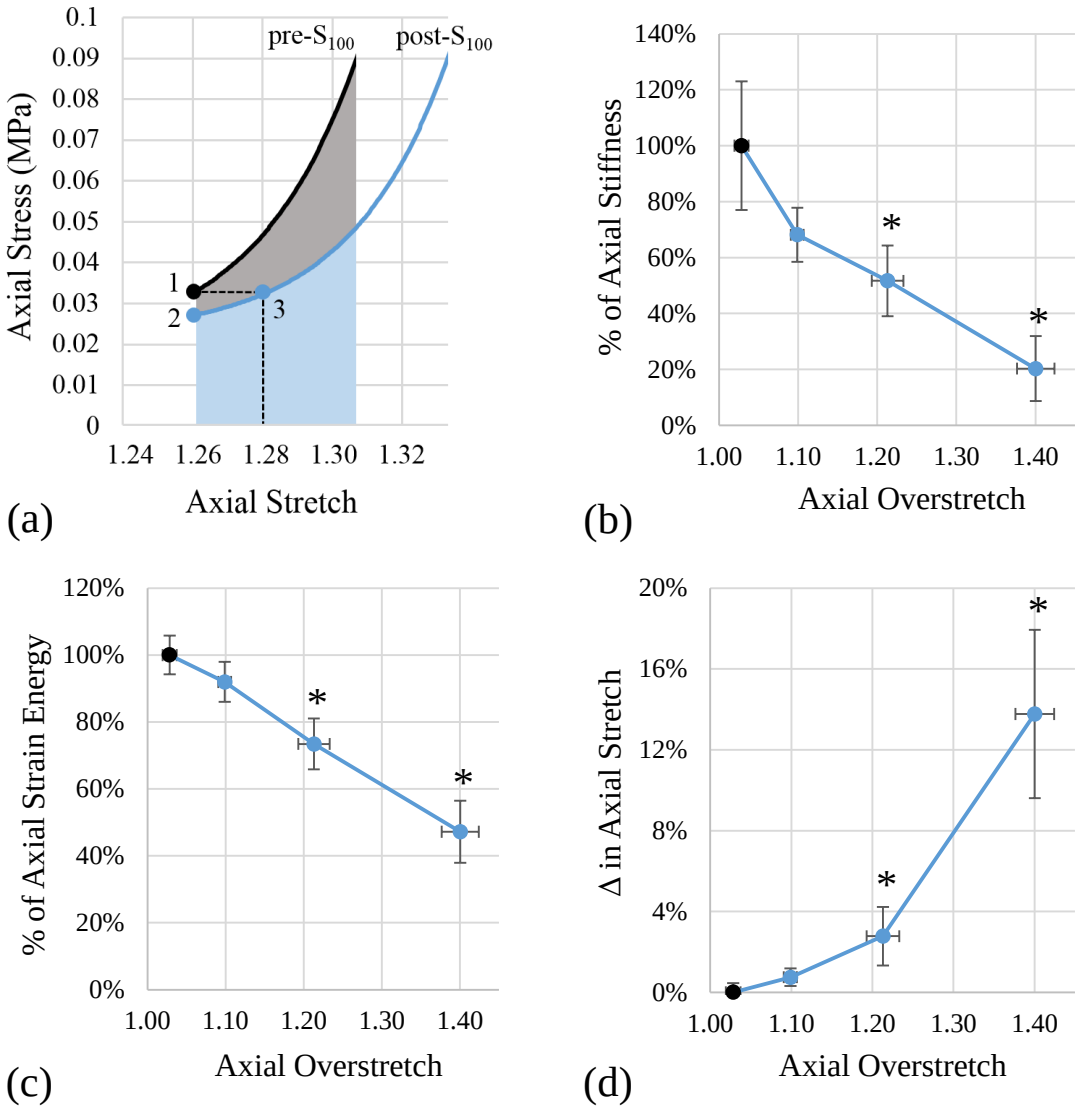

Figure 3.2: Axial softening metrics. Axial softening was observed following axial overstretch for all three measures quantified. (a) Representative pre- (black line) and postdamage (blue line) axial stress-stress curves showing key points where softening was quantified. The *in vivo* configuration is denoted by Point 1. (b) Decrease in axial *in vivo* stiffness with overstretch. Stiffness was quantified at the axial *in vivo* stretch (points 1 and 2 in (a)). (c) Decrease in axial strain energy with overstretch. Strain energy was quantified in the shaded regions under the curves in A (bound by the predamage axial *in vivo* stretch and the upper limit of the baseline characterization). (d) Increase in vessel axial stretch at the baseline stress (predamage *in vivo* stress; Points 1 and 3). Softening was statistically significant ($p < 0.05$, relative to the control data point in black) at 20% and 40% overstretch for all three metrics (*). Note that x-axes in (b), (c), and (d) are relative to the axial *in vivo* stretch. Error bars represent one standard deviation from the mean.

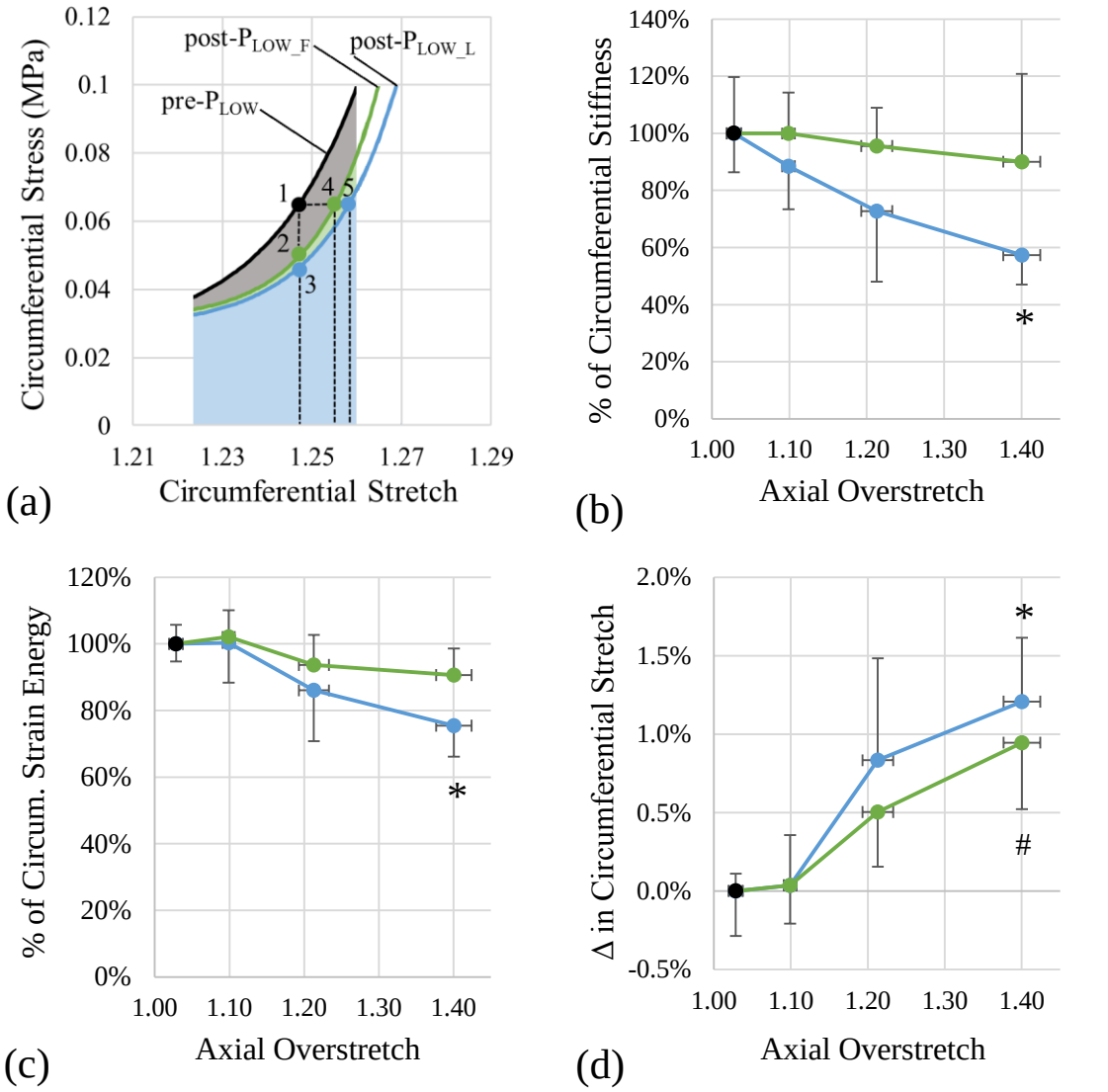

Figure 3.3: Circumferential softening metrics. Circumferential softening was observed following axial overstretch for all three measures quantified. (a) Representative pre- (black line) and postdamage (blue: matched axial stretch; green: matched axial force) circumferential stress-stress curves showing key points where softening was quantified. The *in vivo* configuration is denoted by Point 1. (b) Decrease in circumferential *in vivo* stiffness with overstretch. Stiffness was quantified at the circumferential *in vivo* stretch (points 1, 2, and 3 in (a)). (c) Decrease in circumferential strain energy with overstretch. Strain energy was quantified in the shaded regions under the curves in (a) (bound by the predamage circumferential stretch at 50 and 150 mmHg). (d) Increase in circumferential stretch at the baseline stress (Points 1, 4, and 5). Softening was statistically significant ($p < 0.05$, relative to the control data point in black) at 40% overstretch for all three metrics when evaluated at the predamage axial stretch (*) and a change in circumferential *in vivo* stretch was found at 40% overstretch when evaluated at the predamage axial tension (#). Note that x-axes in (b), (c), and (d) are relative to the axial *in vivo* stretch. Error bars represent one standard deviation from the mean.

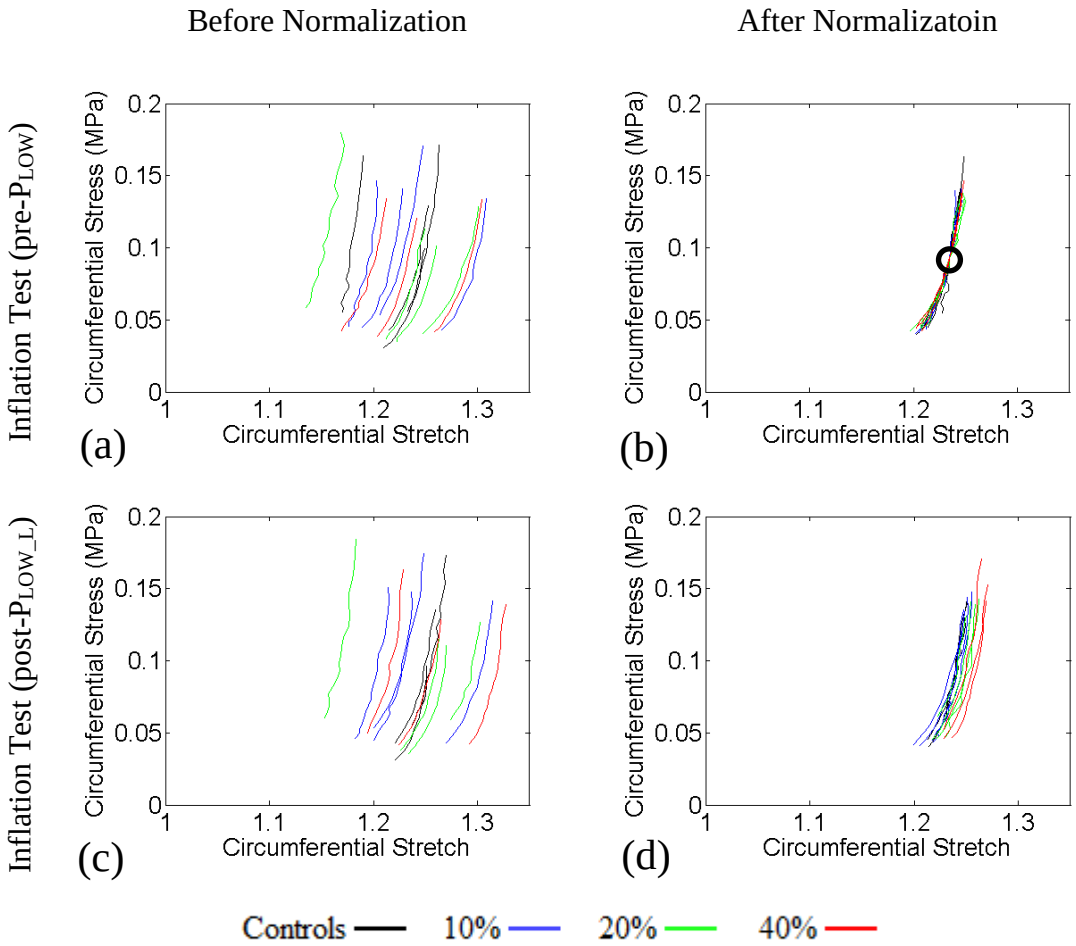

Figure 3.4: Normalization of inflation tests. Graphs showing the difference in alignment of stress-stretch data from pre- (top row) and postdamage (bottom row) inflation tests before (left) and after (right) normalization. As all data were scaled by their predamage *in vivo* configuration, normalized data intersect at the population mean (circled) for predamage tests (b). Scaling of postdamage data by the same predamage factors ultimately served to reduce the variability in softened responses for each of the four stretch groups (d). Controls are shown in black, while samples subjected to 10%, 20%, and 40% overstretch are shown in blue, green, and red, respectively. A similar alignment was observed for the predamage transverse data (axial direction) and predamage data from non-P_{LOW} inflation tests (not shown).

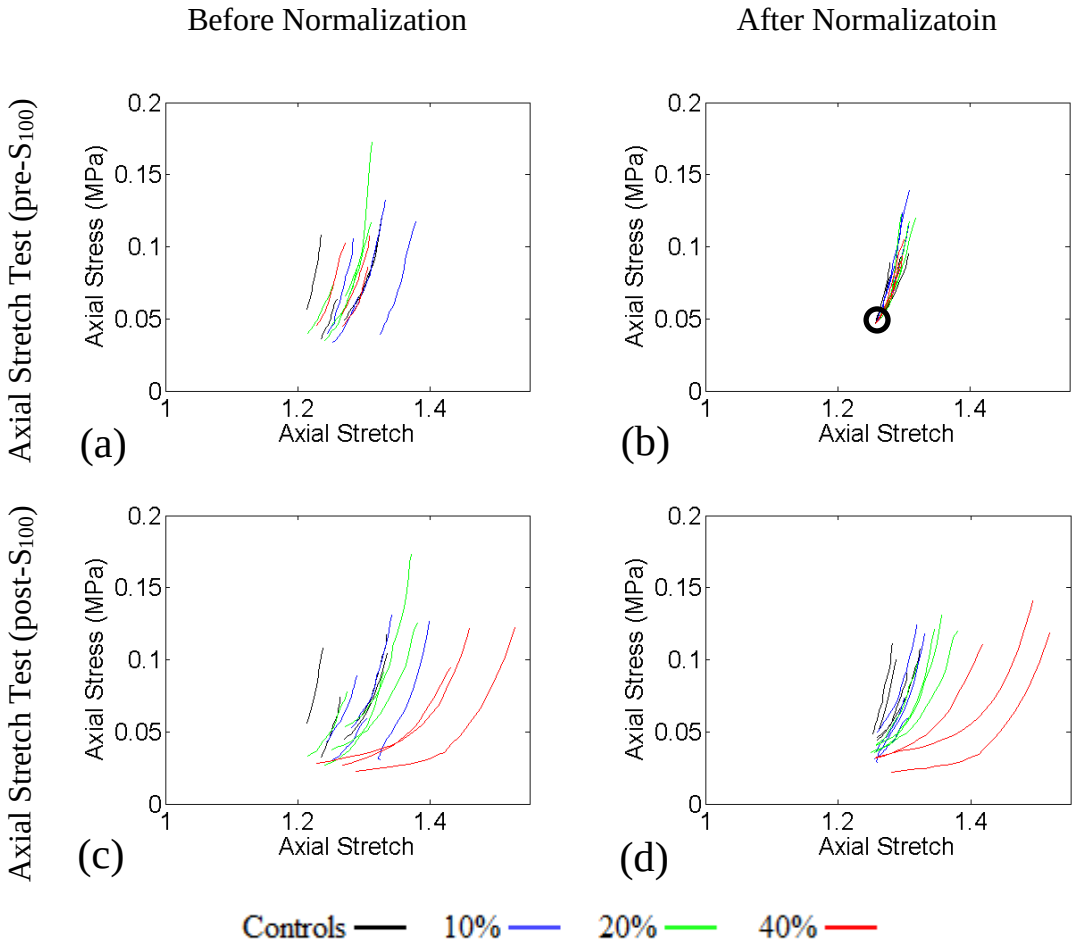

Figure 3.5: Normalization of axial stretch tests. Graphs showing the difference in alignment of stress-stretch data from predamage (top row) and postdamage (bottom row) axial stretch tests before (left) and after (right) normalization. As all data were scaled by their predamage *in vivo* configuration, normalized data intersect at the population mean (circled) for predamage tests (b). As with inflation test data, scaling of postdamage data by the predamage factors reduced the variability in softened responses for each of the four stretch groups (d). Controls are shown in black, while samples subjected to 10%, 20%, and 40% overstretch are shown in blue, green, and red, respectively. A similar alignment was observed for the predamage transverse data (circumferential direction) and predamage data from non-S_{100} axial stretch tests (not shown).

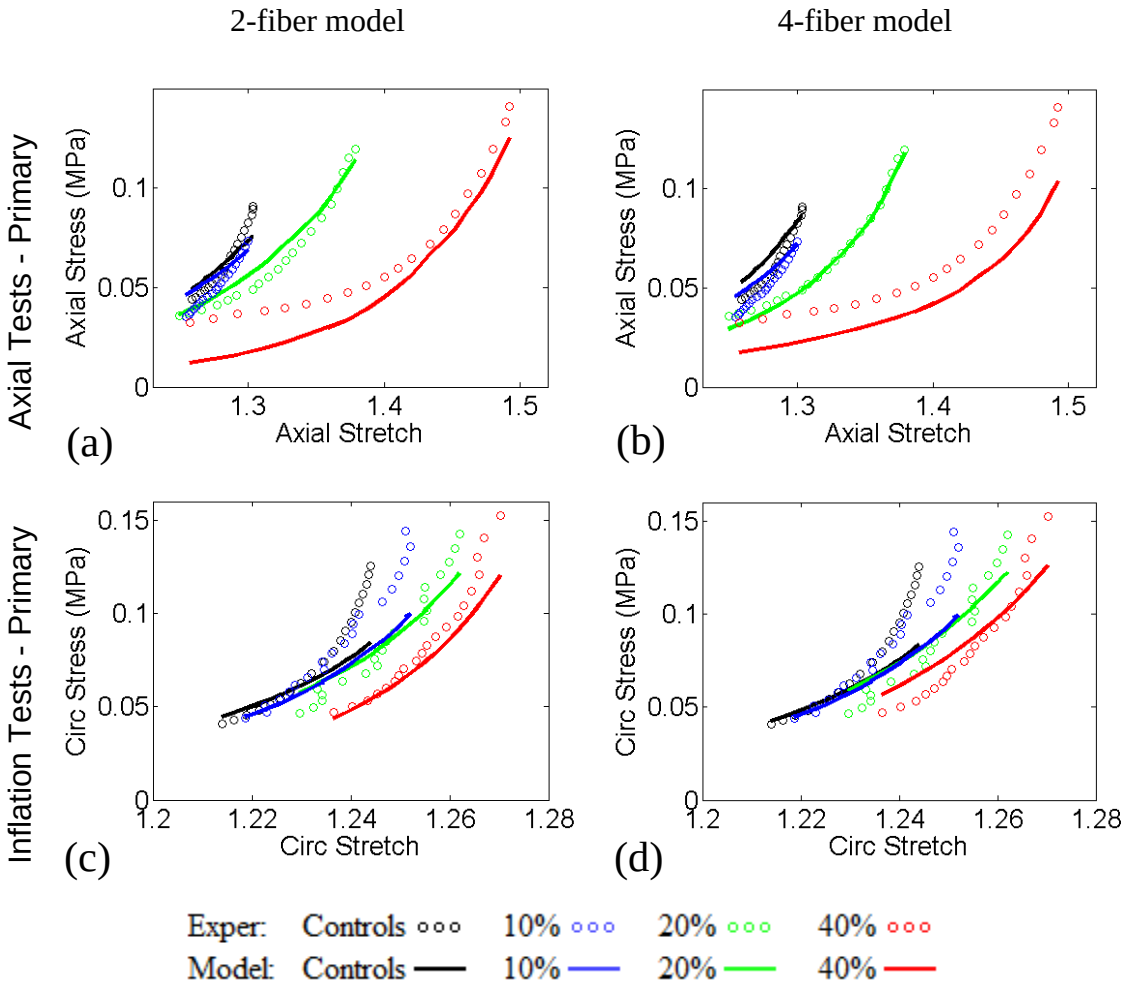

Figure 3.6: Model fits on primary loading data. Representative postoverstretch experimental Cauchy stress-stretch data (open circles) and model fits (solid lines) for the 2-fiber (left panel) and 4-fiber (right panel). The top row shows the axial loading response during axial stretch tests at *in vivo* pressure ('post-S_{100}'). The bottom row shows the circumferential loading response during inflation tests at the axial *in vivo* stretch ('post-P_{LOW_L}'). Data from control, 1.10*λ_{Z_IV}, 1.20*λ_{Z_IV}, and 1.40*λ_{Z_IV} groups are shown in black, blue, green, and red, respectively. Note that 'postoverstretch' data from the control group were used to fit the predamage response.

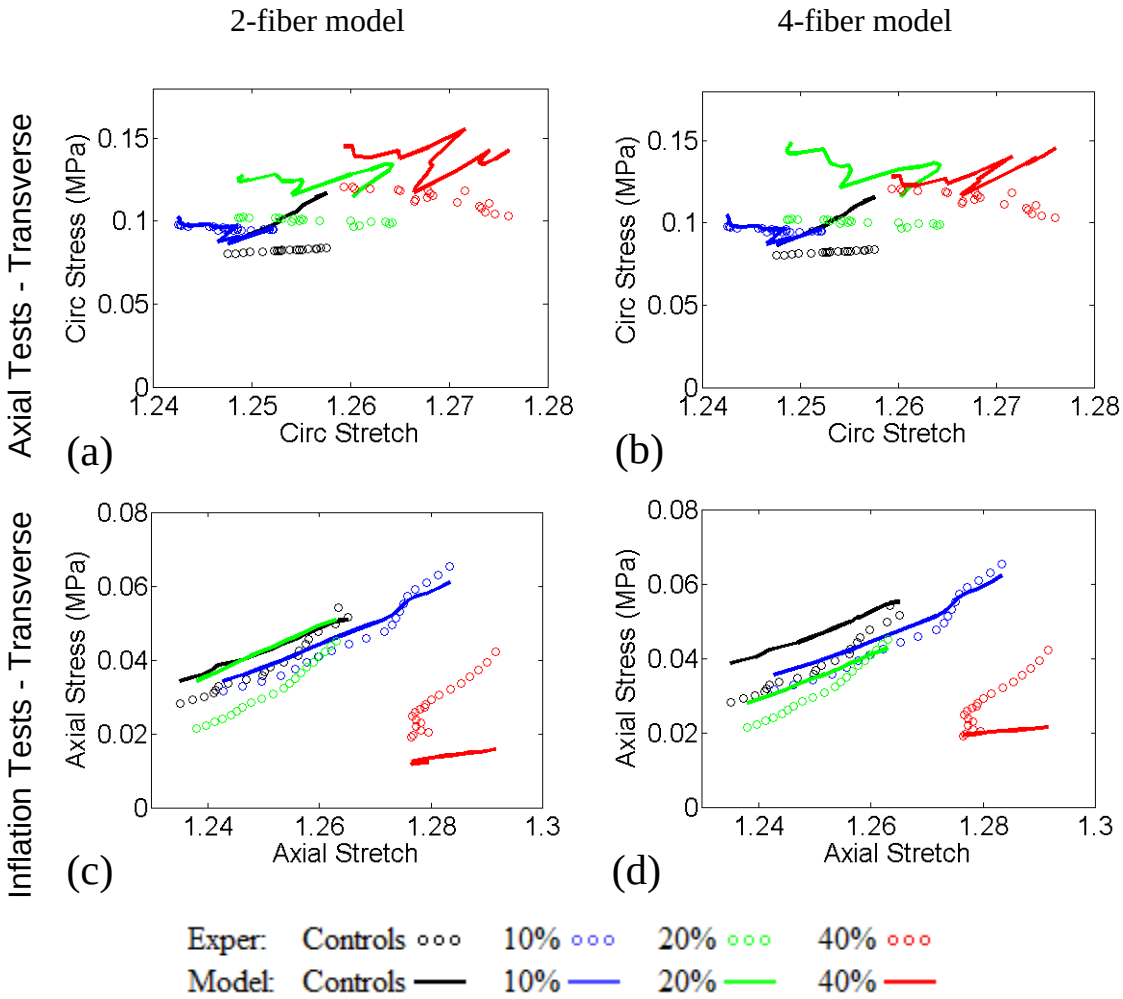

Figure 3.7: Model fits of transverse loading data. Representative postoverstretch experimental Cauchy stress-stretch data (open circles) and model fits (solid lines) for the 2-fiber (left panel) and 4-fiber (right panel) models in the transverse loading directions. The top row shows the circumferential response during axial stretch tests at *in vivo* pressure ('post-S_{100}'). The bottom row shows the axial response during inflation tests at the axial *in vivo* stretch ('post-P_{LOW_L}'). Data from control, 1.10*λ_{Z_IV}, 1.20*λ_{Z_IV}, and 1.40*λ_{Z_IV} groups are shown in black, blue, green, and red, respectively. Note that 'postoverstretch' data from the control group were used to fit the predamage response.

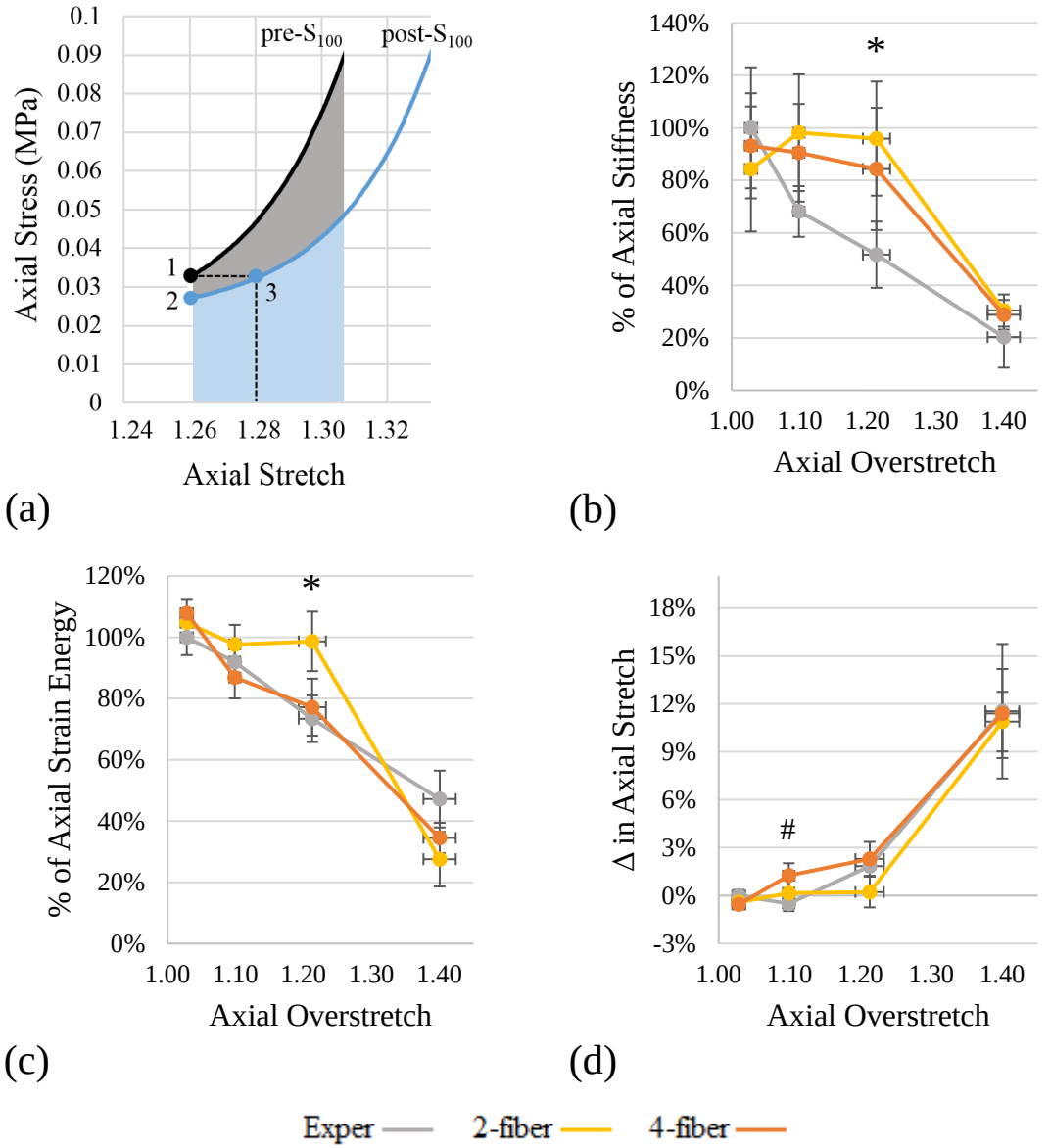

Figure 3.8: Comparison of experimental and computational axial softening metrics. Comparison of axial softening observed experimentally in axial stretch tests conducted at *in vivo* pressures (gray lines in (b)-(d), previously presented in Figure 3.2) overlaid with simulated results of the same tests from the 2-fiber (yellow) and 4-fiber (orange) models. Previously shown graphic from Figure 3.2a is copied to show where softening was measured (a). The models reasonably tracked the overall softening behavior but generally underestimated changes in the stiffness at the axial *in vivo* stretch (b). Furthermore, the 2- and 4-fiber models were statistically different from experimental results in measures of strain energy following 20% overstretch (c) and stretch at baseline stress following 10% overstretch (d), respectively. Significant differences ($p < 0.025$) from post hoc t-tests are denoted by '*' (2-fiber model) and '#' (4-fiber model). Error bars represent one standard deviation from the mean.

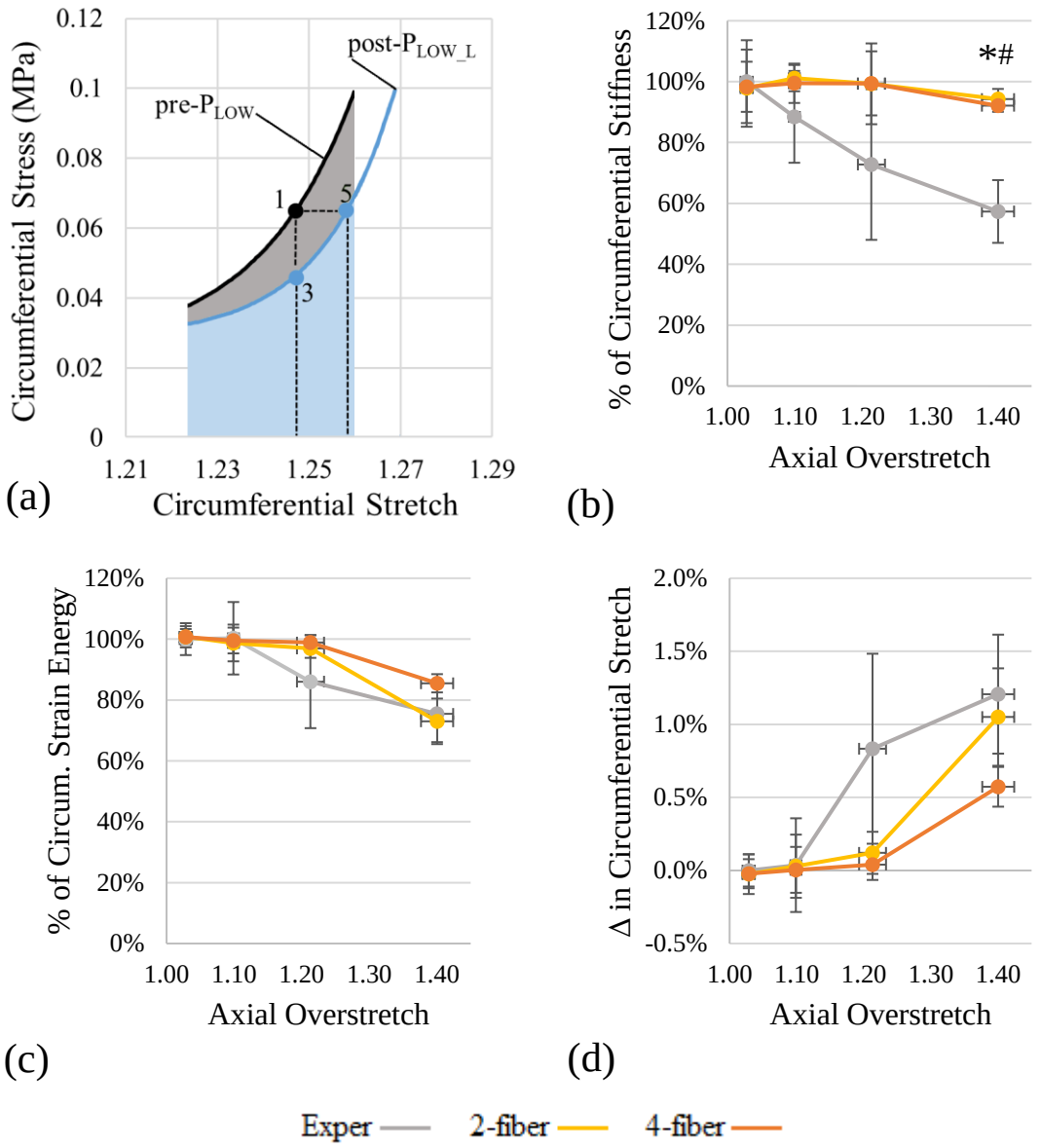

Figure 3.9: Comparison of experimental and model circumferential softening metrics. Comparison of circumferential softening observed experimentally in inflation tests conducted at the predamage axial *in vivo* stretch (gray lines in (b)-(d), previously presented with blue lines in Figure 3.3) overlaid with simulated results of the same tests from the 2-fiber (yellow) and 4-fiber (orange) models. Previously shown graphic from Figure 3.3a is copied to show where softening was measured (a). The models reasonably tracked the general circumferential softening behavior but significantly underestimated changes in the stiffness (b). No other statistically significant changes were observed; however, both models underestimated changes in strain energy (c) and circumferential stretch at the baseline (*in vivo*) stress following 20% overstretch (d). Significant differences ($p < 0.025$) from post hoc t-tests are denoted by '*' (2-fiber model) and '#' (4-fiber model). Error bars represent one standard deviation from the mean.

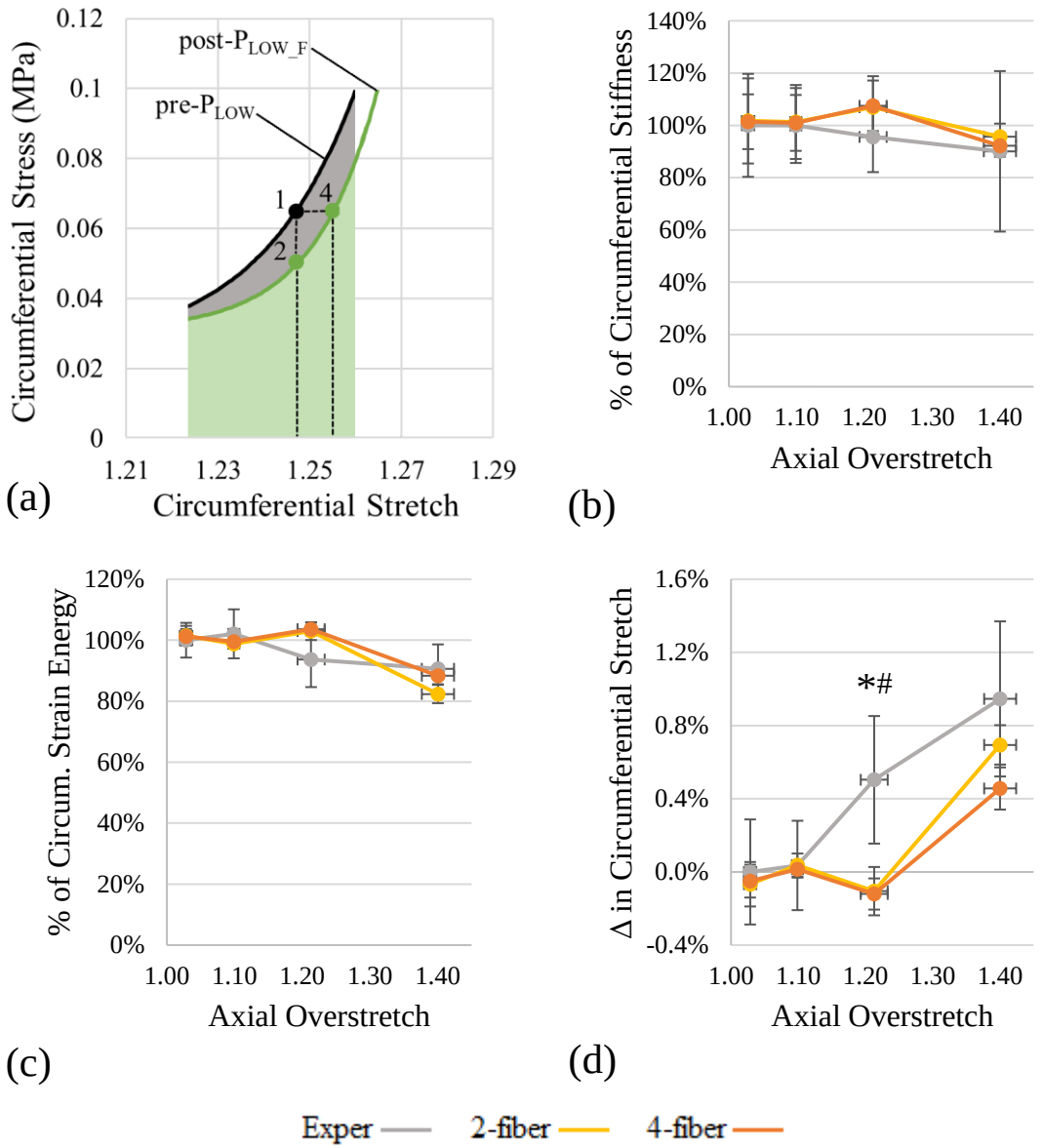

Figure 3.10: Comparison of experimental and model circumferential softening metrics. Comparison of circumferential softening observed experimentally in inflation tests conducted at the predamage axial *in vivo* tension (gray lines in (b)-(d), previously presented with green lines in Figure 3.3) overlaid with simulated results of the same tests from the 2-fiber (yellow) and 4-fiber (orange) models. Previously shown graphic from Figure 3.3a is copied to show where softening was measured (a). As in Figures 3.8 and 3.9, the models reasonably tracked the general circumferential softening behavior but, in a few cases, underestimated the degree of softening. This was especially true following 20% overstretch (b, c, and d), though changes were only statistically significant for measures of the change in circumferential stretch (d). Significant differences ($p < 0.025$) from post hoc t-tests are denoted by '*' (2-fiber model) and '#' (4-fiber model). Error bars represent one standard deviation from the mean.

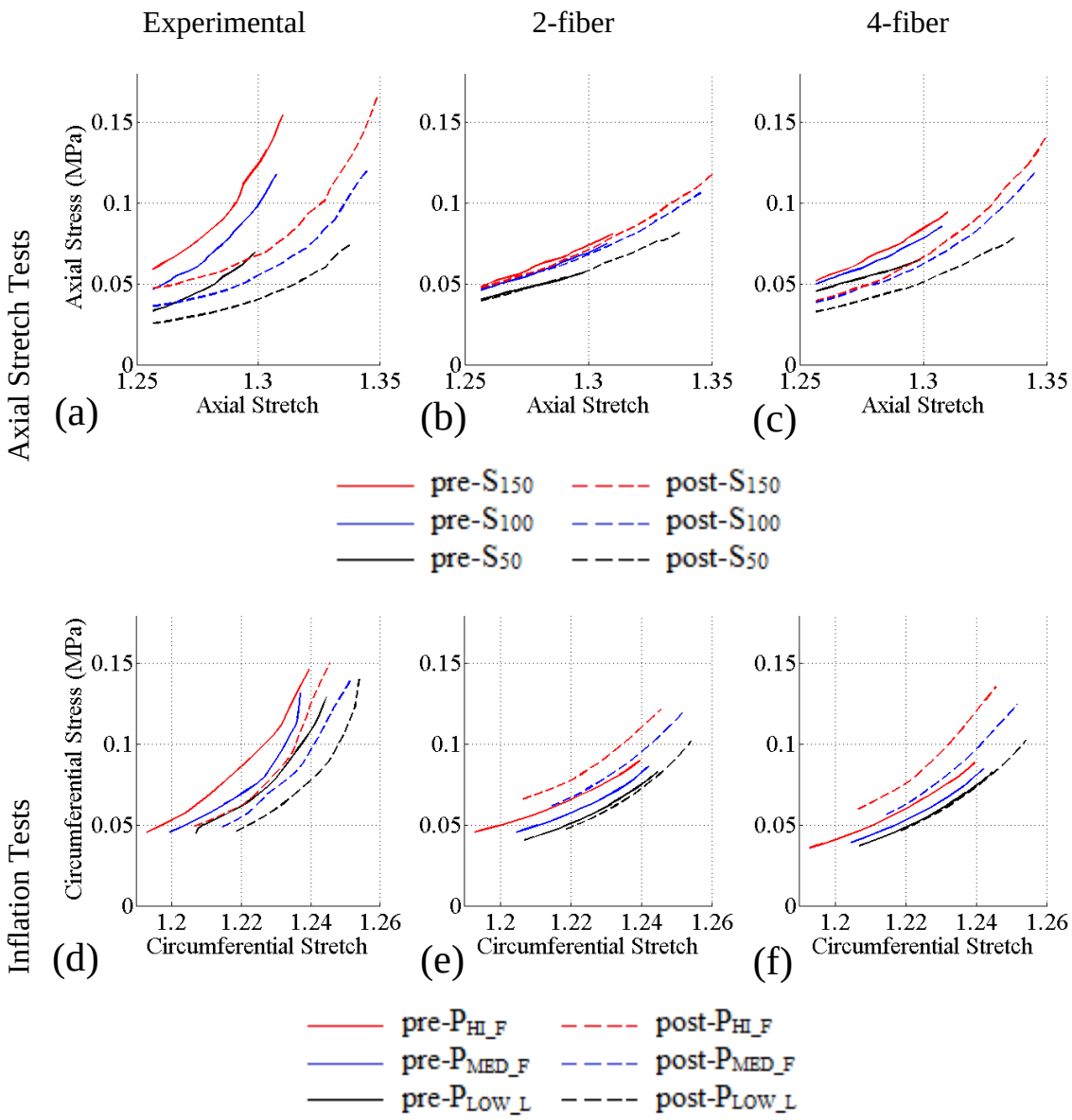

Figure 3.11: Comparison of experimental and model biaxial interactions. Graphs demonstrating the biaxial effects observed experimentally (left column) compared to those demonstrated by the 2- (middle column) and 4-fiber models (right column) for a representative sample overstretched 22%. In general, the model appropriately captured the direction of biaxial interactions but didn't fully match the magnitude of these changes. Specifically, the model underestimated increases in axial stress caused by increases in pressure (a-c) and underestimated circumferential changes in stretch/stress due to increases in axial stretch in the predamage response (d-f). Note that only three of the six postoverstretch inflation tests are shown as only three were used in the model optimization ('post-P_{HI_F}', 'post-P_{MED_F}', and 'post-P_{LOW_L}' as they were the three which most evenly spanned the axial strain range used during characterization).

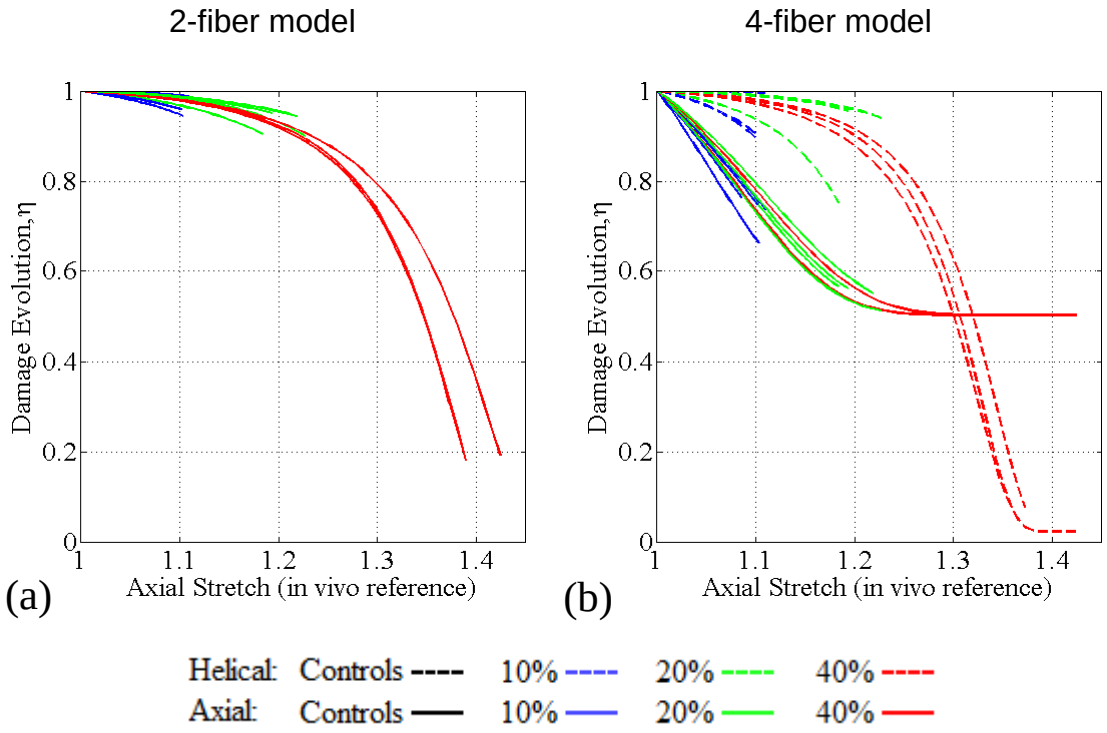

Figure 3.12: Collagen fiber damage evolution. Damage evolution with vessel stretch for the 2-fiber (a) and 4-fiber (b) models during axial overstretch at *in vivo* pressure. (a) The evolution of damage in the axial fiber family (having distributed fiber angles) for the 2-fiber model for all samples from the 10% (blue), 20% (green), and 40% (red) overstretch groups. (b) The evolution of damage in the axial (solid lines) and helical (dashed lines) families for the 4-fiber model for all samples. The list of samples plotted and their respective colors are the same as in (a).

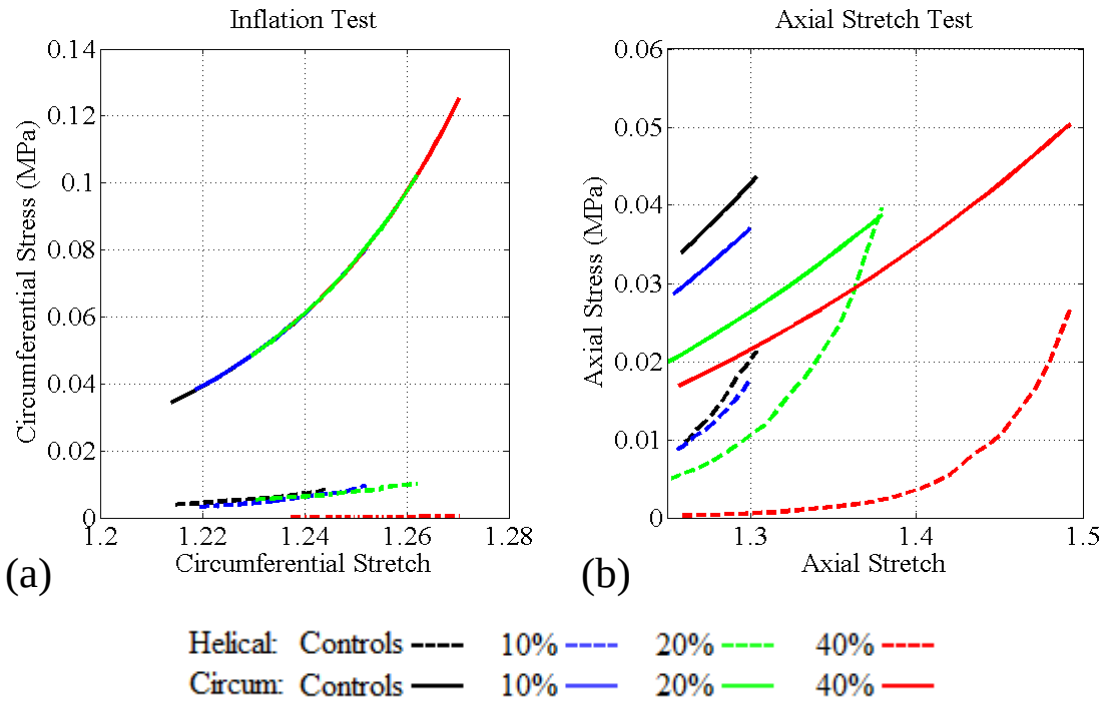

Figure 3.13: Stresses borne by individual collagen fiber families (4-fiber model). Cauchy stresses borne by circumferential, axial, and one of the two symmetric helical fiber families before (black lines) and after 10% (blue), 20% (green), and 40% (red) overstretch. (a) Representative circumferential stress-stretch data from simulated inflation tests at the axial *in vivo* stretch for circumferential (solid lines) and helical (dashed lines) families. As damage was not allowed to evolve in the circumferential fibers, the pre- and postdamage responses lie on top of each other. However, as damage was incurred in the helical family (Figure 3.12b), stresses borne by the fibers decrease for each increasing level of overstretch (10%, 20%, and 40%). This demonstrates that circumferential stress softening is due to softening of helical fibers. Note that the sum of circumferential + 2*helical stresses yields the model stresses presented in Figure 3.6d. (b) Representative axial stress-stretch data from simulated axial stretch tests carried out at *in vivo* pressure. As damage was incurred in both axial and helical fibers (Figure 3.12b), both show softening with each increasing level of overstretch. Evaluating the degree of softening around the axial *in vivo* stretch (left edge of traces) suggests that the majority of axial stress softening is due to softening of the axial fibers. Note that the sum of axial + 2*helical stresses yields the model stresses presented in Figure 3.6b.

Table 3.1: Population *in vivo* stretches and stresses (mean ± SD) used in the normalization of inflation and axial stretch tests data. Values were used in the calculation of sample-specific scaling factors in Equation 3.10.

	$\overline{\lambda_{\theta_{IV}}}$	$\overline{\lambda_{Z_{IV}}}$	$\overline{T_{\theta_{IV}}}$ (MPa)	$\overline{T_{Z_{IV}}}$ (MPa)
Inflation Tests	1.23 ± 0.04	1.26 ± 0.03	0.093 ± 0.015	0.043 ± 0.008
Axial Stretch Tests	1.24 ± 0.04	1.26 ± 0.03	0.092 ± 0.022	0.047 ± 0.010

Table 3.2: Optimal parameters for the 2-fiber model.

Material parameters					Damage parameters	
k_1^1 (kPa)	k_1^2 (kPa)	k_2^1	k_2^2	κ_2	r_2	m_2
1.50	118	9.55	10.2	0.308	1.00	0.110

Table 3.3: Optimal parameters for the 4-fiber model.

Material parameters							Damage parameters			
k_1^1 (kPa)	k_1^2 (kPa)	$k_1^{3,4}$ (kPa)	k_2^1	k_2^2	$k_2^{3,4}$	φ (deg)	r_2	$r_{3,4}$	m_2	$m_{3,4}$
6.18	18.3	0.803	6.18	1.02e-2	7.50	47.1	2.00	1.02	9.40e-3	1.33e-2

Table 3.4: Average absolute error for both models grouped by level of overstretch.

	Control	1.1*L_{IV}	1.2*L_{IV}	1.4*L_{IV}	mean
2-fiber	19.8%	17.2%	21.2%	19.7%	19.5%
4-fiber	19.4%	17.1%	17.4%	18.0%	18.0%

Table 3.5: Average absolute error for both models grouped by type of loading and directionality of stress-stretch data.

	Axial Stretch Test		Inflation Test		
	Axial	Circumferential	Circumferential	Axial	mean
2-fiber	21.1%	22.9%	14.3%	19.5%	19.5%
4-fiber	18.6%	22.7%	14.5%	16.1%	18.0%

CHAPTER 4

DETECTION AND CHARACTERIZATION OF MOLECULAR-LEVEL COLLAGEN DAMAGE IN OVERSTRETCHED CEREBRAL ARTERIES

4.1 Abstract

It is well established that overstretch of arteries alters their mechanics and compromises their function. However, the underlying structural mechanisms behind these changes are poorly understood. Utilizing a recently developed collagen hybridizing peptide (CHP), we demonstrate that a single mechanical overstretch of an artery produces molecular-level unfolding of collagen. In addition, imaging and quantification of CHP binding revealed that overstretch produces damage (unfolding) among fibers aligned with the direction of loading, that damage increases with overstretch severity, and that the onset of this damage is closely associated with tissue yielding. These findings held true for both axial and circumferential loading directions. Our results are the first to identify stretch-induced molecular damage to collagen in blood vessels. Furthermore, our approach is advantageous over existing methods of collagen damage detection as it is nondestructive, readily visualized, and objectively quantified. This work opens the door to revealing additional structure-function relationships in arteries. We anticipate that this approach can be used to better understand arterial damage in clinically relevant settings

such as angioplasty and vascular trauma. Furthermore, CHP can be a tool for the development of microstructurally-based constitutive models and experimentally validated computational models of arterial damage and damage propagation across physical scales.

4.2 Introduction

Arteries play a critical role in carrying essential nutrients and oxygen throughout the body. However, both trauma and surgical interventions such as angioplasty, can distend arteries beyond their physiological range. Even in the absence of hemorrhage, such 'subfailure' deformations can cause cellular damage [77, 81, 82] and permanent deformation of the tissue [82, 83], leading to compromised vessel function [84]. Furthermore, experimental and computational work has demonstrated that overstretch alters arterial passive mechanics in cases of both axial [57-60] and circumferential [60, 61, 85] loading. This alteration is characterized by a softening of the tissue stress-stretch behavior, or, an increase in wall compliance.

A key vascular constituent in all of these processes is collagen. Not only do collagen fibers dominate the passive mechanical behavior of arteries at high strains [38, 75], but they also transfer exogenous loads to cells [86]. Therefore, damage to collagen may alter cellular signaling and, similarly, endogenous loading originating in cells may not transfer properly to the extracellular matrix.

Despite the key role of collagen in arterial mechanics, there is limited understanding of collagen damage following overstretch. The majority of findings come from research on the effects of angioplasty, with investigators using electron microscopy to observe dehiscence [87] and tearing [88, 89] of collagen fibers. Even less is known

about collagen damage following axial (longitudinal) loading, with one report of macroscale tears in the tissue following repeated tensile strains yet with little investigation of the damaged structures [50]. The limited insight on structural damage in arteries is largely due to the lack of an objective assay to detect and localize collagen damage in a quantitative fashion.

We recently demonstrated a new method of identifying molecular-level damage in collagen matrix that employs collagen hybridizing peptide (CHP) specifically binding to denatured collagen strands [90-92]. CHP is a synthetic peptide with a collagen-mimicking Glycine(G)-Proline(P)-Hydroxyproline(O) repeating sequence, and has a strong propensity to form the triple helical structure of collagen. As a result, a CHP strand can effectively bind to unfolded collagen chains through triple helix formation, whereas such binding sites are not present in intact collagen, making CHP a promising probe for detecting mechanically-induced unfolding of collagen. Previously, we reported that single-strand CHP with the sequence $(GPO)_9$ can hybridize to unfolded collagen strands that have been denatured by heat, protease activity [90, 91], or most recently, large deformations [92]. We also demonstrated that CHP has negligible affinity to intact collagen and virtually no nonspecific binding to noncollagenous proteins in tissues [93, 94] due to its neutral and hydrophilic sequence [90, 91]. Given that the presence of unfolded collagen molecules has been suggested in connective tissues (e.g., tendon) subject to heavy loading [92, 95-98], we hypothesized that individual collagen molecules can be unfolded in overstretched arterial tissue and that such collagens can be probed by CHP.

Here we present the quantitative staining of overstretched arteries with a solution

of fluorescently-labeled CHP, testing both the presence of unfolded collagen and the efficacy of the CHP probe. Furthermore, we leverage this novel marker to characterize the location, orientation, concentration, and stretch thresholds of damaged (unfolded) collagen within arteries following various levels of axial and circumferential loading. Finally, we use these results to demonstrate a close association between changes in tissue-level material properties and molecular-level collagen disruption. Studies are carried out in cerebral arteries for the potential translation of findings to cerebral angioplasty and brain trauma. Results for each objective are reported in detail and, as successful preliminary results in arteries prompted a parallel study in rat tail tendon fascicles [92], comparable findings are noted. Finally, the advantages of this technique over existing technology, its potential as a tool for better understanding vascular damage in both trauma and clinical interventions, and the role of molecular-level damage in arterial softening are discussed.

4.3 Materials and methods

4.3.1 Mechanical testing of axially overstretched samples

Sheep heads (n=5) were obtained from a local slaughterhouse immediately after death and transported to the lab on ice. Within 5 hrs of death, the brains were removed and the middle cerebral arteries (MCAs) were dissected from the brain, taking care to remove surrounding connective tissue. Straight lengths of each MCA were cut into 3-5 mm segments (n=21), and branches of these segments were ligated with unwound 6-0 suture. Reference cross-sectional area (A) was measured from unloaded vessel cross-sections cut from the end of each segment. Segments were bathed in PBS throughout the

dissection and testing process.

Mechanical testing was performed with a custom-made pressure myograph system described previously [67]. Briefly, each segment was cannulated with hypodermic needles and secured with 6-0 suture and cyanoacrylate glue. Microspheres were applied to the adventitial surface to allow determination of local strains. Vessel segments were perfused with room temperature PBS.

Following mounting, segments were preconditioned by oscillating the luminal pressure (0-20 kPa; 0-150 mmHg) for five cycles while length was held constant. Preconditioning cycles were repeated at gradually increasing lengths while actively monitoring variations in axial force with pressure. The axial *in vivo* length (L_{IV}) was identified as the length at which pressure cycles had a negligible effect on the tensile load [99], and the appropriateness of this estimate was evaluated as additional inflation cycles were done at stretches up to 1.05*L_{IV} (roughly 1.03* L_{IV} in local axial strain). Variations in tensile loads were only evaluated during the fifth and final inflation cycle at each length so that preconditioning at each length (cycles 1-4) was complete prior to evaluating force. Samples were then returned to the *in vivo* length and subjected to a single, triangular wave, quasi-static axial overstretch while maintained at an internal pressure of 100 mmHg (13.3 kPa) and a rate of 0.1 mm/s (strain rate ≈ 0.025 s^{-1}, Figure 4.1). Ten samples were stretched to a variety of subfailure levels and four were pulled to failure. In order to distinguish remodeling-induced unfolding from stretch-induced unfolding (in subsequent CHP staining), six segments (at least one per brain) served as mechanical controls. These segments underwent the same protocol (dissection, preconditioning) but were not subjected to the triangular wave axial overstretch.

4.3.2 Mechanical testing of circumferentially overstretched samples

A sheep brain was acquired from the Lamb Intensive Care Unit (LICU) at the University of Utah after being euthanized with an overdose of Beuthanasia (MWI Veterinary Supply). All procedures met requirements established by the Institutional Animal Care and Use Committee at the University of Utah. Segments of MCA (n=5, 5-9 mm long) were similarly dissected and preconditioned using the same procedures as that described above. Proximal and distal cross-sections of each MCA were imaged, and wall thicknesses were measured and averaged to define segment reference wall thickness (H). Following preconditioning, segments were removed from the needles and cut into rings approximately 1 mm long (axial dimension, n=31, Figure 4.2). Rings were then individually cannulated with two adjacent 28 gauge hypodermic needles and, in a configuration similar to wire myography, distended circumferentially by a triangular wave displacement of one needle at a rate of 0.1 mm/s (strain rate $\approx 0.06\ s^{-1}$). Ten rings were stretched to a variety of subfailure levels and eleven were pulled to failure. Similar to that done in the axial overstretch experiments, a total of seven rings (at least one per preconditioned segment) underwent the same protocol (dissection, preconditioning) but were not subsequently cannulated with the 28 gauge needles as they were not overstretched (mechanical controls). Unloaded reference (W) and current (w) ring length were measured from images captured at 3 Hz with a digital video camera (PL-A641, Pixelink).

4.3.3 CHP staining for collagen damage

CHP labeled with the fluorophore 5-FAM (F-CHP) was obtained from 3Helix (catalog number: FLU300, Salt Lake City). Following mechanical testing, all vessel segments were stained with F-CHP to detect the unfolded collagen molecules [90]. Stock F-CHP was diluted with PBS to a concentration of 20 μM. Because the CHP slowly self-assembles into its own triple helix over time, losing its driving force to hybridize with collagen, its solutions must be heated to dissociate the trimers into single CHP strands before use. Therefore, CHP solutions were heated for 6 min using a hot plate set to 70 °C and subsequently cooled on ice for 2 min to room temperature and immediately used for staining. Vessel segments were incubated in 100 μL of the activated CHP solution for at least 1 hr at 4 °C. Samples were then rinsed (3 times in 300 μL of PBS for 10 min each at 4 °C), cut open longitudinally, laid flat on glass slides, and prepared for imaging with a mounting media (Fluoromount G; Southern Biotech) and cover slip.

4.3.4 Confocal imaging

Following staining, samples were imaged at 10× (512 × 512 pixels) using a laser scanning confocal microscope (Fluoview 1000, Olympus). Serial slices were taken in 2 μm increments, producing a z-stack through the entire wall. The CHP signal was excited with the 488 nm Argon gas laser. Using a custom MATLAB script, adjacent images were stitched together to form a single montage covering the full circumference of the vessel.

4.3.5 Quantification of tissue stretch

Stretch (λ) was used to characterize tissue deformations and was calculated as the ratio of current and reference dimensions. The *in vivo*, rather than unloaded, configuration was used as the stretch reference as previous work in our lab has shown that doing so reduces the sample-to-sample variability in mechanical response [68]. The reader is referred to Nye et al. [100] for approximate *in vivo* stretches of this tissue. Stretches in axially loaded samples were determined from needle displacements and calculated relative to the estimated *in vivo* length of each specimen using Equation 4.1

$$\lambda_Z = \frac{l}{L_{IV}} \tag{4.1}$$

where l is the current length of the sample. As mentioned earlier, the *in vivo* length (L_{IV}) was determined during preconditioning. In samples pulled to failure, maximum tissue stretch was measured just prior to loss of internal fluid pressure as, beyond this point, additional deformation was localized to the eventual failure site which was disregarded in the subsequent analysis. Stretches in circumferentially loaded ring samples were similarly calculated from needle displacements using Equation 4.2

$$\lambda_\theta = \frac{c}{C_{IV}} \tag{4.2}$$

where c is the current ring circumference and C_{IV} is the estimated *in vivo* circumference. Midwall ring circumferences were calculated according to Equation 4.3

$$c = 2x_n + \pi(D_n + H) \tag{4.3}$$

where x_n is the distance between the central axes of the two parallel needles and D_n is the needle diameter. As the thickness of the wall could not be measured during loading, the reference wall thickness, H, was used. Computational modelling showed this assumption to produce no more than 3% error in circumference measurements [101]. The *in vivo*

circumference was taken to be the ring circumference at the configuration during overstretch that produced equivalent wall stress (Equation 4.4) to that experienced when held at *in vivo* length and pressure (13.3 kPa) during preconditioning (Equation 4.5).

$$T_\theta = \frac{F_\theta}{2wH} \tag{4.4}$$

$$T_\theta = p_i \frac{d_i}{d_e - d_i} \tag{4.5}$$

In Equation 4.4, T_θ refers to the mean circumferential Cauchy stress, F_θ is the experimental force measured by the load cell, and w is the current ring length (axial dimension). In Equation 4.5, p_i refers to the internal pressure and d_i and d_e to the vessel current inner and outer diameters, respectively. Controls were slightly overstretched during preconditioning as internal pressures were cycled above the *in vivo* pressure (Appendix A). However, as controls were never cannulated with the parallel hypodermic needles, their maximum overstretch was simply calculated from the change in diameter as captured by video during preconditioning.

4.3.6 Quantification of collagen damage

The CHP signal was qualitatively evaluated through the entire z-stack (approximately 20 slices) and a single slice within each stack was objectively quantified. The slice quantified was taken from within the media for circumferentially loaded samples and within the adventitia for axially loaded samples. As cerebral arteries have no external elastic lamina, the precise boundary between the media and adventitia was not known. Therefore, the medial and adventitial images used for quantification were selected from the z-stack based on morphological features, roughly 40% and 80% of the

way through the wall (values consistent with previously reported wall thicknesses of cerebral arteries [74]). Collagen damage was quantified by calculating the percentage of pixels having an intensity above a specified threshold. This threshold was defined to be 2.0 times the average brightness of a slice within the corresponding control sample taken at the same wall depth (12-bit scale). The threshold was applied to minimize contributions from background signal inherent to CHP binding of remodeling collagen. Other thresholds (1.5 and 2.5) were qualitatively evaluated; however, these were not ultimately utilized as they appeared to increase false classification of damaged and remodeling fibers. The effect that varying this threshold has on the study results is addressed in Appendix B.

Digital masks were applied to the images to eliminate contributions from branches and associated sutures, as well as from tissue in contact with the needles during distension. Regions of enhanced signal near failed ends were also masked out as the motivation behind the study was to characterize collagen damage within regions of intact (subfailure) arterial tissue. Furthermore, in cases where tears occurred between the needles (n=2), the staining associated with the tear was also masked out. In a few of the circumferentially distended rings (n=3), tears between the needles were so significant that the samples were excluded from the analysis, as all staining was associated with the torn tissue.

4.3.7 Quantification of damaged fiber orientation

OrientationJ, an ImageJ plug-in, was used to quantify the orientation of the damaged collagen fibers. Described in detail by Rezakhaniha et al. [102], this image

analysis tool evaluates the local orientation and isotropic properties of every pixel in an image by analyzing pixel gradients in both the vertical and horizontal directions. While pixel orientation is the primary output of the plug-in, coherency and energy are additional measures of how aligned the structures are. Coherency is bounded between 0 and 1, with 1 indicating highly oriented structures and 0 indicating isotropic areas. The reader is referred to [102] for further details on these parameters.

Prior to processing, pixels having an intensity lower than the control-specific threshold were set to zero. The built-in function 'Dominant Direction' was used to quantify the dominant orientation of the damaged fibers. The 'Distribution' function was used to provide a hue-saturation-brightness (HSB) color-coded map and histogram of fiber orientations for each image. In order to discriminate between significantly and not-significantly oriented areas, the minimum normalized energy was set to 2%. Finally, a cubic B-spline interpolation was used with a Gaussian window of one pixel.

4.3.8 Regression analysis

Collagen damage versus tissue stretch data were fit with a piecewise linear regression model to estimate the average stretch at which the onset of damage occurred. Using a method similar to that employed by Provenzano et al. [42], the percentage of collagen damage (D) was modeled as a function of stretch (λ) as

$$D = m(\lambda - \lambda_C)I[\lambda] \tag{4.6}$$

with

$$I[\lambda] = 0 \text{ for } \lambda < \lambda_C$$

$$I[\lambda] = 1 \text{ for } \lambda \geq \lambda_C$$

where λ_C is the critical stretch threshold below which collagen damage is zero and above

which damage increases linearly with stretch according to slope m. The indicator function $I[\lambda]$ equals 0 when $\lambda < \lambda_C$ and equals 1 otherwise – defining the onset of damage at λ_C. The piecewise model was fit to the experimental data with a Levenberg-Marquardt algorithm using MATLAB's 'lsqcurvefit' function having tolerances set to 1e-8.

4.3.9 Statistical methods

Confidence intervals were calculated for the linear regression model according to standard approaches outlined by Navidi [103] and using the 'regstats' function in MATLAB. Representing our linear estimate of collagen damage vs. stretch (y vs. x) with the form $\hat{y} = \hat{\beta}_0 + \hat{\beta}_1 x$, the 95% confidence intervals were given by Equation 4.7:

$$\hat{\beta}_0 + \hat{\beta}_1 x \pm t_{n-2,\alpha/2} * s \sqrt{\frac{1}{n} + \frac{(x - \bar{x})^2}{\sum_{i=1}^{n}(x_i - \bar{x})^2}} \tag{4.7}$$

where t is the t-statistic with $\alpha = 0.05$, n is the number of samples, s is the standard error, and the superscript bar denotes a mean value.

4.3.10 Quantification of the maximum stiffness and yield point

In order to correlate collagen damage with changes in tissue-level mechanical properties, the yield point and point of maximum stiffness were calculated for each sample. The First Piola-Kirchhoff stresses were calculated according to Equations 4.8 and 4.9:

$$P_Z = \frac{F_Z}{A} \tag{4.8}$$

$$P_\theta = \frac{F_\theta}{2WH} \tag{4.9}$$

and plotted against stretch. As done previously [57, 68, 69, 100, 104], baseline load cell noise was reduced using the digital filter specified in SAE J211 [105] and filtered traces were compared to original data to ensure fidelity. The stiffness at each data point of the loading curve was calculated as the slope of a regression line centered over 1% strain (25 data points for circumferential samples, 48 data points for axial samples). The yield point was defined as the earliest point in the loading curve where the stiffness dropped below 73.4% of the greatest stiffness achieved prior to that point. This threshold was determined in a previous study from the average noise amplitude in stiffness plots of juvenile sheep MCAs [104]. The maximum stiffness was then calculated as the greatest slope prior to the yield point. This sequence was important as in a few samples, stiffnesses higher than that observed in the linear region occurred beyond what we deemed as obvious yielding (see for example Figure A.1, bottom right graph, middle trace). Only stiffnesses beyond λ_θ = 1.1 and λ_Z = 1.2 were evaluated, as data below these levels occasionally showed significant changes in slope prior to the primary linear region (possibly attributable to fiber reorientation). Furthermore, care was taken to rule out slope decreases at the end of a subfailure loading which coincided with deceleration of the linear actuator.

4.4 Results

4.4.1 Location of molecular-level damage within the arterial wall

Confocal microscopy revealed the presence of unfolded collagen strands in overstretched arteries as manifest by the heightened CHP signal (circumferential loading, Figure 4.3, and axial loading, Figure 4.4). Interestingly, we found that circumferential

loading primarily damages collagen molecules within the media (Figure 4.3b) while axial loading primarily disrupts collagen within the adventitia (Figure 4.4c). While some CHP signal was observed in the other layers (Figures 4.3c and 4.4b), it was predominantly an artifact from strong fluorescence in a neighboring layer. In general, CHP staining was found to be spatially inhomogeneous with concentrated regions of fluorescence indicating focal collagen damage. Furthermore, adventitial damage patterns (Figure 4.4c) typically appeared more fibrous than medial ones (Figure 4.3b). As expected, minimal signal was observed in the controls (Figure 4.3d-f and Figure 4.4d-f) as these were not overstretched.

4.4.2 Orientation of damaged fibers

The orientations of the damaged fibers revealed via CHP staining (and measured in their unloaded state) aligned greatly with the direction of loading (Figure 4.5). Considering only samples having a greater percent damage than control samples, the fiber orientation following circumferential loading was -3.1 ± 6.0 degrees (relative to circumferential axis) with a coherency of 0.27 ± 0.06 (mean ± SD, n=16). Following axial loading, the damaged fiber orientation was 86.9 ± 9.6 degrees with a coherency of 0.20 ± 0.05 (n=8). All orientation and coherency values used in this analysis are compiled in Appendix A.

4.4.3 Correlation between CHP intensity and mechanical overload

We also found that the CHP signal increased with overstretch severity for both loading directions. This was true both qualitatively (Figure 4.6) and quantitatively (Figure 4.7). Collagen damage was quantified for a single layer within the wall, the

media for circumferentially loaded samples and the adventitia for axially loaded samples. The CHP signal following relatively mild stretches (Figures 4.6b and 4.6f) was comparable to that of controls (Figures 4.6a and 4.6e), then increased approximately linearly beyond a critical stretch threshold, λ_C (Figure 4.7). Note that controls were overstretched slightly beyond their *in vivo* configuration during preconditioning: approximately 5% in the axial direction when determining the *in vivo* length and roughly 1% in the circumferential direction as pressures were cycled up to 150 mmHg, but 100 mmHg was deemed the *in vivo* pressure. As the amount of 'damage' was also quantified in controls, data from them are included in Figure 4.7 near the origin.

In order to better define the thresholds and accumulation of collagen damage, the data were fit with a piecewise linear regression model. Regression lines consisted of an initial horizontal line through the origin followed by a second line having a constant positive slope. The intersection of these two lines (λ_C) is indicative of the collagen damage threshold, while the slope (m) of the second line is indicative of the rate of damage accumulation with strain beyond λ_C. The resulting regression lines and 95% confidence intervals are overlaid on the data (Figure 4.7) with output parameters presented in Table 4.1. Calculated values for λ_C appear appropriate given that relatively minimal CHP signal was detected below either threshold. In a few samples, small amounts of collagen damage could be observed following milder stretches (see thin fibers in the center of Figure 4.6f); however, our algorithm could not distinguish these from the background signal inherent to controls. More sophisticated edge detection algorithms were also implemented; however, these did not improve sensitivity without reducing specificity.

4.4.4 Relationship between collagen molecular damage and tissue yielding

Analysis of the stress-stretch data revealed that the stretch thresholds (λ_C) as determined by CHP staining approximately coincided with the arterial yield stretches (Table 4.1). For both loading directions, λ_C (red dashed lines in Figure 4.7) fell within 3% strain of the average yield point (solid blue circles in Figure 4.7). As our measure of yielding is somewhat subjective, it is also instructive to compare the stretch threshold relative to the average point of maximum stiffnesses (solid blue squares in Figure 4.7), a measure that some use to define yielding. For the case of circumferential loading, the threshold of collagen damage, λ_C, fell midway between the average stretch at maximum stiffness and the average yield stretch. In contrast, the collagen damage threshold in axial loading fell slightly above the yield stretch. A discussion on the strength of this finding is addressed in Section 4.5.3. Also, a complete list of circumferential (n=11) and axial (n=10) yield stretches is included in Appendix A.

4.5 Discussion

Using CHP, we detected and characterized molecular-level unfolding of collagen in cerebral arteries subjected to a single overstretch. These findings are the first to identify any stretch-induced molecular disruption to collagen in blood vessels, as previous investigations have only explored tissue-, fiber-, or fibril-level disruption. In addition to detecting damage, CHP effectively localized the damage, both revealing the specific layer within which damage occurred and demonstrating that overstretch primarily disrupted fibers aligned with the direction of loading. Finally, comparison of CHP

staining with mechanical data showed that arterial yielding was closely associated with the onset of collagen damage, and that, beyond this threshold, collagen damage increased with strain. Each of these findings held true for both axial and circumferential modes of overload. These results suggest that collagen unfolding is likely to occur in trauma and in surgical interventions such as angioplasty, making CHP a potential tool for better understanding vessel damage in clinical settings. Findings also lend insight into the role of molecular-level collagen damage in arterial softening. Observations of elastin damage were also noted; however, these will be addressed in a future work.

4.5.1 Location and orientation of damaged collagen within the wall

The finding that overstretch primarily damages arterial collagen that is aligned with the direction of loading, with negligible damage to off-axis fibers, is both novel and consistent with the current knowledge of arterial mechanics. While fiber angles were measured in an unloaded state, relatively small changes occur when transforming between this and the *in vivo* state (Appendix C). It is well established that collagen is the primary load bearing constituent in arteries at high levels of strain [106]. Given that collagen fibers are much stiffer in tension than in shear [107], it follows that the fibers bearing the greatest load will be those aligned with the loading direction. This, coupled with the fact that axially oriented fibers are primarily found in the adventitia [42, 74, 102, 104, 106-108], is consistent with our finding of an axially oriented CHP signal within the adventitia following axial overstretch. The fact that the arterial media is rich with circumferentially oriented fibers [106] is similarly consistent with our finding of a circumferentially oriented CHP signal within the media following circumferential

overstretch. Furthermore, we report that damaged circumferential fibers are more aligned than the damaged axial fibers (SD=6.0 compared to 9.6 degrees), paralleling the structure of intact collagen in cerebral arteries [108]. The z-resolution of the confocal objective used was not fine enough to precisely quantify collagen damage among fibers oriented orthogonal to the loading direction, as these images were often influenced by the strong fluorescence from a neighboring layer. Therefore, we cannot conclusively exclude medial damage following axial loading or adventitial damage following circumferential loading, though the level of collagen damage in these layers is clearly lower. Helical fibers known to be present in the adventitia (Figure 4.7a in [74]), were intact and often observed while imaging and quantifying the adventitia for the axial study (see large diagonal fiber with moderate brightness in Figure 4.6g). While such fibers are hypothesized to provide a protective mechanism against overdistension, it is interesting that these were never observed to have much, if any CHP staining. It is possible that such fibers did support axial loading while others more aligned with the loading reached their failure point earlier, leading to crack initiation and propagation across the remaining tissue and subjecting helical fibers to a quicker loading to failure. Preliminary work suggests that the duration of the strain, not just the magnitude, increases the amount of mechanically-induced unfolding.

Despite the correlation between our results and the current knowledge of arterial mechanics, the actual identification of mechanically damaged collagen has only been reported by a handful of investigators, each using either histology [50] or electron microscopy [87-89]. In agreement with the present work, one report showed that circumferential loading with a balloon catheter damaged circumferentially oriented

medial fibers. However, the presence/absence of damage within the adventitia was not reported [89].

4.5.2 Thresholds and accumulation of collagen damage

To our knowledge, this is the first study to define clear thresholds of collagen damage in blood vessels and to characterize the accumulation of damage with strain. While both parameters serve as meaningful inputs for future microstructurally-based constitutive models of arterial damage, neither one appears to have been previously defined for molecular-, fibril-, nor even fibril-level collagen disruption. The work that most closely achieves this for axial loading found the threshold for macroscopic collagen disruption to be between 6-30% beyond the zero strain length [50]. While this range is insightful, it is poorly defined and is limited to the case of 1000 loading cycles in rabbit aorta. For the case of circumferential loading, investigators have reported stretched collagen fibers in human MCAs after subjecting them to 1.5 atm and ruptured fibers after 3.0 atm [89]. However, these two data points fall short of defining a clear threshold or a rate of damage accumulation.

4.5.3 Coincidence of molecular damage and yielding

Aside from the novelty of detecting molecular-level collagen damage in vascular tissue, perhaps our most significant finding is the approximate coincidence of the yield point and the onset of CHP binding. To the best of our knowledge, no investigations have even compared thresholds of tissue-level yielding with any form of collagen damage in arteries. We hesitate to overstate our finding, though, as our methods for quantifying both

yielding and collagen damage could not be purely objective. We did, however, do our best to seek objectivity in all of our methods (see Appendix B for a discussion on quantifying collagen damage). Regarding yielding, there is no standard approach for quantifying the yield point in soft biological tissues; however, two general methods seem to be used. One method defines the yield point as the point of greatest stiffness either directly from the data [23, 109] or after fitting the data with a polynomial [110-112]. A second method defines the yield point as the point where the stress-strain curve first departs from the linear region based on a user-defined threshold [104, 113, 114]. While this latter approach is more sensitive to user inputs, it is better suited to detect yielding at the end of a sustained linear region rather than in the middle of it, which was our goal. We ultimately employed both methods, with the latter defining the yield point and the former defining the point of maximum stiffness. These two numbers provide some sense of the amount of variability in our calculated yield point. For both loading directions, we found the average difference between the yield point and the point of maximum stiffness to be 5% strain (Table 4.1). In defining the threshold for yielding, we did our best to be objective by taking the threshold from a previous study in similar tissue [104]. Furthermore, posthoc qualitative analysis showed that this threshold did a reasonable job of identifying the end of the linear region in all axial samples (Figure A.1). However, samples loaded circumferentially often exhibited a less pronounced linear region and less dramatic changes in stiffness, making it harder to qualitatively verify the identified yield points. In light of this, it is interesting to note that we found the axial threshold of collagen damage to best align with our defined yield point while the onset of collagen damage in circumferential samples (where the yield point was less defined) fell closer to

the point of maximum stiffness. The fact that changes in stiffness were more dramatic in axial loading may be due to the fact that the adventitia consists of thicker bundles of collagen fibers [38] compared to the media, which, upon rupture, cause more significant changes in stiffness.

4.5.4 Comparisons between circumferential and axial results

While the primary objective of the present work was to detect the presence of unfolded collagen following circumferential and axial loading separately, we believe there is still value in comparing the qualitative and even quantitative findings from the two datasets. In general, the CHP signal in the media following circumferential loading highlighted finer, more closely packed fibrous damage than that observed in the adventitia following axial tests (demonstrated in both Figures 4.5 and 4.6). This is likely due to the fact that smaller fibers are found in the media while the adventitia consists primarily of thick bundles of collagen fibers [38] having a larger spatial distribution [108]. These large adventitial bundles may explain the brighter CHP signal in axial tests (Figures 4.5 and 4.6), as larger damaged fibers would provide more binding sites for CHP. This brighter adventitial signal may also have contributed to the higher rate of damage accumulation beyond λ_C in axial tests (Table 4.1), since this would increase the likelihood of damaged fibers being above the defined pixel intensity threshold. Finally, the stretch threshold, λ_C, and related yield threshold, λ_Y, were found to be lower in circumferential tests (Figure 4.7 and Table 4.1). This may be due to fact that medial fibers are more aligned with the circumferential direction than are adventitial fibers with the axial direction [108], causing them to become taut and subsequently fail at lower

stretches. Additional factors such as collagen crimp and cross-linking may also contribute to differences in these damage parameters. However, to our knowledge, these have not been quantified in cerebral arteries. It should also be noted that there was an age difference in axial (juvenile, approx. 3-9 months) and circumferential (adult, approx. 3-7 years) samples. While microstructure is expected to change with age, our recent study on supraphysiological axial loading of sheep MCAs found no significant differences in the maximum stiffness, the ultimate stretch, or in the ultimate stress between the juvenile and adult groups [100]. As collagen dominates the passive mechanical response at high strains, these results suggest negligible changes in collagen over these same age ranges. In contrast, biaxial tests in the physiological range from the same study found the circumferential stiffness to be roughly five times higher than the axial stiffness for juvenile and adult samples, paralleling the difference in supraphysiological stiffnesses observed in the present work (Figure 4.7). While these observations are not conclusive, they suggest that effects from structural differences in the two age groups are likely secondary to the inherent structural differences between the two loading directions.

Though not directly related to collagen damage, we also noted differences in the stress-stretch behavior for the two loading directions. As the curves shown begin from the *in vivo* configuration (Figure 4.7), they include a slight initial stress offset, are missing much of the toe-region and are, therefore, more linear than those commonly presented for blood vessels. However, we have provided more complete axial loading curves for this same tissue previously [100]. Furthermore, the average axial and circumferential *in vivo* stretches presented in the same work can be used to convert the stretches reported here to be relative to the unloaded length. The stress offset in the axial samples is lower than

expected, likely due to some stress relaxation when determining the *in vivo* length (Section 4.3.1). In addition, the stress-stretch response over the loading range was generally stiffer in the circumferential direction than the axial, bearing roughly four times the stress at half the stretch. A similar disparity was also observed at the *in vivo* stretch, in agreement with our previous investigation in sheep [100] yet contradictory to our studies in human [68] and rat [69] cerebral arteries. Further investigation is needed to determine whether these discrepancies are simply due to test methodology or actual species-specific differences.

4.5.5 Comparisons with CHP results in rat tail tendon fascicle

As mentioned earlier, successful preliminary results of CHP binding in mechanically overstretched arteries led to a parallel study in rat tail tendon fascicles [92]. Three similarities can be drawn between the recent findings from that study and the present work. First, the study in tendon showed a nearly linear increase in CHP binding with strain beyond a critical threshold, comparable to that reported here in arteries (Figure 2 of [92]). Second, the onset of CHP binding in tendon also coincided with a decrease in stiffness (Figure 2a and Supplementary Figure 2a of [92]). Although a precise yield point was not defined in the tendon study, it was qualitatively observed for all samples tested. Finally, the authors noted that CHP did not bind to ends of tissue that were cut with scissors, suggesting that such loading does not unfold collagen strands. We, too, observed this phenomenon in arteries. One key mechanical difference between the two tissues, however, was that both molecular- and tissue-level failure occurred at lower stretches in the tendon fascicle than in arterial samples. This is expected as arteries, in

general, have a much higher fraction of elastin [115].

Two technical differences between the two studies are also apparent. First, multiple test groups in the tendon study, each having a specific target stretch, define the increase in CHP staining beyond the critical strain threshold (Figure 2 of [92]). This was not possible to achieve in the present work as our linear trends were primarily defined by samples pulled to failure (Figure 4.7 and Appendix A), with each having unpredictable failure stretches. Therefore, we characterized the rise in CHP staining with a regression line and associated confidence intervals rather than with error bars for each strain group. A second difference between the two studies is the additional noise observed in the arterial damage-stretch plots (Figure 4.7). This is likely due to both the structural heterogeneity of arteries as well as the increased CHP signal observed in arterial controls (for example, see Figure 4.6e). This latter factor led us to develop a more sophisticated algorithm for classifying collagen damage in arteries – defining pixels with intensities greater than two times the average control intensity as being mechanically damaged. It is still unclear why arteries were more prone to background binding compared to rat tail tendons; however, one possible explanation would be a higher native collagen-remodeling rate in arteries.

4.5.6 Advantages of CHP over existing technology

The reported binding of CHP to mechanically damaged collagen in arteries is a novel discovery for the field of arterial mechanics. This technique improves upon existing methods in four important ways. First, CHP opens the door to understanding molecular-level damage to collagen whereas other common techniques (SEM, TEM, and

histology) only reveal fibril-, fiber-, or tissue-level disruption. Therefore, CHP can be used to further elucidate the progression of collagen damage across these physical scales. Furthermore, the previously mentioned study in rat tail tendon fascicles suggests that collagen triple helices may unfold long before disruption or damage of larger scale structures – making CHP a more sensitive metric of collagen damage [92]. In addition, CHP lends insights into inter- and intramolecular damage progression. For example, the fact that CHP bound along the length of damaged fibers in the present work suggests that the stress/strain mechanisms leading to molecular failure (likely alpha-chain pullout, [92]) are not localized to a single point on a fiber, but that they propagate along the length of a fiber during the overload. Second, CHP conjugated to a fluorophore provides an approach for detecting vascular damage that is nondestructive in both its imaging of subsurface detail and minimal tissue preparation. In contrast, electron microscopy and histology require serial slicing in order to reveal subsurface damage. Furthermore, previously mentioned studies using an SEM [89] required fixation, formic acid digestion in a 45 °C oven, and freeze drying – all of which can alter the very structures being studied. Third, the damage-specific CHP provides a straight-forward method for positive identification of damage in tissue compared to a ‘needle-in-the-haystack’ hunt with an SEM. Fourth, in contrast to classifying the severity of tissue damage with the help of a blinded observer [50], quantifying the fluorescence intensity of CHP provides a simple, objective measure of damage severity.

4.5.7 CHP as a tool for probing vascular damage in angioplasty and trauma

In light of the advantages that CHP offers over existing techniques, this marker has the potential to serve as a useful probe of vessel injury in both angioplasty and trauma. While molecular-level collagen damage has yet to be demonstrated in either of these settings, we have reason to believe it occurs. For example, balloon angioplasty has been shown to rupture collagen fibers [89]. Given our recent evidence that collagen unfolding precedes fiber failure [92] it is likely that collagen unfolding occurs in balloon angioplasty. Therefore, CHP could serve as a useful research tool for assessing the severity of balloon or stent loading acutely as well as tracking collagen remodeling over time. More specifically, CHP could be used to answer Humphrey's call for "multiaxial data from which balloon-induced wall damage can be quantified as a function of clinically relevant balloon parameters" [116]. Furthermore, as we have shown collagen unfolding to be correlated with tissue yielding, this molecular-level denaturation may be the key mechanism behind the well-established remnant deformations observed in angioplasty [82, 117]. Regarding trauma, it is well known that blood vessels are often torn and bleed as an immediate consequence of TBI [2, 3]. It follows that other vessels undergo subfailure deformations. Therefore, CHP could also serve to increase understanding of vascular strains in TBI by probing for intact yet damaged vessels, potentially elucidating their prevalence, loading magnitude, and even their loading direction. However, as the present work only explored quasi-static loading, the effect of strain rate on CHP binding should first be understood *in vitro*.

Should an investigation require detection of mild collagen damage, efforts should

first be made to improve the signal-to-noise ratio of CHP binding in arteries. This could be accomplished by reducing or blocking the background signal inherent to continuously remodeling collagen in arteries with unlabeled CHPs prior to overstretch. Alternatively, development of a more sophisticated algorithm that distinguishes between CHP binding of remodeling and damaged fibers could also facilitate detection of mild damage.

4.5.8 Role of collagen unfolding in arterial softening

As arterial mechanics are known to soften in angioplasty [59-61] and theorized to do so in trauma [57], another motivation behind this investigation was to shed light on the microstructural mechanisms responsible for arterial softening. Numerous experimental and computational studies have demonstrated that a single overstretch softens the subsequent reloading curve in cases of both axial [57-60] and circumferential [59-61, 85] loading. While this softening behavior has been attributed to collagen [62, 118], the underlying mechanism is not known. Using the same tissue and experimental approach as done here, Bell et al. showed that softening occurs following axial stretches as low as 1.2 times the *in vivo* length [57] – lower than the threshold for collagen damage observed in the present study. This comparison suggests that mechanisms other than the unfolding of the collagen triple helix must be at play in arterial softening. While this is likely true, we hesitate to rule out the present mechanism, as small amounts of CHP staining were observed in samples stretched to 1.2 (Figure 4.6f), although these subtle signals were difficult to quantitatively distinguish from background signals.

The literature on preconditioning provides additional mechanistic insights for arterial softening, as the softening during preconditioning is similar to that observed by

Bell et al. Quinn and Winkelstein showed collagen fiber reorientation to be correlated with softening during preconditioning of ligaments [119]. Others have suggested that macromolecule unfolding [38], as well as irreversible proteoglycan deformation [120], could also play an important role in preconditioning. Therefore, these alternative mechanisms may be important following mild overstretch of arteries.

4.5.9 Limitations

Two limitations of this study are noted. First, despite the application of microspheres on all overstretched samples, the stretches reported in the present work were calculated from a more global measure of needle displacements. While local strain measurements do result in different damage parameters, additional analysis suggests that this factor doesn't undermine the association between tissue yielding and the onset of collagen damage (Appendix D). Second, the method used for axial loading was biaxial (due to the internal fluid pressure) rather than uniaxial (as done for circumferential loading). This was done out of an initial desire to improve translation of findings to an *in vivo* setting. While this does limit comparisons between the two modes of loading, the contribution of circumferential stress during axial loading was rather small, approximately 7% of the axial stress at the onset of collagen damage. Therefore, we would not expect the axial results to be much different had they been conducted in a purely uniaxial manner.

4.6 Conclusion

For the first time, molecular-level collagen damage was detected, localized, and quantified in overstretched vascular tissue through the use of a collagen hybridizing peptide (CHP). Consistent with established literature on arterial mechanics [42, 74, 102]; [104, 106-108], we showed that overstretch primarily damages (unfolds) collagen fibers that are aligned with the direction of loading. Furthermore, we demonstrated that the onset of collagen damage is closely associated with tissue-level yielding. This was true for both axial and circumferential loading. As samples were only loaded quasi-statically, it remains unknown how results may vary at higher strain rates. Not only does this approach provide the first insights into molecular-level collagen damage in vascular tissue, but it improves upon existing methods of detecting collagen damage as it is nondestructive, readily visualized, and objectively quantified. We anticipate that this approach can be used to better understand arterial damage in clinically relevant settings such as angioplasty and vascular trauma. Furthermore, CHP can be a tool for the development of microstructurally-based constitutive models and experimentally validated computational models of arterial damage and damage propagation across physical scales.

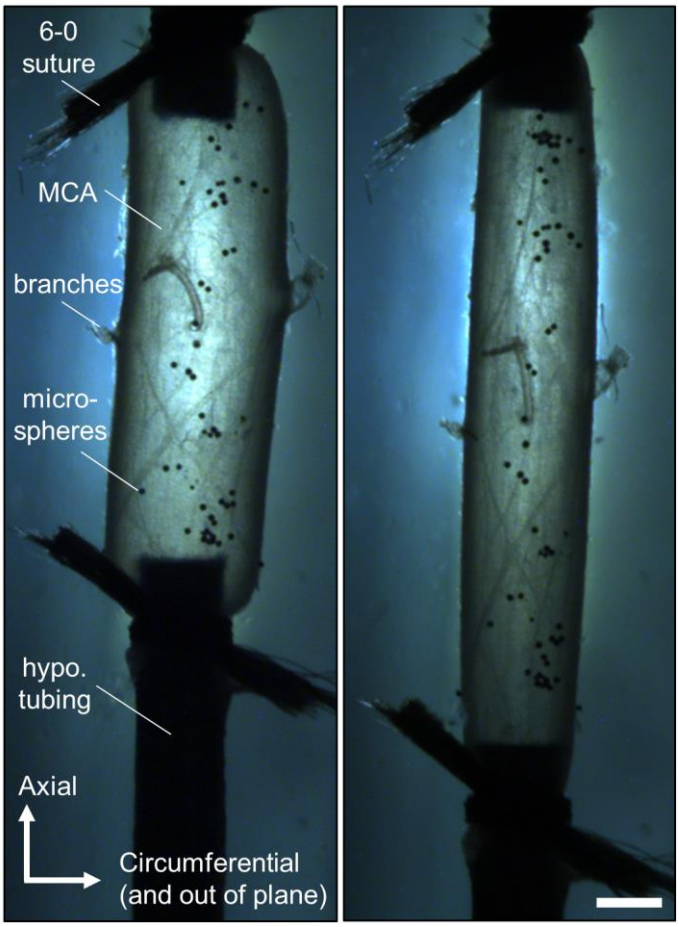

Figure 4.1: Artery configuration for axial overstretch. Light microscope image of a single sheep MCA mounted to notched hypodermic tubing just prior to (left) and at peak (right) overstretch. Small branches were ligated so that the vessel could maintain 100 mmHg (13.3 kPa) during overstretch. Small black dots are microspheres used to track local strain. Axes and scale bar (0.5 mm) apply to both images.

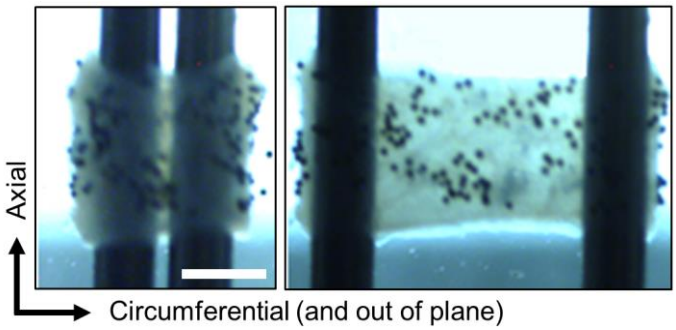

Figure 4.2: Artery configuration for circumferential overstretch. Light microscope image of a single arterial ring from a sheep MCA just prior to (left) and at peak (right) overstretch. These rings, or short lengths of otherwise intact artery, came from longer MCA segments that were first mounted and preconditioned similar to segments loaded axially (Figure 4.1). However, following preconditioning, segments were chopped into short lengths so that the two 28 gauge hypodermic needles shown could be passed through the lumen. Small black dots are microspheres used to track local strain. Axes and scale bar (0.5 mm) apply to both images.

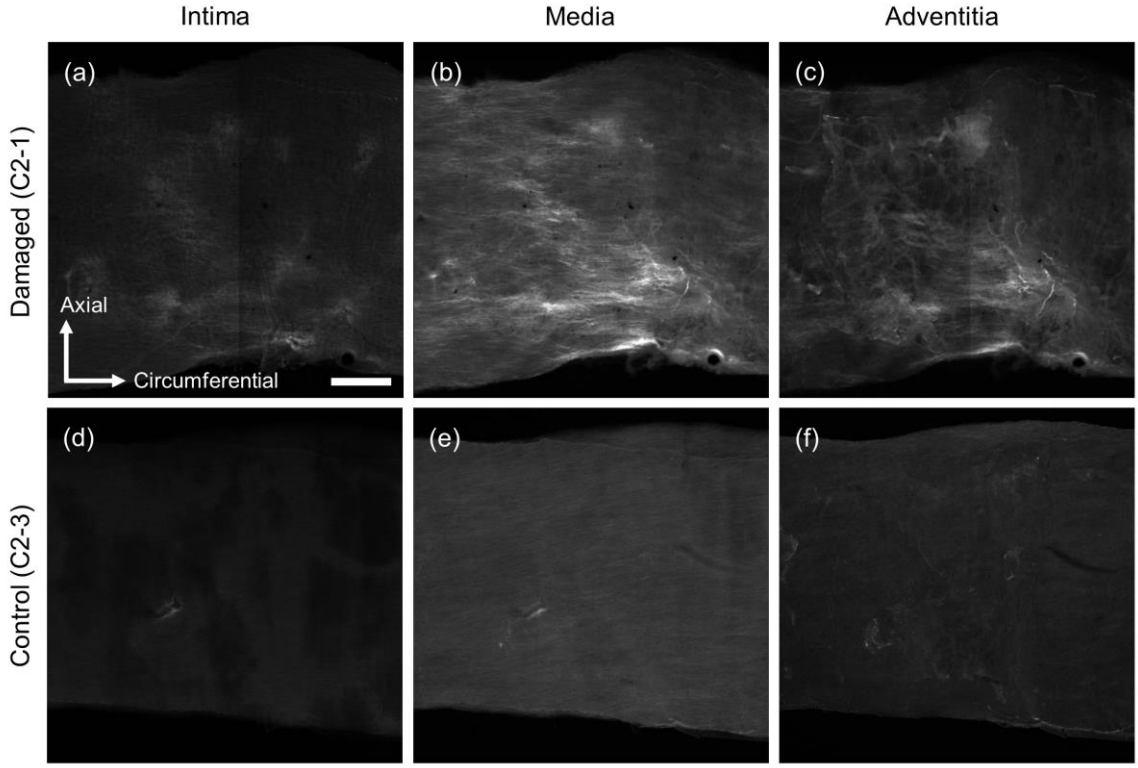

Figure 4.3: Confocal images from an artery loaded circumferentially relative to its control. The fluorescent CHP signal was most prominent in the media (b), indicating that that layer had the highest concentration of unfolded collagen molecules. Fluorescence in the intima and adventitia (a, c) is primarily an artifact from the medial signal (b). Axes and scale bar (200 μm) apply to all images.

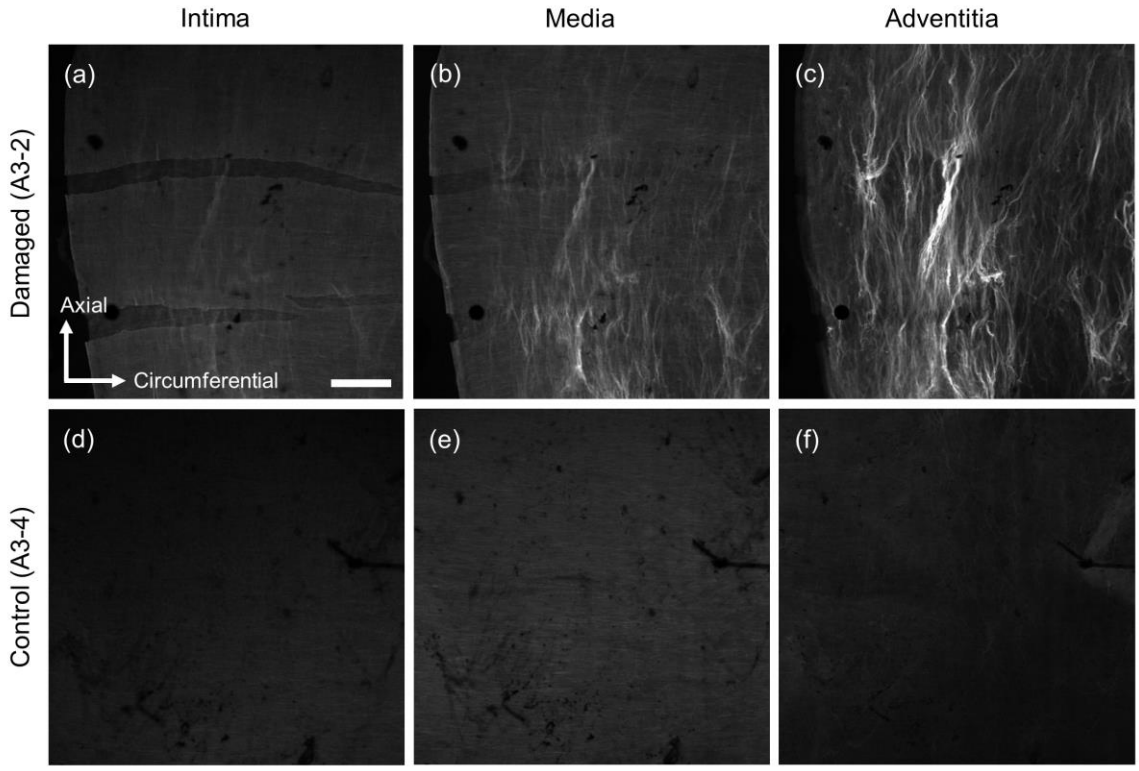

Figure 4.4: Confocal images from an artery loaded axially relative to its control. The fluorescent CHP signal for axially loaded samples was most prominent in the adventitia (c). The two horizontal bands in (a) show rupture of the internal elastic lamina. Fibrous fluorescence in intima and media (a, b) is primarily an artifact from the adventitial signal (c). Axes and scale bar (200 μm) apply to all images.

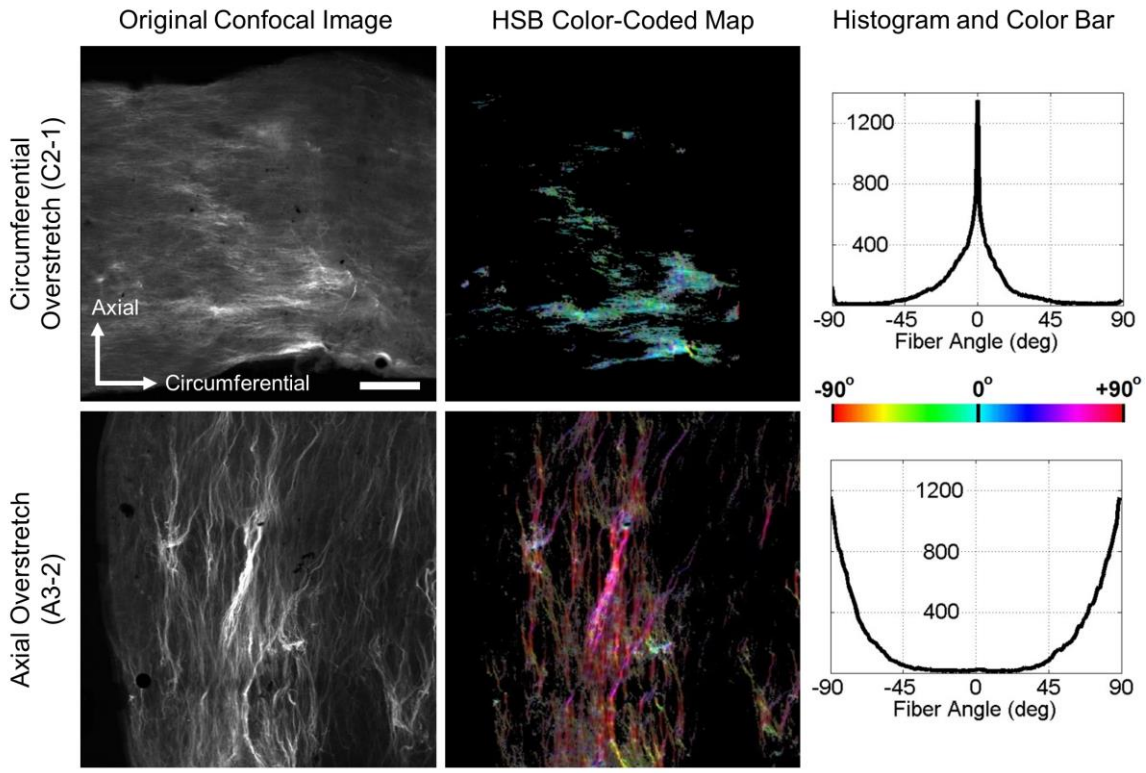

Figure 4.5: Representative micrographs showing the orientation of damaged collagen fibers. The damaged fibers primarily exhibit a circumferential orientation (0 degrees) within the circumferentially loaded samples while samples loaded axially show damaged fibers mainly with an axial orientation (±90 degrees). After setting all pixels below the control-specific intensity threshold to zero, OrientationJ was used to quantify the orientation of each pixel within the image, outputting an HSB color-coded map and an associated histogram (Hue: local orientation; Saturation: coherency; Brightness: original image). Histograms count the total number of pixels with a defined orientation (one degree resolution). Axes and scale bar (200 μm) apply to all images.

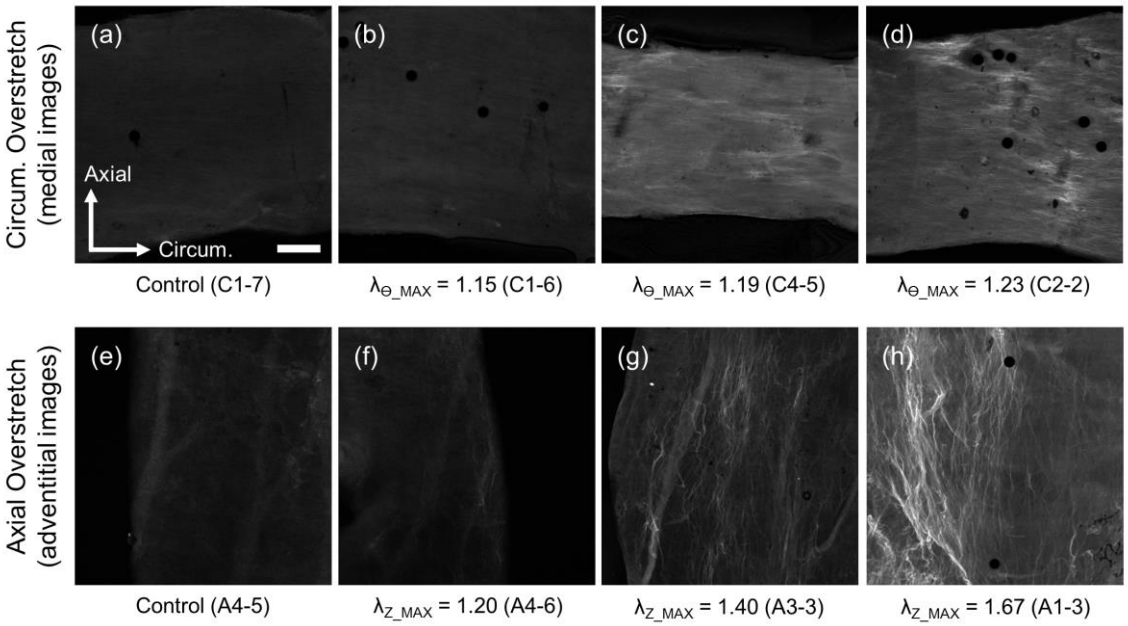

Figure 4.6: Increase in CHP binding (collagen damage) with overstretch severity. Samples subjected to relatively mild levels of overstretch (b, f) appeared similar to mechanical controls (a, e); however, the increase in CHP binding became more apparent at higher strains (c, d, g, h). Images only show a portion of the entire sample. Black circular dots are microspheres. Axes and scale bar (200 μm) apply to all images. Note that samples serving as mechanical controls were slightly overstretched beyond their *in vivo* configuration during preconditioning: (a) $\lambda_{\Theta\_MAX} = 1.01$ and (e) $\lambda_{Z\_MAX} = 1.05$ as described in Section 4.3).

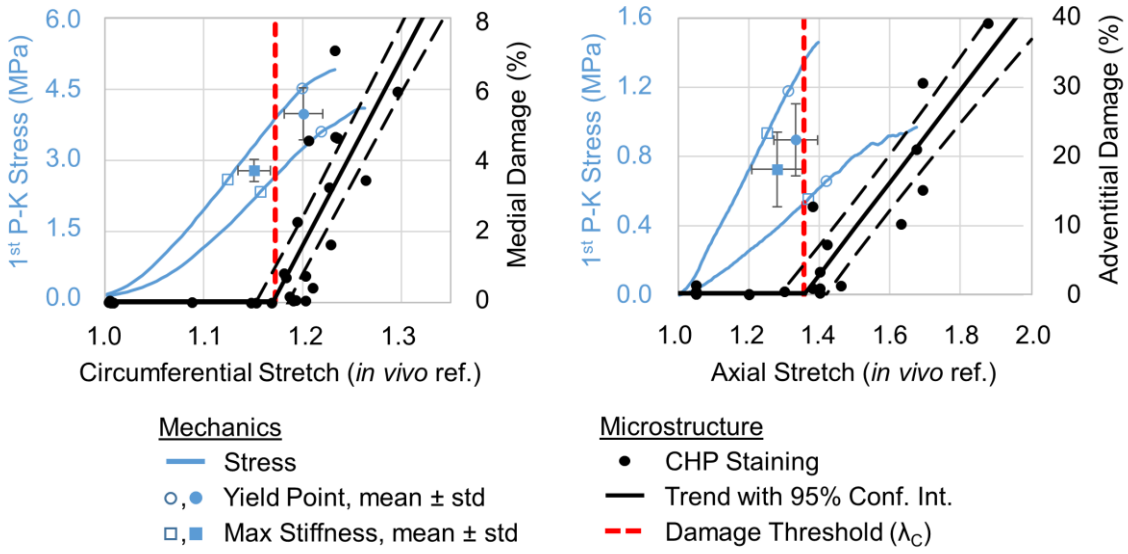

Figure 4.7: Collagen damage and arterial stress vs. overstretch. Collagen damage was measured following CHP staining as the percentage of pixels above a control-specific intensity threshold. Both directions of loading produced an increase in damage with overstretch severity. The intersection of the horizontal and sloped regression lines defines the critical threshold for collagen damage (λ_C, red dashed line). In both cases, this damage threshold fell with 3% strain of the average yield point (solid blue circle). Two representative stress-stretch curves are overlaid for each loading case. Stretches are measured relative to the *in vivo* configuration.

Table 4.1. Collagen damage parameters (calculated from linear regression of CHP data) compared to stretches at maximum stiffness and yield stretches (calculated from stress-stretch curves).

Loading Direction	Stretch at Max Stiffness, λ_{MAX} (mean ± SD)	Yield Stretch, λ_Y (mean ± SD)	Collagen Damage Parameters		
			Damage Threshold, λ_C (95% CI)	% Damage Per Unit Stretch (m) beyond λ_C	R^2
Circumferential	1.15 ± 0.01	1.20 ± 0.01	1.17 (1.15-1.19)	52.8	0.55
Axial	1.28 ± 0.07	1.33 ± 0.06	1.35 (1.29-1.42)	66.7	0.79

CHAPTER 5

STRETCH-INDUCED INTIMAL FAILURE IN CEREBRAL ARTERIES

5.1 Abstract

Recent clinical studies have shown that TBI is a significant risk factor for stroke. Motivated to better understand possible mechanisms of this association, we studied subfailure disruption of the intima in overstretched sheep cerebral arteries as this has been implicated in the increased risk of stroke following blunt cerebrovascular injury. Middle cerebral arteries from four age groups are stretched longitudinally to failure and intimal disruption is captured with a video camera. We found that all vessels experienced intimal disruption prior to catastrophic failure with nearly all samples incurring disruption well below the stretch at ultimate stress. The threshold of intimal failure was independent of age. Additional analysis showed that disruption included failure of both the endothelium and internal elastic lamina. These findings likely have important implications for vessel function following trauma. Future work should seek to identify subfailure disruption of the cerebrovasculature in models of head trauma.

5.2 Introduction

Traumatic brain injury (TBI) is one of the major health care problems in the United States, contributing to nearly a third (30.5%) of all injury-related deaths [1]. An

estimated 1.7 million people annually sustain a TBI, and of these patients, approximately 50,000 die [1]. Those who do survive the initial head injury often suffer from neurological damage. While damage to the brain tissue is the fundamental concern in TBI, nearly all significant head injuries include some element of injury to the blood vessels, and any injury or dysfunction of the vasculature puts neural tissue at risk.

Two recent clinical studies have shown that TBI is a significant risk factor for stroke, comparable in significance to hypertension [121, 122]. As intracranial hemorrhage is a regular part of the acute TBI picture, authors excluded such patients from their analysis. One author found a persisting higher risk of ischemic stroke 60 days after TBI [122]. Another found a greater risk of all types of stroke (ischemic and hemorrhagic) post-TBI that decreased with time after injury but that was still 2.3 times higher five years after TBI than in non-TBI patients [121].

Mechanisms behind the TBI-stroke link are unclear; however, one likely mechanism is subfailure damage to the vascular wall. The vascular wall is made up of three principal layers known as the intima, the media, and the adventitia. The intima is the innermost layer and forms the lumen. Its inner surface is lined with axially oriented endothelial cells which are directly in contact with flowing blood and an underlying thin (~80 nm) basal membrane [70]. Separating the intima and media is a fenestrated sheet of elastin known as the internal elastic lamina (IEL). Subfailure disruption of the intima has been implicated in the increased risk of ischemic stroke following blunt cerebrovascular injury (BCVI) [123, 124]. BCVI is a rare but serious consequence of blunt trauma to the head and neck. It often includes damage to vertebral and carotid arteries and is primarily caused by longitudinal stretching of the vessels [123].

We hypothesize that similar longitudinal stretching of intracranial vessels in TBI may also lead to intimal failure and partly explain the increased risk of stroke. However, in order to better understand this mechanism, the objective of the present work is to first quantify the occurrence and threshold of intimal failure in cerebral arteries. We do so by subjecting sheep middle cerebral arteries (MCAs) to a single axial overstretch to failure. Intimal failure is captured with a video camera and samples from four age groups are used to test for changes with development. Additional analysis is carried out on select samples to elucidate which components of the inner vessel wall are being damaged.

5.3 Methods

5.3.1 Specimen acquisition and preparation

Middle cerebral arteries (MCAs) were collected from sheep ranging in age from fetal to adult. A total of 41 specimens were tested: 10 from fetal lambs (128-135 days gestation; 85-90% full gestation), 11 from newborn lambs (8 days old after full term or 150 days gestation), 11 from juvenile lambs (3-7 months), and 9 from adult ewes (3-7 years). The mechanical failure response of these same vessels was reported previously [100]. All fetal, four juvenile, and all but one adult vessels were obtained from the Lamb Intensive Care Unit (LICU) at the University of Utah; the remaining vessels were collected from local slaughterhouses. Sheep from the lamb LICU were euthanized by injection of beuthanasia solution, while those from slaughterhouses were sacrificed by either electrical shock or percussion stunning. In the latter cases, the impact site was located away from the Circle of Willis to prevent damage to the MCAs prior to testing. Sheep MCAs were removed shortly after death and placed in cold, calcium-free

phosphate-buffered saline (PBS; KH_2PO_4 1.54, NaCl 155.2, $Na_2HPO_4–7H_2O$ 2.7; concentrations in mM). Vessel testing always occurred within 48 hrs of death. Procedures for obtaining MCAs were prospectively approved by the Institutional Animal Care and Use Committee at the University of Utah.

Following death, the sheep brain was removed and a proximal segment of the MCA (~ 8 mm long) was removed and placed in cold PBS. Remaining pia-arachnoid tissue was carefully peeled away from the MCA with forceps. Branches were ligated with unwound 6-0 silk sutures. Cross-sections were typically obtained from the proximal end of the dissected vessel and photographed for subsequent measurement.

5.3.2 Mechanical testing

Mechanical testing was performed with an apparatus and methods identical to those described previously [100]. Briefly, ends of isolated MCAs were cannulated with grooved, 22-gauge hypodermic needles using 6-0 silk suture and cyanoacrylate glue. Tests used a custom load frame which facilitated both circumferential and axial loading, while simultaneously recording vessel pressure and axial load. Specifically, one of the aforementioned hypodermic needles was attached to a load cell (Honeywell, Model 21 Low, 250 or 1000 g) through an X-Y stage that allowed for needle alignment. The second needle was attached to the load frame via a low friction sled supported by a voice coil actuator (Akribis, MGV52-25-1.0). Displacement of the actuator moved this second needle vertically along the sled track, axially stretching the vessel. Specimens were viewed via a digital video camera (Pixelink, PL-A641) attached to a stereo microscope (Zeiss, Stemi 2000-C). Vessels were bathed in calcium-free PBS to eliminate any active

contribution from smooth muscle cells and perfusion was digitally controlled by a linear actuator (Ultra Motion, D-A0.25-AB-HT17075-4-P). Internal pressure was determined by averaging the signals of pressure transducers (Honeywell, 26PCDFM6G) located at each end of the vessel. Test control, as well as data and video acquisition, was accomplished using a custom LabVIEW program (National Instruments). A light source was aimed at the vessel so that that intimal failure could be observed through the vessel wall and captured on video. Actuator positions were given by digital encoders (resolution 1.0 μm). Data from the encoders, load cell, and two pressure transducers were recorded at 100 Hz and images acquired at 3 Hz. Tests were performed at room temperature.

Mounted MCAs were preconditioned by oscillating the internal pressure ($50 < p_i < 150$ mmHg) for five cycles while length was held constant at up to 1.2 times the approximate reference unloaded length, L, defined subsequently by the point where force began to increase during an unpressurized axial stretch test. Following this, MCAs were subjected to a series of six biaxial sequences by cycling the pressure (up to 150 mmHg) with vessel length held constant (at 1.05, 1.07, or 1.10 times the *in vivo* length – defined below), and three axial stretch tests (up to 1.1 times the *in vivo* length) with constant pressures (50, 100, and 150 mmHg). These sequences were done in order to characterize the vessel mechanics around the physiological loading range for a concurrent study [100]. MCAs were finally stretched axially to failure under a constant internal pressure of 100 mmHg. All tests were done quasi-statically.

5.3.3 Data processing and analysis

Experimental data were processed to generate stress-stretch curves for the axial stretch to failure. MCAs were assumed to be incompressible, homogeneous, circular cylinders with uniform wall thickness. Unloaded reference outer diameter (D_o) and cross-sectional area (A) were obtained from images of vessel rings using Vision Assistant (National Instruments). Reference inner diameter (D_i) was calculated from these measurements. Current vessel length (l) was determined from actuator displacement, and current outer diameter (d_o) was measured from video images obtained during testing. The midwall circumferential stretch (λ_θ) and axial stretch (λ_Z) were calculated using Equation 5.1.

$$\lambda_Z = \left(\frac{l}{L}\right) \tag{5.1}$$

Current vessel inner diameter (d_i) was calculated using Equation 5.2, assuming incompressibility.

$$d_i = \sqrt{d_o^2 - \frac{4A}{\pi\lambda_Z}} \tag{5.2}$$

Enforcing equilibrium resulted in the mean axial Cauchy stresses (T_Z) in Equation 5.3, with F_Z being the experimental axial force.

$$T_Z = \frac{\lambda_Z}{A}\left(F_Z + \frac{\pi}{4}p_i d_i^2\right) \tag{5.3}$$

Force data were postfiltered with the Butterworth, 4-pole, phaseless filter specified in the SAE J211 standard, and diameters were interpolated between tests images to match corresponding force and pressure data. Axial *in vivo* stretch (λ_{IV}) was found during preconditioning and was defined as the axial stretch at which force did not change during

an increase in pressure up to 150 mmHg [100].

5.3.5 Luminal staining and confocal imaging

Additional analysis was carried out in order to determine which structures of the inner artery are being damaged in axial overstretch. Specifically, two of the vessels from the previously defined fetal group were perfused with nigrosin in order to dye the endothelial cells lining the lumen and visualize rupture of this innermost structure during overstretch. Furthermore, four additional juvenile MCAs were similarly perfused and overstretched quasi-statically; however, overstretch was stopped after observing intimal failure and prior to reaching complete disruption of the vessel wall. Regions of disrupted intima were subsequently imaged at 10x (512 x 512 pixels) using a laser scanning confocal microscope (Olympus, Fluoview 1000). Serial slices were taken through the vessel wall in 2 μm increments and elastin structures were imaged with the 488 nm laser.

5.3.6 Statistics

One-way ANOVA was used to determine significant differences ($p < 0.05$) of the intimal failure thresholds between age groups. Intragroup comparisons were also made between the intimal failure threshold and previously reported values of the axial stretch at both maximum stiffness and maximum stress [100]. For these comparisons, significant differences were determined with a Wilcoxon Signed-Ranks Test for Paired Samples ($\alpha = 0.05$).

5.4 Results

A total of 41 specimens were successfully stretched to failure. Unloaded lengths, reference outer diameters, and *in vivo* stretches of the specimens tested are provided by age group for reference (Table 5.1)

Partial disruptions of the inner artery wall prior to ultimate failure were observed in nearly all specimens, independent of age, during failure tests. The disruptions were visualized through the camera view as circumferential segmented bands (Figure 5.1) which generally appeared within the duration of a single frame (0.33 sec). The layers involved in the disruption could not be clearly discerned, but tears appeared to be limited to the intima, possibly to include the internal elastic lamina. The disruptions were not associated with any significant changes in the measured axial load, and in many cases vessels continued to hold pressure with no immediate change in outer diameter; subsequent vessel tearing at ultimate failure usually initiated within or near these bands. It was common for multiple subfailure disruptions to occur in each specimen. The earliest disruption in each vessel occurred at a stretch ratio of 1.56 ± 0.17 ($\mu \pm$ SD), with the lowest of all samples occurring at 1.29 (all stretches relative to the unloaded length). The stretch value at which intimal disruption occurred was not dependent on age (Figure 5.2).

Comparing the threshold of intimal disruption with previously reported stress-stretch data for these same vessels [100] showed that the mean stretch at disruption occurred beyond the mean stretch at the maximum stiffness (significantly beyond for fetal, newborn, and adult groups) yet prior to reaching the ultimate stress (significantly prior for newborn and juvenile groups; Figure 5.2). Failure occurred at 84, 82, 70, and 93% of the strain at ultimate stress and 67, 68, 61, and 78% of the strain at catastrophic

failure for fetal, newborn, juvenile, and adult groups, respectively. Mean ± standard deviation failure stretches are reported in Table 5.2.

Confocal imaging and analysis of lumen-dyed vessels showed rupture of both the internal elastic lamina and endothelium. Video observation of vessels with a nigrosin-dyed endothelium showed rupture of this inner-most structure in a manner similar to that observed in those without dye. Furthermore, confocal imaging of regions containing intimal failure revealed rupture of the internal elastic lamina yet intact media and adventitia (Figure 5.3).

5.5 Discussion

The objective of this study was to quantify the occurrence and threshold of intimal failure in cerebral arteries and how these change with development. Vessels were overloaded axially as we have hypothesized this to be the dominant loading mode in head trauma. Ovine middle cerebral arteries from four different age groups were used. We observed partial disruptions of the inner artery wall in all specimens, independent of age. While multiple disruptions in the same vessel were frequently observed, the earliest disruptions generally occurred after the vessel reached maximum stiffness but prior to the ultimate stress. Further analysis indicates that disruption includes failure of both the internal elastic lamina and endothelium. Comparison of results with the literature suggests that, if found *in vivo*, such subfailure damage may provide a mechanistic link between TBI and the subsequent increased risk of stroke.

5.5.1 Intimal failure in the literature

Also motivated by blunt trauma, a similar investigation of intimal failure during axial loading of porcine aorta and human carotid specimens yielded numerous findings comparable to those in our study. As in our work, Stemper et al. [125] observed that intimal failure was not detectable in the stress-stretch data, that disruption occurred at multiple locations along the length of the vessel, and that failure was oriented in the circumferential direction. Furthermore, Stemper et al. found disruption to generally occur prior to catastrophic failure and qualitatively showed in a couple of samples that it occurred after reaching maximum stiffness (see Figure 2 in [125]. We, too, found intimal failure to initiate between these two points. Our thresholds of failure fell between their reports of 60.1 and 85.0% of the strain to catastrophic failure in human carotid specimens and porcine aortas, respectively.

Confocal imaging and analysis of lumen-dyed vessels showed rupture of both the endothelium and the internal elastic lamina with medial and adventitial layers intact. As similar analyses were not done in previous studies of axial overstretch [125], we compare our findings to the literature on angioplasty. Specifically, circumferential overdistension has also been shown to rupture the IEL, with no gross changes to the extracellular fibers and elastin [84], and to tear the intima while leaving the media and adventitia intact [82, 87]. Related forms of damage have also been observed such as focal dehiscence, or separation, of the IEL [81, 126] and denudation of endothelial cells [77, 81]. One study in human femoral arteries also found intimal rupture; however, medial and adventitial rupture commonly occurred prior to intimal failure [127]. While this latter finding somewhat contradicts our observations, it is not expected that circumferential and axial

mechanics be identical given the structural disparities between the axial load-bearing adventitia and the circumferential load-bearing media [70], as well as variations in mechanics throughout the arterial tree [59]. Furthermore, *in vitro* studies of angioplasty-like loading are often complicated by the presence of atherosclerosis in test specimens [82, 127].

5.5.2 IEL failure and changes with development

As prior histology on these same vessels has shown the IEL to be thicker than the intima [100], we hypothesize that failure of the IEL was primarily responsible for the visible disruption observed using our video camera, and that the intima and IEL ruptured simultaneously. While little is known about the failure thresholds of elastin sheets, selective removal of collagen or elastin from biological tissues has shown that elastin exhibits a relatively distensible, linear force-displacement response while collagen undergoes significant stress stiffening with stretch ([75] [128]. Therefore, one might expect the adventitial collagen, which is believed to protect against overdistention [38], to fail prior to the elastic lamina. In fact, we made this very observation in our recent investigation of collagen damage in arterial overstretch (Chapter 4), though discussion of elastin damage was left for inclusion in the present work. In that study, MCAs from juvenile sheep were overstretched axially to various subfailure or failure levels. Samples stretched to failure exhibited damage to both the IEL and collagen (as identified with a novel probe of tropocollagen unfolding; Figure 5.4). However, in many instances of subfailure stretch, collagen damage was observed in the absence of IEL failure, suggesting that collagen damage commonly occurs at lower stretch values. Therefore, we

suspect that breakdown of load-bearing collagen fibers induces high local strains sufficient to rupture the internal elastic lamina and adjoining intima. However, as IEL failure was occasionally observed in the presence of only mild collagen damage, the failure thresholds for each are likely close to each other, at least in the case of juvenile sheep.

Our belief that intimal failure (and concurrent failure of the internal elastic lamina) is preceded by collagen damage is further supported by our observation that disruption generally occurred after vessels reached the point of maximum stiffness (Figure 5.2, Table 5.2). This point [23, 109-112], or a point shortly thereafter [104, 113, 114], is commonly defined as the yield point and has been associated with the onset of collagen damage in ligament [51, 113], tendon [92], and arteries (Chapter 4).

While reaching the maximum stiffness may be a prerequisite to subsequent intimal/IEL failure, it is interesting to note that despite there being significant changes with age in the stretch at maximum stiffness (Figure 5.3; the reader is referred to [100] for statistical differences), no changes were found in the threshold for intimal failure. The stretch at maximum stiffness should be expected to vary with age as it is likely a function of the relative content of collagen and elastin in the wall which we previously showed to change with development [100]. Furthermore, the lack of change in the failure stretch of the intima/IEL is not surprising as elastin has been shown to be very stable over a lifetime, having <1% turnover in a year [129], the longevity of a human life span [130], and minimal synthesis in the adult animal [130-132]. In fact, “elastin expression in most tissues occurs over a narrow window of development, beginning in midgestation and continuing at high levels through the postnatal period” [133].

5.5.3 Pathology of IEL failure

Failure of the internal elastic lamina could have important implications for atherogenesis and aneurysm formation post-TBI if found *in vivo*. The IEL serves as an important barrier between the endothelium and inner smooth muscle cell layer [134] and may have a role in atherogenesis through its modulation of diffusion [135, 136]. This barrier, when intact, enables passage of endothelial and smooth muscle cell projections [137-139] through its fenstrations (holes) yet inhibits migration of fibroblasts [127] and prevents passage of higher molecular weight lipids. Consequently, damage of the IEL results in large increases of low density lipoprotein (LDL) in the media [140]. Furthermore, multiple authors [141-145] have stated that degeneration, fragmentation, and splitting of the internal elastic lamina are associated with the initiation of aneurysms [146]. As expression of elastin beyond the postnatal period is low [133], repair of a torn IEL would likely be slow, and ultimately incomplete, and risks associated with failure persist. One investigation tracked the repair of torn IEL at days, weeks, and months following angioplasty. Results suggested that full recovery may take close to one year as reconstruction of the IEL had not even begun after two months and regeneration was still incomplete at six months postinjury [87].

5.5.4 Pathology of endothelial failure

Our observed failure of the endothelium also has important physiological implications post-TBI if found *in vivo*. While the list of roles that the endothelium plays continues to grow, a few notable ones are that it serves as a nonthrombogenic barrier between the blood and arterial wall, synthesizes vasoactive materials, and controls

smooth muscle cells [70]. Consequently, endothelial damage initiates a litany of pathological responses such as platelet deposition, migration of medial smooth muscle cells [147]), the formation of neointima, and accumulation of thrombi [148]. Compounding the risk of constriction is platelet-activated thromboane, a vasoconstrictor [70], and an increased sensitivity to vasospasm [33, 149]. Furthermore, mechanical damage to the endothelium in the presence of excess lipids is known to accelerate atherosclerosis [150-153]. While reendothelialization may begin within a week of injury [147, 154]), endothelial cells may not completely mature for three months [87]. It is unclear how these rates may be affected by the absence of abluminal IEL.

5.5.4 Implications for TBI

The observed intimal/IEL disruption prior to ultimate failure demonstrates that cerebral arteries can be damaged significantly in the absence of hemorrhage. Similar disruptions in larger arteries following trauma have been associated clinically with subsequent occlusion, stenosis, and aneurysm, with possible subsequent stroke [123, 155]. There is little evidence that similar vascular injury and pathology may occur in the smaller cerebral arteries, but this may be due to difficulty of detection. Clinical studies show that TBI is a significant risk factor for both ischemic and hemorrhagic stroke, but mechanisms for the link between TBI and stroke have not been identified [121, 122]. The connection is almost surely multifactorial, but it seems reasonable to expect that nonhemorrhaging, structurally damaged cerebral vessels would be dysfunctional and potentially contribute.

We did not observe any differences with age in our study, but none of the vessels

were obtained from animals of advanced age. Thus, while likely important to TBI and possible subsequent stroke, trauma-induced subfailure disruption of the intima does not likely contribute in different ways to outcomes of TBI in children versus adults, at least directly.

Future work should explore the occurrence of intimal failure in other cerebral blood vessels (arterioles, veins, venules) and at higher loading rates so that it can subsequently be identified in models of head trauma. As the level of strains in TBI it is still unknown, the likelihood of failure remains unclear. However, hemorrhaging is common. Therefore, it is likely that subfailure damage of nearby vessels should also be present. Should it be discovered, it would not only provide a possible mechanistic link between TBI and subsequent stroke – and a new strategy for treatment of patients, but it would also offer insights into the distribution of vascular strain in head trauma.

5.5.5 Limitations

A few limitations of the study are noted. First, arteries were stretched quasi-statically rather than dynamically as would occur in TBI. It is not yet known what effect rate may have on these findings. Stemper et al. still observed intimal disruption at high rates in their study [39], and strain at initial subfailure decreased with increasing rate. Second, tests were only carried out on middle cerebral arteries, one of the largest arteries in the cerebrovasculature and one not commonly damaged during TBI. Future work should explore intimal failure in veins and smaller arterioles and venules. Third, stretches were calculated with actuator displacement rather than tissue fiducial markers, which could lend to higher reported stretch values since axial stretch tends to be higher at the

ends where circumferential stretch is constrained [156]. Comparisons between stretch values calculated from adventitial microspheres and actuator motion indicate differences between 2 and 10% [104]. Finally, confirmation of damaged structures was only done in a subset of all the vessels tested. Endothelial failure was identified in two out of two fetal samples and IEL failure in four out of four juvenile samples. Future work could verify that these same structures are damaged in the other age groups.

5.6 Conclusion

For the first time, axial stretch has been shown to induce subfailure damage of the intima and IEL of intracranial arteries. This was observed over four phases of development (fetal, newborn, juvenile, adult), and the stretch threshold at which it occurred did not vary with age. Disruption included failure of both the endothelium and internal elastic lamina, structures critical to vessel health and function. Given that similar loading and vessel failure have been implicated in blunt cerebrovascular injury, we hypothesize that this same mechanism may provide a mechanistic link between TBI and the subsequent increased risk of stroke. Additional work should be done to identify the occurrence of intimal failure in models of head injury.

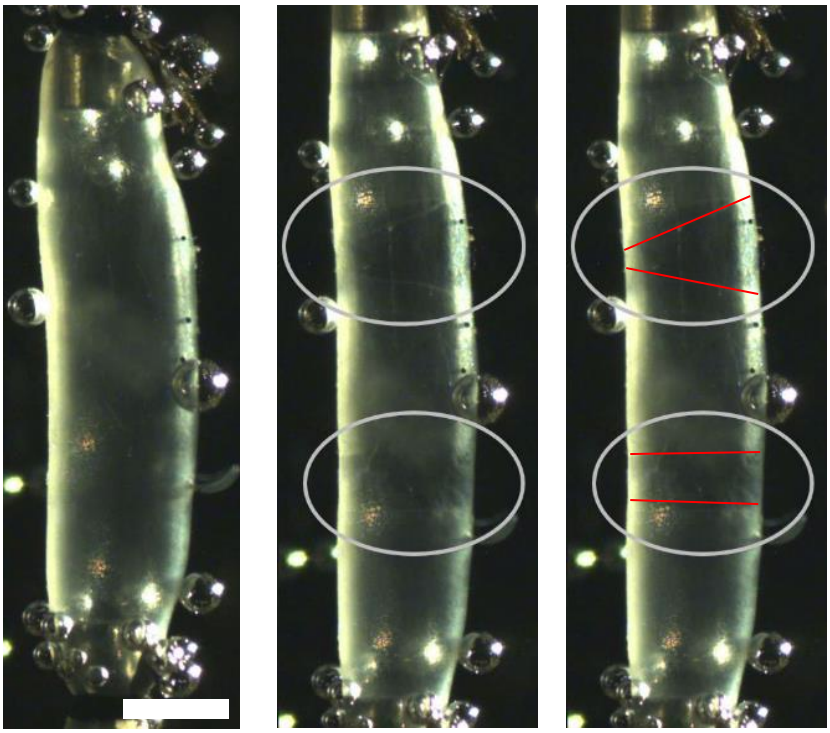

Figure 5.1: Ovine MCA prior to (left) and after appearance of (middle and right) intimal layer disruptions (circled) during a pressurized axial stretch test. For clarity, the approximate boundary of the failed intima has also been defined with red lines (right). Scale bar is 1 mm.

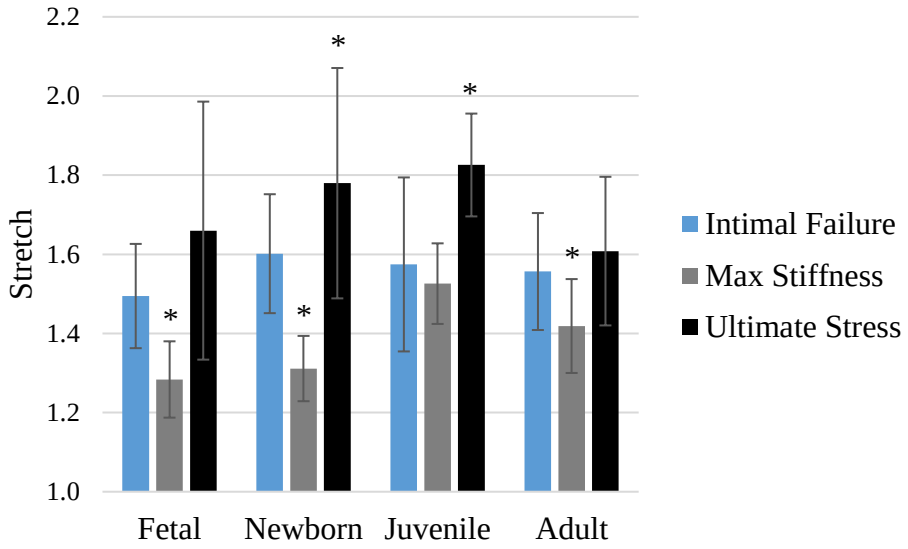

Figure 5.2: Stretch thresholds of intimal failure relative to the stretch at maximum stiffness and the stretch at ultimate stress by age group. Significant differences between age groups were not found for the stretch at intimal failure (blue). However, for all groups the mean stretch at intimal failure fell between the stretch at maximum stiffness (gray) and the mean stretch at ultimate stress (black). Significant differences relative to intimal failure in the same age group (*) were determined with a Wilcoxon Signed-Ranks Test for Paired Samples ($\alpha = 0.05$).

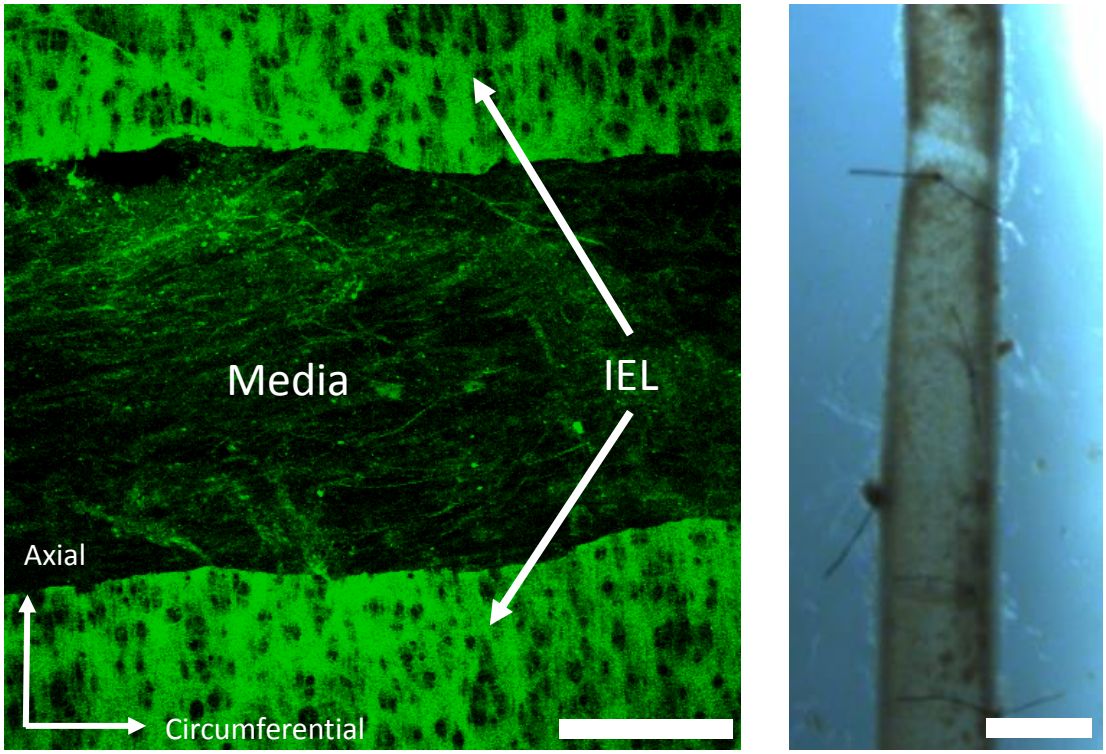

Figure 5.3: Failure of the internal elastic lamina (IEL, left) and endothelium (right). Left: confocal image of ruptured internal elastic lamina (IEL). Fenestrations (holes) in the IEL and some of the elastin from the intact media can also be seen. Scale bar is 50 µm. Right: image captured during overstretch showing failure of the nigrosin-dyed endothelium. Scale bar is 0.5 mm.

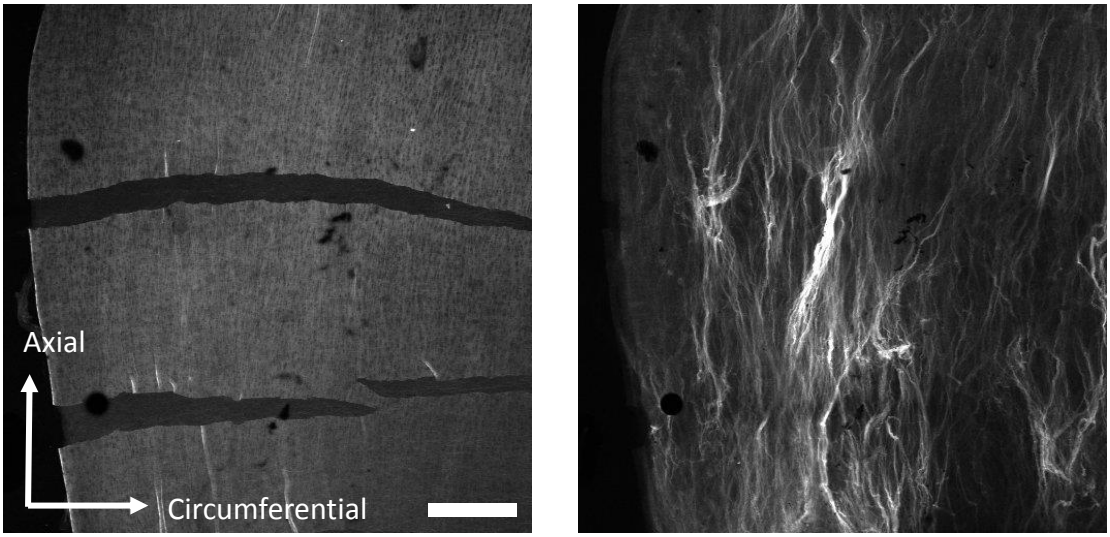

Figure 5.4: Confocal images at two different depths of the arterial wall showing failure of the internal elastic lamina (left) in the presence of disruption of axially oriented collagen in the adventitia (right). Images are taken from a recent study of axial overstretch in lamb MCAs (Chapter 4). Collagen damage was detected with collagen hybridizing peptide (CHP), a recently developed marker of tropocollagen unfolding. Axes and scale bar (200 μm) apply to both images.

Table 5.1: Mean ± standard deviation unloaded lengths, reference outer diameters, and axial *in vivo* stretches for each age group.

	Fetal (n=10)	Newborn (n=11)	Juvenile (n=11)	Adult (n=9)
Unloaded length (L)	4.88 ± 1.20	3.71 ± 0.54	4.60 ± 1.30	4.22 ± 1.30
Outer diameter (D_o)	0.61 ± 0.06	0.70 ± 0.09	0.78 ± 0.12	1.04 ± 0.15
Axial *in vivo* stretch (λ_{IV})	1.15 ± 0.10	1.11 ± 0.06	1.16 ± 0.05	1.07 ± 0.04

Table 5.2: Mean ± standard deviation stretches at earliest intimal disruption, maximum stiffness, ultimate stress, and catastrophic failure for each age group. The first three metrics are also displayed graphically in Figure 5.2.

	Fetal (n=10)	Newborn (n=11)	Juvenile (n=11)	Adult (n=9)
Stretch at earliest intimal disruption	1.49 ± 0.13	1.60 ± 0.15	1.57 ± 0.22	1.56 ± 0.15
Stretch at maximum stiffness	1.28 ± 0.10	1.31 ± 0.08	1.53 ± 0.10	1.42 ± 0.12
Stretch at ultimate stress	1.66 ± 0.33	1.78 ± 0.29	1.83 ± 0.13	1.61 ± 0.19
Stretch at catastrophic failure	1.94 ± 0.38	1.90 ± 0.23	1.93 ± 0.11	1.74 ± 0.27

CHAPTER 6

DETECTION OF VESSEL DAMAGE IN AN OVINE CLOSED-HEAD INJURY MODEL

6.1 Abstract

Cerebrovascular disruption and dysfunction are common sequelae of TBI. Previous research has investigated alterations in vessel function following trauma, but little consideration has been made for changes to vessel microstructure that may contribute to disease progression. Therefore, the objective of the present work was conduct preliminary investigations to detect structural damage to the vascular wall in an ovine closed-head injury model. Cortical hemorrhage in the absence of skull fracture was successfully achieved by a left temporal blow with a captive bolt stunner through a padded steel plate. Subarachnoid hemorrhage and leaks during India ink perfusion identified regions likely to have incurred high vascular strains. Intact cortical arteries and veins greater than 150 and 300 μm in diameter, respectively, were dissected from these regions and stained with a marker of collagen damage. Fluorescence microscopy of samples from two ewes did not detect collagen damage or disruption of the internal elastic lamina. Recommendations are made for increasing the severity of loading and sensitivity of damage detection to better determine the contribution of the cerebrovascular ECM damage in head injury.

6.2 Introduction

Cerebrovascular disruption and dysfunction are common sequelae of TBI. In addition, recent clinical studies have shown that TBI is a significant risk factor for stroke, even up to five years after the initial injury [121, 122]. Previous research has investigated alterations in vessel function following trauma [3], but little consideration has been made for changes to vessel microstructure that may contribute to disease progression. As it is well established that cerebral vessels are torn and bleed in TBI [2, 3], it follows that other vessels experience deformations that are significant but not severe enough to produce hemorrhage. Recent *in vitro* studies have shown that vessel overstretch alters both the mechanical properties [57] (Chapter 3) and contractility [67] of cerebral vessels. Furthermore, subfailure deformations of isolated arteries have been shown to damage arterial collagen (Chapter 4) and elastin (Chapter 5). These structural alterations may help to explain the experimentally observed mechanical/functional as well as play a role in the clinically reported symptoms post-TBI. However, as subfailure mechanical and microstructural alterations of cerebral vessels have only been observed *in vitro*, an essential step to exploring this mechanistic link is to identify stretch-induced vessel damage acutely in a model of head injury.

Numerous animal models of head injury have been used to study vascular damage in TBI. Many of these have focused on relationships between head/brain loading and complete vessel disruption (hemorrhage), while a few have evaluated changes to nearby, intact vessels through the administration of vasoactive chemicals or pressure changes [7-15]. The majority of these latter studies have demonstrated dysfunction in nonhemorrhagic vessels, suggesting changes to smooth muscle and endothelial cells.

While these studies provide evidence that trauma can alter the active response of intact vessels, is remains unknown the degree to which the extracellular matrix is damaged.

The objective of the present work is to characterize acute structural damage to the vasculature in a previously published model of closed-head injury in sheep [24, 25]. Advantages of this model over typical rodent models are numerous. These include a biomechanically realistic blunt impact to the intact head that results in coup and contrecoup contusion [24, 25], typical of human injury. The gyrencephalic brain of the sheep also allows better translation of injury-related findings both from this study and from future studies directed at disease development and healing. The model is also important for direct study of blood vessels since the vessels on the brain surface are larger and more robust than those from smaller animals.

The nature of loading experienced by blood vessels during TBI is currently unknown. Brain deformations have been estimated using both experimental [17, 157, 158] and computational [159-161] models of TBI, but study of accompanying vessel loading has been limited due to the required complexity of the models. As a result, it is difficult to predict locations where vascular damage would be most prominent. Further, it is not clear whether vessels of different types (artery, vein), sizes and geometries might be relatively more susceptible to injury. For example, branchpoints have been studied as regions of stress concentration [162, 163]; they are also commonly associated with aneurysm development and flow abnormalities and have been shown to have unique microstructural characteristics [146, 164-170]. We hypothesize that vascular microstructural damage will be greatest at the impact site, be most prevalent among veins, and be preferential to bifurcations.

6.3 Methods

Using an established model of TBI [24, 25], adult sheep were subjected to a closed-head impact. Cortical vessels were dissected and studied for signs of structural damage. Investigations were limited to subarachnoid vessels as hemorrhaging on the surface of the brain has been shown to be more common than contusion with this model [24, 25, 171]. As initial efforts were unsuccessful at producing hemorrhage, numerous iterations of the methods were made. Sections 6.3.1-6.3.7 describe the general methods used in these exploratory studies and additional details pertinent to specific investigations are included in Section 6.4.

6.3.1 Animal preparation and instrumentation

Experiments were conducted on Colombia-Rambouillet ewes shortly after they had given birth to lambs as part of research ongoing in the Lamb Intensive Care Unit at the University of Utah (LICU). All work was done with University of Utah IACUC approval. Following the delivery, the anesthetized animals were placed supine on a table with their heads supported on a horizontal platform that otherwise allowed free motion. Straps were used to constrain shoulder and body motion. Heart rate, mean arterial pressure (measured with a cuff on upper front limb), and oxygen saturation were monitored continuously and recorded every 15 mins. Blood gas content was measured and documented hourly. Fiducial markers were used to track motion of the superior surface of the head during impact to provide a rough approximation of head motion. When the sheep had horns, markings were drawn directly onto the horns. Otherwise, an incision was made on the superior surface of the skull and either bone screws or markings

(permanent marker) were placed on the superior surface. At least one marker was centered on the sagittal suture lying within the coronal plane passing through where horns would grow. A high speed digital video camera (Vision Research, Phantom Miro eX4) situated directly above the fiducial markers was used to visualize motion during impact. Images were collected at high frame rate (1,900-12,000 Hz) with a pixel resolution ranging between 64x128 and 480x640. The impact region was shaved and an impact plate was strapped to the sheep head between the supraorbital process and the external auditory meatus – serving to protect the skull from fracture. Occasionally, rubber was placed between the impact plate and the head to further prevent fracture. In some cases, heparin (5 mL of 1000 IU/mL) was injected to inhibit coagulation of the blood.

6.3.2 Head impact and survival

Heart rate and mean arterial pressure were recorded every minute for the 5 min prior to and 10 min after impact to compare changes relative to those expected for this model [24, 172]. A humane captive-bolt stunner (Karl Schermer and Co, model KC; or Accles & Shelvoke, CASH Magnum Concussion) was placed flush against the impact plate. An explosive charge was then used to deliver either a temporal or parietal blow through the secured plate. The head was allowed to move freely over the platform in response to the impact. Following impact, sheep were survived for up to 6 hrs. In one case, the sheep was transported to the Imaging & Neurosciences Center at the University of Utah for magnetic resonance imaging. At the end of the procedure, the sheep was sacrificed via Beuthanasia and the brain was carefully dissected. To aid in development, several impacts were also carried out after sheep were euthanized. In these cases, impact

occurred within 3 hrs of death.

Impacts in two postmortem ewes were carried out with an alternative weight drop design. The sheep was laid on its side approximately 0.7 m from the floor; its head extended off the table and elevated by a frangible support. The aforementioned impact plate was secured to the left temporal region and the head was impacted with a 22 kg falling weight. The weight consisted of a solid cylindrical piece of steel (14.0 cm diameter, 17.8 cm length) with a stainless steel sphere (5.1 cm diameter) as an impact tip. The lower half of the sphere was welded within a hollow steel cylinder (2.5 cm tall, 0.6 cm thick) having an inner diameter matching that of the sphere. The base of the hollow cylinder (with accompanying sphere) was then centered on and welded to one flat surface of the 22 kg weight. A large eye ring was also welded to the opposing end of the solid cylinder so that the weight could be suspended with a rope. A double-pulley was used to lift the weight through a PVC tube (15 cm inner diameter, 1.8 m long). The tube, secured to a portable, vertical wooden frame, was centered over the impact plate. Upon release of the rope, the weight fell freely, impacting the sheep head and landing within a plastic bin lined with sheets of rubber. Free fall distances prior to impact were 1.07, 1.37, or 1.65 m.

6.3.3 Brain removal

Because impact-induced damage to the cortical vessels was of primary interest in this work, removal of the brain was done with care. Skin, muscle, and eyes were removed. A window between the occipital condyles was chipped away with a rongeur such that the posterior side of the spinal cord and part of the cerebellum were visible. The superior surface of the sinus was also cut away with a rongeur. The skull was then

removed in three pieces: a 1 cm wide strip over the sagittal suture and two lateral plates. The two lateral plates were removed by cutting alongside the sagittal suture and along the posterior edge of the parietal bone. The coronoid process was then removed to continue cutting along the superior edge of the zygomatic arch and through the orbit. The path was then completed by making a fourth cut through the sinus. All cuts were made with a Dremel tool (Dremel, 4000-2/30 120-Volt Variable Speed) having a flexible extension and a 5/16" rounded high-speed cutter (Dremel, bit #114). This cut effectively through the skull yet slow enough that damage to the dura could be avoided. The dura was subsequently cut with scissors, taking care to point scissor blades tangent to or even away from the brain surface. The remaining strip of bone overlying the sagittal suture was then removed by cutting each of the bridging veins and the dural connections to the falx cerebri. The brain was finally lifted out of the skull base with some additional cutting of the spinal cord, tentorium cerebelli, cranial nerves, internal carotid artery, and olfactory lobe. Immediately following removal, images of the brain were taken from all six orthogonal views. Locations of subarachnoid hemorrhage were documented and the skull was examined for any signs of fracture.

6.3.4 India ink perfusion and vascular mapping

Perfusion with 10% India ink was used to better map the vasculature and localize vessel disruption. The arachnoid was removed from the proximal 4-5 mm of each MCA and the cranial lobes were separated. With one lobe underneath a stereomicroscope (Zeiss, Stemi 2000-C), MCAs were cannulated with hypodermic tubing and approximately 1 mL of India ink was slowly perfused through the hemisphere. During

this process attempts were made to identify the source of any vascular leaks. One or two major veins in the occipital lobe were occasionally cannulated to better perfuse the posterior portion of the temporal cortex. The relevant arterial and venous supplies were drawn on top of the previously taken images (Microsoft, Paint). Locations of arachnoid disruption and contusion were also identified and documented.

6.3.5 Vessel dissection

Using the methods described in Chapters 3 and 4, vessels were dissected from the cerebral cortex and studied for structural damage. As others have already shown that hemorrhaging and contusion are primarily found subjacent and contralateral to the impact site, investigations focused on vessels on the lateral surfaces of the brain. Specifically, investigations were limited to regions supplied by the middle cerebral arteries (MCA), and only damage to arteries and veins greater than 150 and 300 μm in diameter, respectively, were explored as smaller vessels likely get damaged if dissected. Figure 6.1 shows a ewe brain dissected in our lab with relevant arteries traced in black. These arteries, neighboring veins, and similar vessels on the opposing hemisphere were the targets of our study, with particular emphasis on vessels near the impact site or locations of hemorrhage. Preliminary investigations showed the impact site to consistently be located over the posterior Sylvian gyrus, approximately 1 cm distal of the main MCA branch and 1 cm superior to the rhinal fissure (Figure 6.1).

In order to facilitate vessel dissection, the cortex was divided into up to 8 regions, each of which was removed with a primary slice made parallel to the brain surface. These relatively thin (1-2 cm thick) regions were then submerged in saline and vessels were

dissected underneath a stereomicroscope (Zeiss, Stemi 2000-C). This process was repeated for both hemispheres.

6.3.6 Identification of microstructural damage

Lengths of arteries and veins from both hemispheres were dissected from the cortex. Unbranched lengths were dissected and each branchpoint segmented – retaining approximately 1 mm of length from the parent branch and each daughter branch. The origin of each segment was documented and stained with CHP according to the protocol outlined in Chapter 4. Following this, segments were cut longitudinally and laid flat on glass slides for imaging, with branched segments flattened as done by Campbell et al. [146]. As before, samples were imaged at 10x with a confocal microscope. Images of the intima were used to identify failure of the internal elastic lamina (IEL). Images of the media and adventitia were used to detect and quantify collagen damage as manifest by an increased CHP signal.

6.3.7 Quantification of head motion

While the primary objective of these preliminary investigations was to determine appropriate loading conditions and skull protection to produce cortical hemorrhage, a rough approximation of head motion was also desired. The high rate video capturing the superior view of the head during impact was exported as an .avi file (Vision Research, Phantom Miro eX4). Motion of the fiducial markers was tracked manually beginning 10 frames prior to impact and ending 4 μs after impact (MathWorks Inc., MATLAB). The clearest four points on each fiducial were picked out in the initial image and tracked

throughout all frames. These four positions were averaged to reduce noise, creating a single set of position data for the marker. Horizontal and vertical position data (in the image plane) were then individually smoothed with an SAE J211 filter, and linear accelerations within the image plane were calculated between every frame.

6.4 Results

A total of 21 ewes were used in the study, 12 of these being impacted while anesthetized and 9 within 3 hrs postmortem (for model development). Numerous iterations of the impact method eventually resulted in a procedure for inducing hemorrhage in the absence of skull fracture with the CASH Magnum Concussion stunner. This was demonstrated in the two final ewes. Coup and contrecoup hemorrhage were observed; however, neither damage to collagen nor elastin was found in the surrounding vasculature. Details of the experiments are presented in Sections 6.4.1-6.4.2 and a summary of all experiments is provided in Table 6.1.

6.4.1 Impact method development

6.4.1.1 Impact method 1 – Karl Schermer KC stunner

The Karl Schermer KC stunner was used on ewes I-X. Impacts on ewes I-VII focused on proper implementation of the head impact model, specifically, in determining the appropriate combinations of explosive charge (from weakest to strongest: C-5 Yellow, Blue, or Red), impact location (temporal or parietal), and skull protection (stainless steel or aluminum plate with thicknesses varying from 6 to 13 mm) to maximize vascular disruption while preventing skull fracture. Lack of large vessels

subjacent to the temporal impact site motivated parietal impacts in ewes IV-VII. These either resulted in skull fracture with hemorrhage or no skull fracture with an absence of hemorrhage. Ewes VIII-IX were impacted in the location and with the charge proposed by earlier groups [24, 25], that is, a temporal impact with the strongest charge (C-5 Red). A 13 mm thick steel or aluminum protective plate was used (as thinner ones deformed) and the ewes were euthanized 5-10 min after impact. No signs of subarachnoid bleeding or impact-induced leaks during the India ink perfusion were found.

Additional efforts were made to detect vascular damage in ewe X. This final ewe was injured in the same manner as the previous two, survived for 4 hrs to allow adequate time for hemorrhage to develop and conduct an MRI scan. A total of 18 arterial lengths and 9 branchpoints were dissected from the left hemisphere while 24 arterial lengths and 11 branchpoints were dissected from the right hemisphere. Damage to veins was not explored. In the left hemisphere we found partial transection of an arterial branch subjacent to the impact site (Figure 6.2). However, no hemorrhaging was observed in the MRI scan, indicating that wall transection may have been caused during dissection. In the right hemisphere we found intimal failure in one branchpoint and mild CHP staining in one length of artery (Figure 6.3).

6.4.4.2 Impact method 2 – weight drop

As hemorrhage could not be induced in the absence of skull fracture with the Karl Schermer KC stunner, and as small amounts of observed vascular disruption (Figures 6.2 and 6.3) may have been on the order of that expected to occur during dissection, efforts were turned to increasing head motion with a weight drop approach. The weight drop was

tested on two postmortem ewes (ewes XI, XII) following impact with the KC stunner. Despite designing the weight drop to exceed the performance of the stunner, it produced comparable head motion (Figure 6.4). Underperformance was likely due to overestimation of the coefficient of restitution. Dropping the weight from a higher position would have required removal of ceiling tiles which was not permitted per building code.

6.4.4.3 Impact method 3 – Accles & Shelvoke CASH Magnum Concussion stunner

Subsequent efforts continued to focus on increasing head motion with the Accles & Shelvoke CASH Magnum Concussion stunner. As this stunner had a smaller impact tip and was capable of transferring roughly 50% more energy at impact than the Karl Schermer KC stunner, significant time had to again be spent on proper implementation of the model, specifically, the appropriate combinations of explosive charge (from weakest to strongest: Orange, Black, Green, or Red) and skull protection. By evaluating device specifications, the Green charge in the CASH Magnum was estimated to transfer a comparable amount of energy to the head as the strongest charge in the KC stunner (C-5 Red). Therefore, in order to produce higher accelerations than done previously, we ultimately sought skull protection adequate for use with the strongest charge in the CASH Magnum stunner (Red). Testing on seven postmortem ewes (ewes XIII-XIX) showed that a mushroom shaped metal impact plate roughly 5 cm in diameter was needed to prevent skull fracture. Flat metal plates, despite having a variety of sizes/placements and up to 6 mm of rubber padding, resulted in fracture. Therefore, the mushroom head of the KC

stunner was removed and welded to a stainless steel plate (5 x 5 x 0.6 cm). Holes were drilled in the four corners of the plate so that the impact plate could be tightly strapped to the sheep head with paracord (Everbilt, model #52662). In addition, a 6 mm thick square piece of rubber (5 x 5 cm; Apache Mills, model #60-799-1246-01800030) was placed between the mushroom plate and the sheep head to further prevent fracture. This combination was used on three postmortem ewes (ewes XVII-XIX), and head motion was captured on two of them (ewes XVII-XVIII). The mushroom plate and rubber successfully protected all three heads from fracture, and head accelerations were more than twice that produced with the two previous methods (Figure 6.4).

6.4.2 Vascular damage following *in vivo* impacts with CASH Magnum stunner

The significant increase in head acceleration with the CASH Magnum stunner led to use of this model in two anesthetized ewes (ewes XX-XXI). As in the three postmortem ewes (XVIII-XIX), impact did not fracture the skull of either ewe. Furthermore, impact successfully produced temporal subarachnoid hemorrhages in the absence of skull fracture, matching, in part, our desired morphologic outcomes for the model. However, neither collagen damage nor failure of the IEL was found in neighboring vessels. Details of both investigations follow.

6.4.2.1 Ewe XX

Heparin was administered 15 min prior to impact and the ewe was survived for 1 hr. Head acceleration was comparable to that observed in preliminary impacts in cadavers

(Figure 6.5). Four min after impact the mean arterial blood pressure (MAP) was found to rise roughly 10% (Figure 6.6). Coup and contrecoup subarachnoid hemorrhages were found in the left and right temporal cortexes, respectively, but bleeding was more pronounced in the right (compare Figure 6.7a and 6.9a). India ink perfusion of the right hemisphere localized two leaks proximal to veins (Figure 6.7c, d); neighboring arteries and veins were dissected (Figure 6.8). A 0.9 mm tear in the arachnoid was found over a sulcus (Figure 6.8). One site of contusion was also observed, having a parenchymal depth of 2.5 mm (Figure 6.8), though this region was only vascularized with vessels < 100 μm in diameter, too small to dissect. Ink perfusion of the left hemisphere localized one leak in the temporal cortex subjacent to the impact. The leak was most proximal to a vein; however, SAH was diffuse within the gyrus which was also vascularized with a similarly sized artery (Figure 6.9b-d). This artery was dissected (Figure 6.9d); however, the closest veins were too small to dissect. No arachnoid tears or contusions were found. A total of five arterial and six venous segments were dissected from both hemispheres (Figures 6.8 and 6.9d), stained with CHP, and imaged. Neither collagen damage nor failure of the IEL was found. While many of the dissected segments contained branchpoints, time did not permit investigation of these.

6.4.2.2 Ewe XXI

The ewe was euthanized 15 min after impact as time constraints with the collaborating lab did not permit a longer survival. This was believed to be sufficient as one previous investigation did not show any increase in the incidence of SAH with longer survivals [173]. Heparin was not administered. Mean arterial pressure spiked for the first

minute after injury, but decreased to roughly 20% below baseline by minute four (Figure 6.6). No hemorrhage was observed in the left hemisphere and, as expected, careful inspection of India ink perfusion showed no leaks (Figure 6.10). No vessels were dissected from this hemisphere. Two regions of SAH were found in the right temporal cortex (Figure 6.11). Ink perfusion of the right temporal cortex did not show any leaks in the more anterior lesion; however, due to disruption of a branch of the MCA during dissection, ink didn't fully perfuse the surrounding vasculature. Ink was found to collect in the sulcus of the more posterior lesion; however, the source of the leak could not be identified. A total of 5 arteries and 4 veins were dissected and imaged. No IEL failure was found. CHP staining was not done as tissue examination/dissection was completed beyond 48 hrs postmortem, at which point tissue is known to degrade [70].

Significant lesions were also found in the brain stem and ventral surface of the right piriform cortex (Figure 6.12). The brain stem contained both subdural and subarachnoid hemorrhage; however, coagulation of blood prevented thorough investigation of vascular damage. Small lesions of symmetric SAH were also found lateral to where the oculomotor nerves pass through the arachnoid. As these lesions were focal, the subjacent vasculature was carefully investigated for damage. Unfortunately, efforts to perfuse the subjacent vessels were unsuccessful and no vessel failure could be identified under the microscope. The largest neighboring vessels were veins roughly 200 μm in diameter, too small to dissect.

6.5 Discussion

The objective of the present study was to characterize acute structural damage to the cerebrovascular wall following closed-head impact. We hypothesized that microstructural damage would be greatest subjacent to the impact, most prevalent in veins, and preferential to bifurcations. We tested this by implementing a previously published model of head injury in sheep [24, 25]. Difficulty reproducing hemorrhage in the absence of skull fracture led to significant iterations to the study methods. These consisted of three distinct impact approaches each with various combinations of loading magnitude, skull protection, and impact locations. Studies over 19 ewes (9 postmortem, 10 anesthetized) ultimately resulted in a method for preventing skull fracture while accelerating the head with the strongest explosive-driven captive bolt stunner on the market (CASH Magnum Concussion, Red charge). This final approach produced head accelerations comparable to that published previously [174] and, as demonstrated in two final impacts of anesthetized ewes, induced cortical hemorrhage. Therefore, due to the delays in replicating the published model, cerebrovascular damage could only be meaningfully studied in 2 out of the 21 ewes impacted. Neither IEL disruption nor collagen damage was found in these final investigations. The main contributions of the work are a detailed protocol for producing hemorrhage in a closed-head impact, methods for tracking and quantifying the associated head motion, and techniques for careful brain resection and detection of hemorrhage sources. Additional work should be done to further increase the severity of the loading and improve detection of damage in smaller pial vessels.

6.5.1 Comparison of head motion, physiological response, brain lesions, and impact approaches

The primary contribution of this work is a detailed procedure for producing cortical hemorrhage in the absence of skull fracture. While this was previously achieved by two other groups, our best attempts to replicate their methods did not produce cortical hemorrhage. Numerous iterations resulted in a procedure capable of producing head accelerations, physiological responses, and brain lesions comparable to previous reports.

6.5.1.1 Head acceleration

Not only did our modified model successfully produce cortical hemorrhage in a nonpenetrating impact, but head motions were comparable to one report. Head kinematics were quantified by tracking one point drawn either on top of a (short) horn or on the surface of the skull midway between where horns grow. Impact with the CASH Magnum stunner produced peak accelerations of 895 and 616 G's in two postmortem ewes and 672 G's in one anesthetized ewe (Figure 6.5). Two previous investigators also quantified head motion in a similar model [25, 174], but only one clearly defined their coordinate system [174]. This latter study used a nine accelerometer array to quantify angular and linear head accelerations about three axes. Data provided in Figure 2 of [174] were analyzed to estimate the linear acceleration of their representative sheep head had they used our motion tracking approach. Given a distance of 65 mm between their anatomical origin and the bregma (approximate location where we draw our marker; distance measured on one of our ewes) yields a linear acceleration of 703 G's, comparable to ours (Figure 6.5). While this one-dimensional analysis is far from a

complete comparison of head motions, it does provide some assurance that our impact is similar to that produced by the Adelaide group. It is interesting to note, though, that our reported linear accelerations (Figure 6.5) better match the general shape of their impact force readings than do their own accelerometer readings (see Figure 2 in [174]). The higher frequency oscillations in their readings suggests that accelerometer attachment to the skull was not perfectly rigid. Therefore, it is unclear how accurate their reported peak accelerations are.

6.5.1.2 Physiological response

The ewe's physiological response in our final impact was also comparable to a previous report. We found a delayed, 10% increase in mean arterial pressure (4 min) in ewe XX but a sudden increase (within 1 min) followed by a decrease below baseline in ewe XXI (Figure 6.6). This latter behavior was comparable to that reported by Lewis et al. [24]. A similar behavior was also observed by Byard et al. [172]; however, both the magnitude and time above baseline was roughly 6 times greater than in our study and that by Lewis et al, possibly indicative of a more severe injury as Byard used a stronger charge (No. 17) than Lewis et al. (No. 13).

6.5.1.3 Brain lesions

One final comparison demonstrating the similarity between our modified model and previous reports is the nature of cerebral hemorrhage. Three publications quantified the incidence of subarachnoid hemorrhage without fracture of the inner table of the skull. The authors report SAH in 6 of 8 [24], 11 of 12 [171], and 4 of 8 [25] sheep when using

the strongest charge. Furthermore, impact contusions were found in 3 of 8 [24], 1 of 12 [171], and 2 of 8 [25] sheep. Though the number of our successful impacts are fewer, we found comparable ratios with SAH in 2 of 2 and impact contusion in 1 of 2 ewes. In addition, one of the groups reported that the extent of bleeding tended to be more pronounced at the side contralateral to the impact [171], in agreement with what we observed. Finally, one of the models reported brain stem lesions [24] which we also observed in ewe XXI.

It is still unclear why our initial attempts to replicate the methods of previous groups did not produce cortical hemorrhage; however, three important factors may be differences in the sheep breed/gender, the model of impactor used, and subtle variations in the manner in which impact was administered. Closed-head impacts in sheep have been conducted by at least two groups: researchers at the University of Adelaide in Australia [24, 172-175] and others at the University of Münster in Germany [25, 171]. Both groups placed the sheep in the prone sphinx position and allowed free rotation of the head during a lateral impact with a Karl Schermer MKL stunner. The Australian group conducted their experiments in male Merino sheep and the German group in an unspecified breed and gender. In contrast, the nature of our collaboration caused us to use Colombia-Rambouillet ewes that had just given birth. While we do not know how our early results might have varied if a different breed/gender had been used, it is a variable that we had to work with. Furthermore, the two previous groups employed the Karl Schermer MKL stunner which was no longer on the market when we began our studies; therefore, we purchased a comparable one, the Karl Schermer KC stunner. To the best of our knowledge, both stunners use the same power loads; however, communication with a

sales representative suggests that the MKL model had a smaller, 4 cm diameter ball-shaped impact tip which may have transferred force differently. Finally, variations in the administration of impact existed among the different investigators; namely, skull protection, stunner restraint, and possibly impact location. Skull protection has varied from flat plates, contoured plates [24]) and anatomically-shaped rubber bolts without an impact plate [25]. At least one group made an incision so that the plate could be placed below the skin [24] and personal conversations with the group at the University of Adelaide have revealed that more recent studies have not used any skull protection. Furthermore, the tension of the elastic securing the plate to the head was never addressed in prior studies, though this too may be an important factor affecting energy transfer. While most investigators held the stunner by hand when firing, two of the investigations secured the stunner to minimize recoil [25, 174]. Doing so should increase both the repeatability and magnitude of loading. Lastly, differences in the terminology used to describe the placement of the impact plate were found in the literature. Authors described the lateral impact as being centered above the temporoparietal suture [24], at the midpoint between the supraorbital process and the external auditory meatus [172, 175], over the temporal fossa [171], or simply as temporal blows [173, 174]. It is unclear whether these are mere differences in the chosen anatomical descriptors or intentional variations in impact placement. If the latter is true, variations are still subtle as all of these positions fall within a few centimeters of each other. The effect that these slight variations may have on skull fracture and head motion have not been investigated. In our work, cortical hemorrhage in the absence of skull fracture was achieved by also placing the sheep in the prone sphinx position and allowing free rotation of the head during lateral impact;

however, impacts were carried out with a CASH Magnum Concussion stunner. We, too, used a steel impact plate to prevent fracture; however, we required the addition of a 6 mm thick piece of rubber between the impact plate and sheep head to prevent fracture. This is likely due to the increased energy of the CASH Magnum relative to the Karl Schermer stunner. No rigid stunner restraint was employed. We explored left temporal and left parietal impacts, but due to the increased susceptibility of the parietal bone to skull fracture, returned to left temporal blows. Our temporal impacts have been centered at the midpoint between the supraorbital process and the external auditory meatus but, most recently, closer to or at the level of the external auditory meatus with the CASH Magnum stunner. This modification enabled the impact plate to lie more vertical, facilitating a more horizontal impact. We do not believe this was critical to obtaining cortical hemorrhage as the plate was not always positioned in this manner during preliminary impacts where comparable accelerations were achieved (ewes XVII-XVIII).

6.5.2 Brain removal and India ink perfusion

The second contribution of this work was two techniques to help facilitate detection of vascular damage. The first of these was a protocol for removing the brain without inducing damage to surface vessels. Critical to success of this was patient use of a ball Dremel tool and following the path and sequence outlined in Section 6.3.3. Neurosurgeons routinely cut into the skull without damaging the brain; however, this is typically done in living patients. Time after death increases adhesion of the dura to the skull, making it increasingly difficult to prevent dural damage. A footplate similar to that used by neurosurgeons was machined; however, initial use showed that it too often cut

through the dura. Therefore, our proposed approach was used and typically required 2-3 hrs to complete once skin and muscle were removed. Roughly half of the hemispheres were resected without inducing any detectable damage to the arachnoid and pial vessels. Whenever it was believed that Dremel cutting may have caused subjacent vessel damage, this was noted. Experience showed that such regions could be readily distinguished from impact-induced damage as that caused by dissection exhibited more severe disruption of tissue with minimal hemorrhage. It is unclear whether or not the focal SAH lateral to the oculomotor nerves in ewe XXI (Figure 6.12) was caused by dissection. In this case, damage would not have been caused by the craniotomy, rather, by stretching the oculomotor nerves when extracting the cerebrum from the middle cranial fossa. Damage in this region, or lack thereof, was not carefully investigated in earlier ewes. The second technique developed was an India ink perfusion used to localize potential sources of vessel disruption. While others have used this approach to detect vascular damage in experimental head trauma [176], to our knowledge it is typically employed to document general locations of damage rather than the precise vessel that is the source of the hemorrhage. While it is not critical to the aims of the present work to identify the vessels responsible for bleeding, we believe that identifying such will guide us to the vessels (type, size, etc.) most prone to collagen and elastin damage. The ink perfusion was fruitful in a number of ways. First, perfusion through the MCA generally spread through both the arterial and venous systems on the brain surface, likely due to arteriovenous shunts. Second, whenever the ink perfusion successfully reached a region with SAH, it also leaked out of the vasculature, suggesting positive detection of vessel damage. Obviously, the sooner the leak was detected the better it localized the disruption.

Detection was easiest when SAH was located on a gyrus and most difficult in a sulcus. In the best cases, the source of a leak could be pinpointed to a region a few hundred microns in diameter. However, these typically identified regions dense with veins too small to dissect. Therefore, the belief that veins were the source of the hemorrhage could never be shown definitively. It is unclear whether these findings suggest that veins are more susceptible to rupture than arteries or that our model simply generates high strains in regions that happen to be highly vascularized with pial veins. Finally, we never observed ink to leak in a region that wasn't previously documented to have SAH, suggesting that manual perfusion never caused spontaneous damage. In addition to the previously noted challenge of localizing the precise source of the leak, especially in sulci, the primary limitation of ink perfusion is that it can only successfully identify leaks in one or two regions. Once ink reaches a leak, this serves as a low resistance drain which generally inhibits further perfusion. This limitation is exacerbated by the fact that dissection-induced damage is likely to occur somewhere along the vasculature. This very challenge prevented complete perfusion of the right hemisphere in ewe XXI.

6.5.3 Limitations and future work

One of the limitations of our approach to detecting vascular damage *in vivo* is that preliminary *in vitro* investigations on stretch-induced microstructural damage were conducted at quasi-static rates and on only one size of cerebral artery. Vessel loading rates in head impact are not known; however, brain tissue strain rates have been estimated to range from 10 to 100 s^{-1} in conventional TBI [17, 18, 79, 80]. We have previously shown strain rate to have little significance on the mechanical, including

failure, properties of human cerebral arteries and veins over four orders of magnitude (0.01 to 500 s^{-1}; [23]). While little is known about rate effects in subfailure damage, the literature does suggest it plays a role. Stemper et al. found the strain at intimal disruption to decrease with increasing loading rates in aortic segments [39]. In addition, a recent study showed molecular-level collagen damage to decrease at higher frequency loading of tendon fascicles [92]. Therefore, we recommend that future work should explore both collagen damage (via CHP) and elastin damage (via imaging of IEL failure) at strain rates above 100 s^{-1}. Furthermore, as our preliminary studies only investigated damage in middle cerebral arteries, subfailure damage should also be investigated in smaller pial arteries, veins, and branchpoints.

In addition to better understanding subfailure damage at high strain rates and in cerebral vessels other than the MCA, eventual detection of collagen and/or elastin damage in the vessel wall will require at least one of two things to occur: further increasing the severity of vascular trauma induced by the model or improving detection of structural damage in smaller vessels. Given that neither collagen nor elastin failure was detected in our investigations thus far, it is suggested that efforts should be made to advance both aspects of the study. Granted, hemorrhage following a closed-head impact was only successfully achieved in two animals and investigations of microstructural damage are still limited. However, for results to be meaningful, microstructural damage will not just have to be found in a few vessels, but damage must be shown to be significantly greater than that incident to dissection.

6.5.3.1 Increasing the severity of vascular damage

While our findings were comparable to those reported by previous investigators, it is not unreasonable to think that the severity of vascular damage can be further increased in the model. A few of the prior studies showed more diffuse SAH in the temporal lobe [24], trauma in all regions of the brain [175], and head accelerations up to 50% greater than that achieved in the present work [174]. Furthermore, we have no reason to believe that efforts were ever made by previous groups to optimize this aspect of the model. The current method for loading the head is far from a rigid impact. Prior to reaching the skull, force from the impactor passes through a 6 mm thick piece of porous rubber, the skin and shaved wool, and the several millimeters thick muscle on the temporal fossa. Efforts should be made to explore loading the head more directly, which would likely require use of an impact plate that diffuses the impact force over a broader area. Lewis et al. made an incision so that a "contoured" impact plate could be placed below the skin [24]. Two others restrained the impactor to prevent recoil, which should also increase the energy transferred [25, 174]. Such modifications were never attempted in the present work. Methods outside of explosive-driven stunners could also be explored. For example, Jarvis Products Crop makes a pneumatic driven stunner that claims to be stronger than the CASH Magnum used in this study. However, these devices are also much more expensive.

6.5.3.2 Improving detection of structural damage in small vessels

While increasing the severity of the head injury is helpful, it is likely an incremental improvement compared to facilitating detection of damage in small vessels.

Arteries greater than 250 μm in diameter were routinely dissected in our studies, with the smallest being around 150 μm. As veins can be more rigidly attached to the pia-arachnoid, and have thinner walls, the smallest veins dissected were around 300-400 μm in diameter. In many cases, the arachnoid was even left attached to veins as removal of it could cause damage. Detecting structural damage in smaller vessels essentially scales the amount of vasculature to be explored nonlinearly and increases the likelihood of identifying damage. However, such a scaling may also make it unreasonable to physically remove so many vessels. Therefore, the best approach would not only enable study of smaller vessels yet damage detection without having to remove the vessels from the brain, saving both time and avoiding dissection-induced damage. This could potentially be done with fluorescent labeled platelets [177, 178] that can later be imaged without removal of the vessels.

As hemorrhage was only recently achieved in the model, future work could also seek to improve the repeatability and characterization of the model. A few modifications by other investigators worth exploring are attachment of an accelerometer array to fully characterize the motion of the head [174] and integration of an in-line force transducer to quantify impact forces [25, 174].

6.6 Conclusion

In summary, preliminary investigations were carried out to detect structural damage to the cerebrovascular EMC in an ovine closed-head injury model. The initial goal of the study was to induce cortical hemorrhage in the absence of skull fracture. This was successfully achieved by a left temporal blow with a captive bolt stunner through a

padded steel impact plate. Subarachnoid hemorrhage and leaks during India ink perfusion identified regions likely to have incurred high vascular strains. Cortical arteries and veins greater than 150 and 300 μm in diameter, respectively, were dissected from these regions and stained with a marker of collagen damage. Fluorescence microscopy of samples from two ewes did not detect collagen damage or disruption of the internal elastic lamina. Recommendations are made for increasing the severity of loading and sensitivity of damage detection to better determine the contribution of the cerebrovascular ECM damage in head injury.

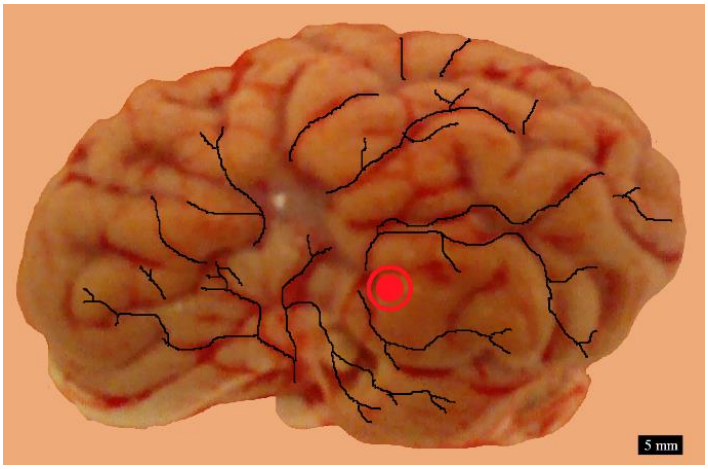

Figure 6.1: Left hemisphere of ewe brain with MCA distribution (>250 um) traced in black. Impact site provided for reference (red circle). Scale bar is 5 mm.

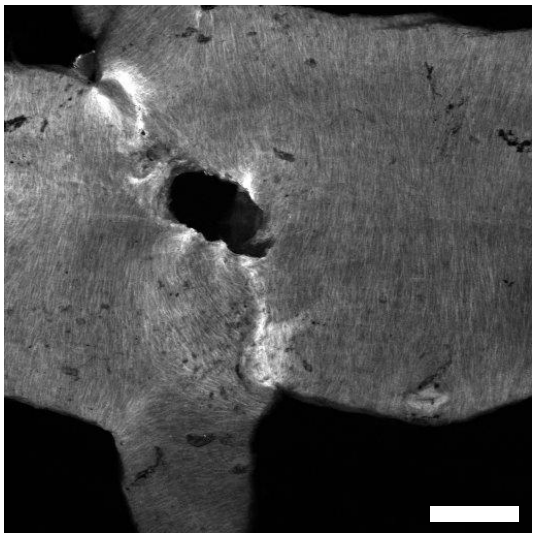

Figure 6.2: Confocal image showing partial transection of the arterial wall at a branchpoint taken from ewe X. Branchpoint has been cut open and laid flat for imaging with a 488 nm laser. Disrupted wall is manifest as a hole (dark region) at the center of the image which passes through the entire arterial wall. However, as hemorrhage was not observed in the MRI scan, disruption may have been caused during dissection. While the confocal laser used for this image also excites the CHP signal, we were unable to draw any conclusive results regarding collagen damage as enhanced signal may have been confounded with folds in tissue at branch junction. Scale bar is 200 μm.

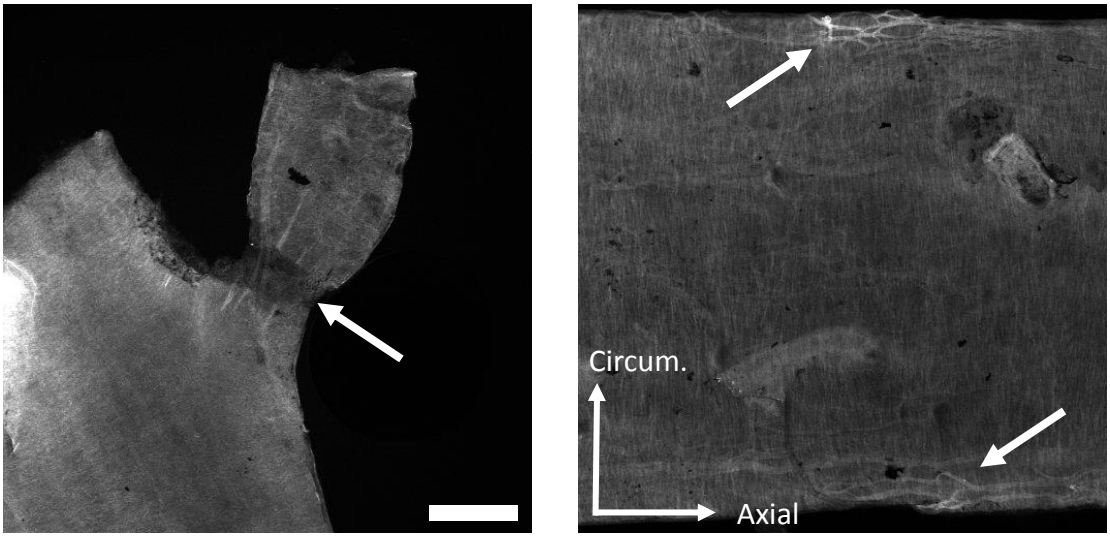

Figure 6.3: Confocal images showing intimal failure at an arterial branch (left) and mild CHP staining along the length of an artery (right) from ewe X. Left image was collected with the 405 nm laser which best images elastin structures in the vascular wall without exciting the CHP fluorophore. Right image was collected with the 488 nm laser which best images the CHP signal. Note that these levels of damage would not result in cerebral hemorrhage. Scale bar (200 μm) applies to both images.

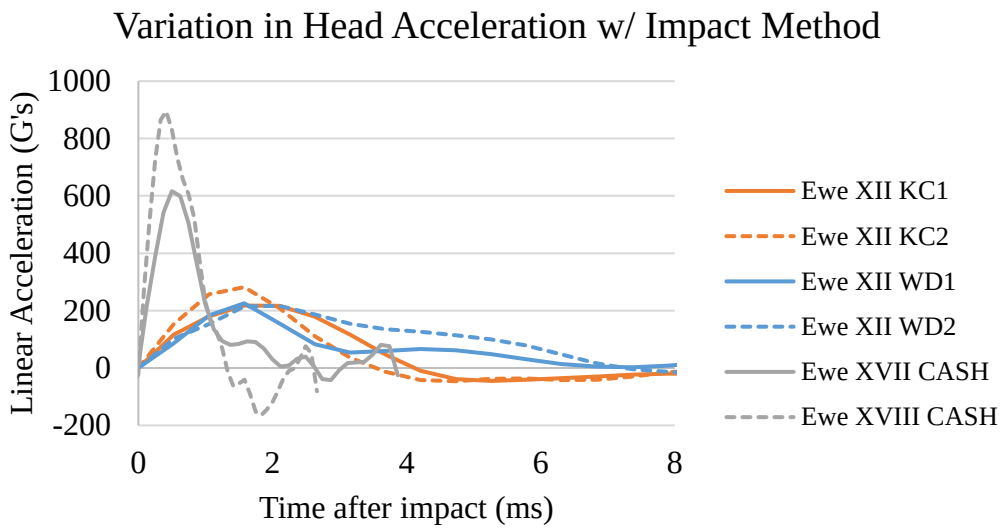

Figure 6.4: Comparison of head accelerations in postmortem ewes using the most severe loading for all three impact methods (KC: KC stunner, C-5 Red charge; WD: weight drop, 1.65 m; CASH: CASH Magnum stunner, Red charge). The weight drop approach failed to produce higher accelerations than the KC stunner. Further development with the CASH Magnum Concussion stunner resulted in head accelerations more than double that produced with the two other approaches.

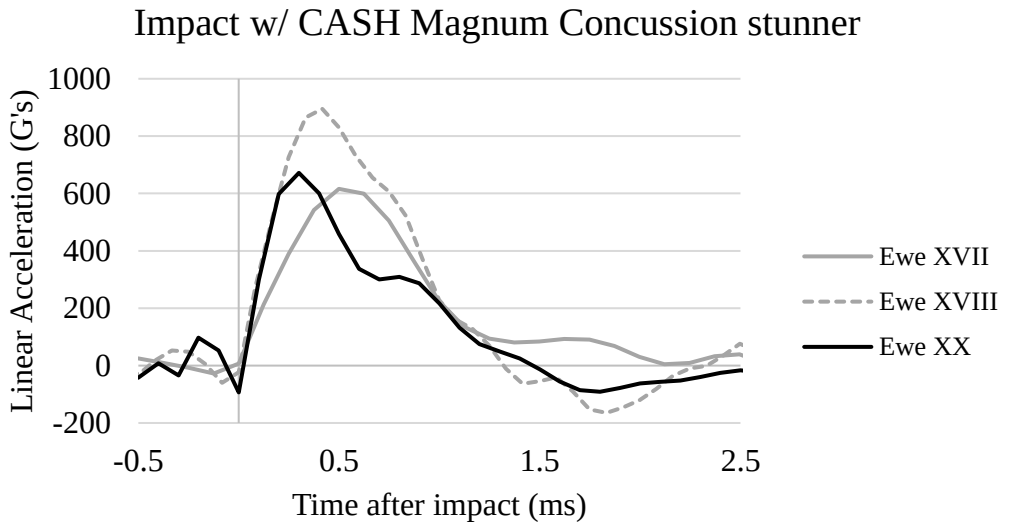

Figure 6.5: Head acceleration from *in vivo* impact of ewe XX (black) compared to same loading in postmortem ewes XVII and XVIII (previously presented in Figure 6.4). Loadings were comparable and produced peak head accelerations between 616-895 G's.

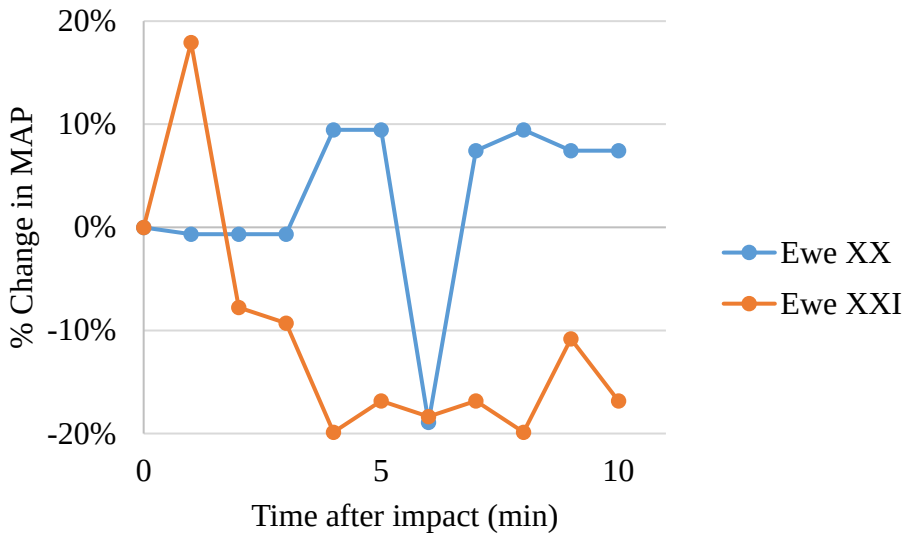

Figure 6.6: Mean arterial pressure (MAP) as a function of time after impact for ewes XX and XXI. Blood pressure in ewe XX showed a slight increase 3 min after impact. Ewe XXI showed an initial increase in the first minute but then readings stabilized around 15-20% below baseline.

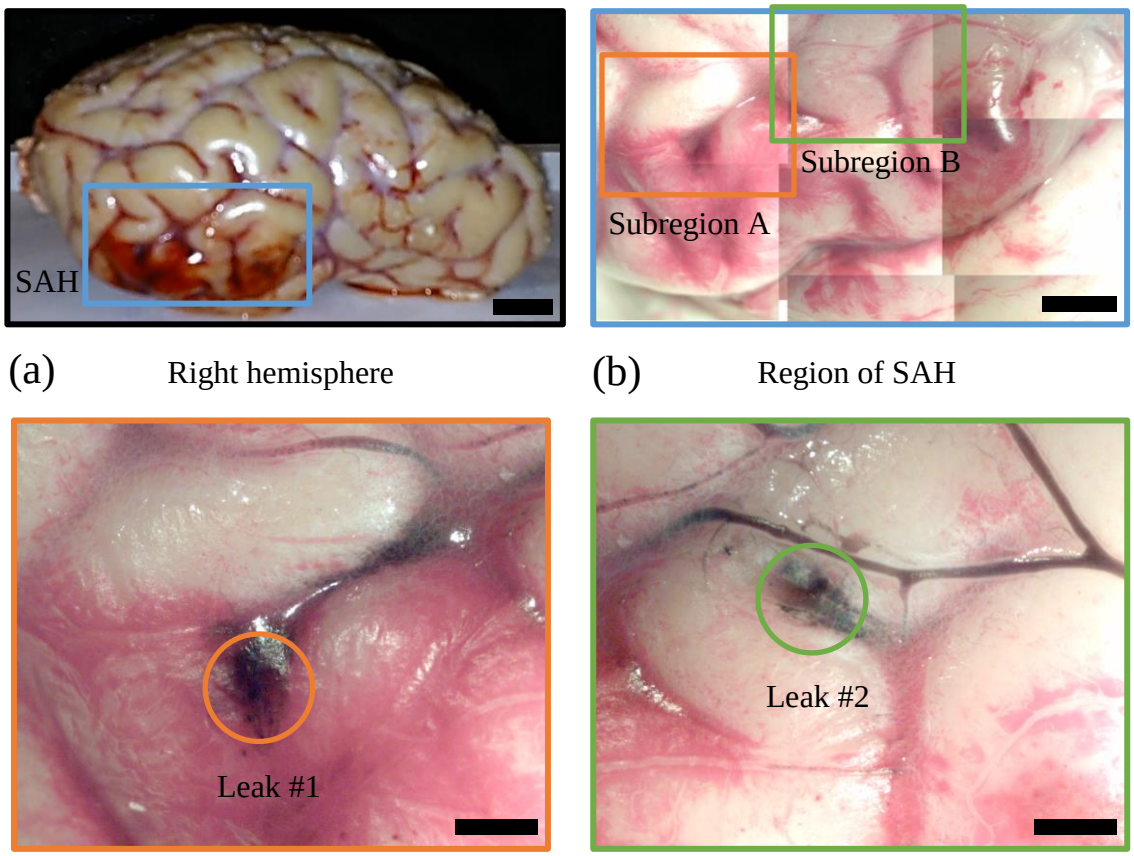

(a) Right hemisphere (b) Region of SAH

(c) Subregion A w/ ink perfusion (d) Subregion B w/ ink perfusion

Figure 6.7: Vascular damage in the right hemisphere of ewe XX. (a) Contrecoup, diffuse subarchanoid hemorrhage was found in the the temporal cortex. (b) Higher magnification image of region of SAH from (a). Subregions A (c) and B (d) from (b) showing two leaks observed observed during India ink perfusion. Scale bars (a): 10 mm, (b): 5 mm, (c) and (d): 2 mm.

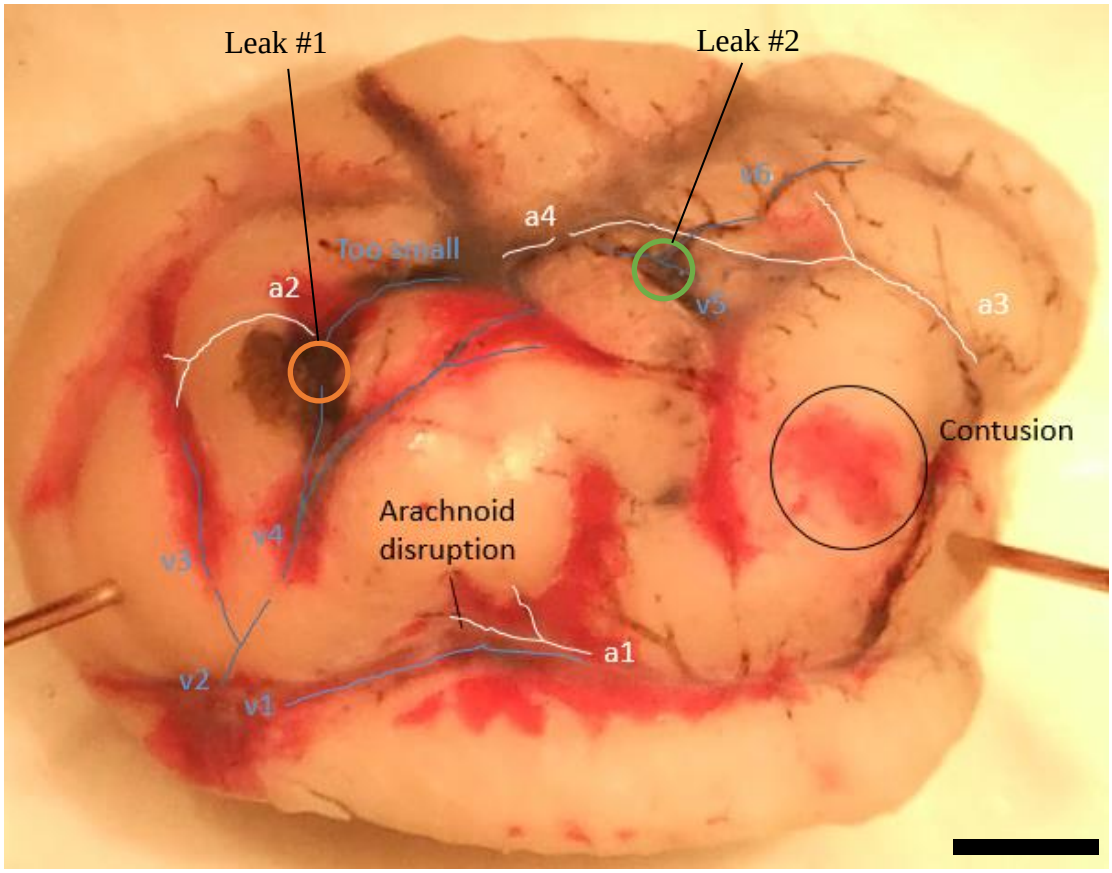

Figure 6.8: Region of SAH from right hemisphere w/ largest neighboring arteries (white) and veins (blue). Arteries are labeled ‘a#’ and veins ‘v#’ if they were dissected. India ink leaks, arachnoid disruption, and contusion are also identified. Scale bar is 5 mm.

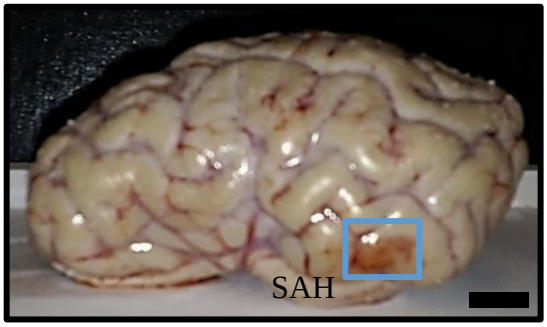

(a) Left Hemisphere

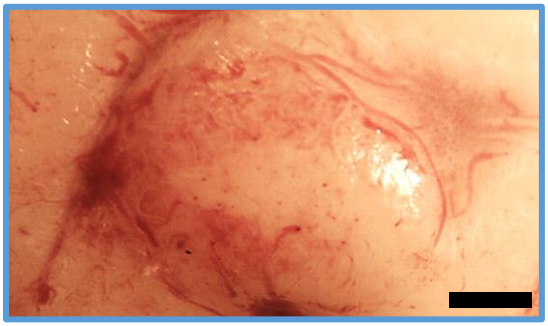

(b) Region of SAH

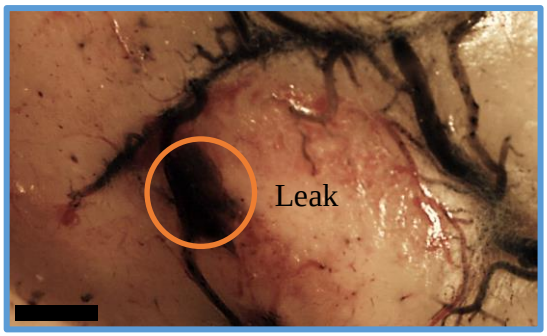

(c) Region of SAH w/ ink perfusion

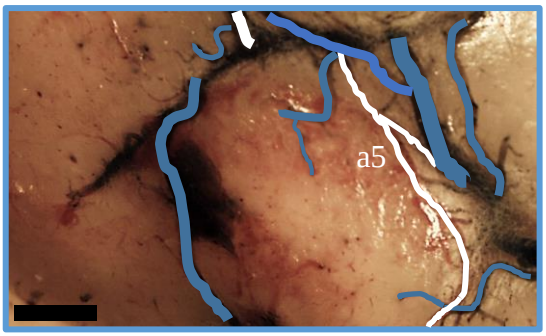

(d) Region of SAH w/ largest arteries (white) and veins (blue)

Figure 6.9: Vascular damage in the left hemisphere of ewe XX. (a) Coup subarchanoid hemorrhage was found in the the temporal cortex. (b) Higher magnification image of region of SAH from (a). (c) Region from (b) with slightly different orientation showing leak identified during Ink ink perfusion. (d) Image from (c) with largest neighboring arteries (white) and veins (blue). Only one artery, “a5”, was dissected as veins proximal to the leak and hemorrhage were too small to dissect. Scale bars (a): 10 mm, (b), (c), and (d): 2 mm.

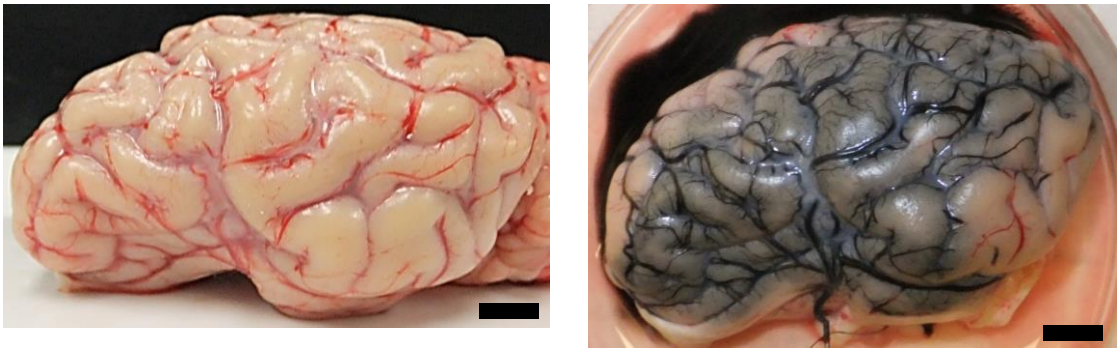

Figure 6.10: Left hemisphere of ewe XXI. Neither hemorrhage (left) nor India ink leaks (right) were found. The perfused region was carefully examined for leaks underneath a light microscope at 1-2x magnification. Scale bars = 10 mm.

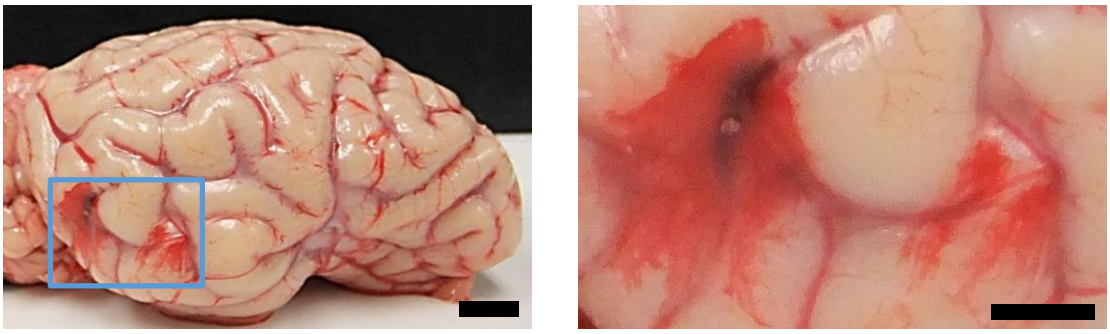

Figure 6.11: Right hemisphere of ewe XXI. Subarachnoid hemorrhage was found in two regions of the temporal cortex (boxed, left; magnified, right). Subsequent India ink perfusion failed to detect sources of leaks. Scale bars: 10 mm (left), 5 mm (right).

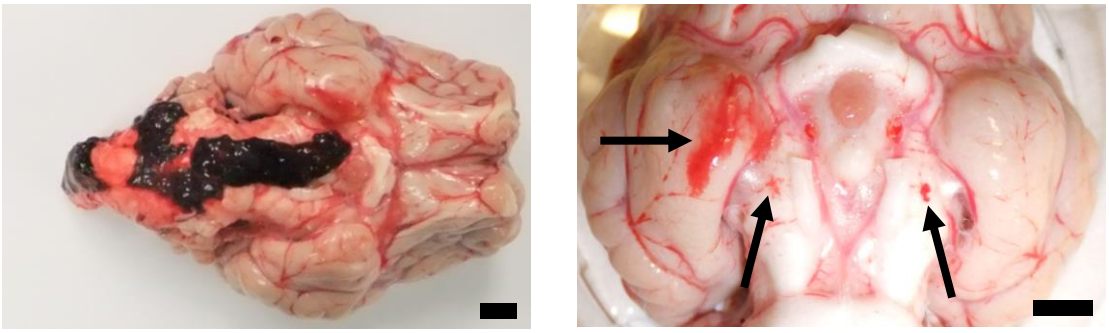

Figure 6.12: Ventral surface of ewe XXI. Coagulated subdural blood separated from the brain during resection, though was replaced in approximate location for imaging (left). Subarachnoid hemorrhage was also found subjacent to the subdural hemorrhage. Symmetric, focal SAH was found lateral to the oculomotor nerves and on the ventral surface of the right piriform cortex (arrows). Scale bars = 10 mm.

Table 6.1: Summary of impact studies on all 21 ewes showing the impact method used (KC: KC stunner; WD: weight drop; CASH: CASH Magnum Concussion stunner), the explosive charge (color) or drop height used; the location of the impact, the duration that the ewe was survived postimpact (N/A: postmortem impact), the location of skull fracture and hemorrhage (L: left hemisphere; R: right hemisphere; Stem: brain stem; Par: parietal cortex; Temp: temporal cortex; Piri: piriform cortex), and the type of hemorrhage (SAH: subarachnoid hemorrhage; SDH: subdural hemorrhage; dash signifies that the brain was never removed). Cortical hemorrhage in the absence of skull fracture was not achieved with the first impact method (KC stunner, ewes I-X) or with the second (weight drop, ewes XI-XII), but was achieved with the third (CASH Magnum stunner, ewes XX and XXI).

Ewe	Impact method	Charge / Drop (m)	Location	Survival (min)	Skull fracture	Hemorrhage
I	KC	Yellow	Temp	<10	None	None
II	KC	Blue	Temp	<10	None	None
III	KC	Blue	Temp	<10	None	Stem SAH
IV	KC	Red	Par	<10	L Par	L Par SAH/SDH
V	KC	Red	Par	<10	None	None
VI	KC	Red	Par	<10	L Par	L Par SAH/SDH
VII	KC	Red	Par	<10	L Par	L Par SAH/SDH
VIII	KC	Red	Temp	<10	None	None
IX	KC	Red	Temp	<10	None	None
X	KC	Red	Temp	255	None	None
XI	KC, WD	Red 1.1, 1.4, 1.7	Temp	N/A	None	None
XII	KC, WD	Red (2x) 1.65 (3x)	Temp	N/A	None	None
XIII	CASH	Orange, Black, Green	Temp	N/A	Yes	-
XIV	CASH	Orange	Temp	N/A	Yes	-
XV	CASH	Red	Temp	N/A	Yes	-
XVI	CASH	Orange, Red	Temp	N/A	Yes	-
XVII	CASH	Orange, Green, Red	Temp	N/A	None	-
XVIII	CASH	Red	Temp	N/A	None	-
XIX	CASH	Red	Temp	N/A	None	-
XX	CASH	Red	Temp	60	None	L Temp SAH; R Temp SAH
XXI	CASH	Red	Temp	15	None	L Temp SAH; R Temp SAH; R Piri; Stem SAH/SDH

CHAPTER 7

CONCLUSION

This dissertation characterizes stretch-induced damage to the cerebrovascular ECM and seeks similar damage in a closed-head injury model. Investigations are broken down into three *in vitro* studies (Chapters 3-5) and their results serve to guide and interpret an *in vivo* investigation of cerebrovascular damage (Chapter 6). The first study (Chapter 3) characterizes the effect of a single subfailure axial overstretch on the mechanical properties of cerebral arteries while the second and third studies explore the effect on vessel microstructure. This includes defining relationships between overstretch magnitude and injury to the various structural components of the vessel wall, including the collagen (Chapter 4) and elastin (Chapter 5) microstructures responsible for vessel integrity. Findings from these studies are then used to identify and describe blood vessel damage in a preliminary large animal model of TBI (Chapter 6). The animal model seeks to clarify the distribution of vessel damage over the cortical surface and identify vessel types most susceptible to injury. The key findings from these four studies are summarized by chapter herein.

7.1 Synopsis of Chapter 3: biaxial softening

1) A single axial overstretch increases both the axial and circumferential compliance of sheep middle cerebral arteries. Softening is manifest as a decrease in stiffness and strain energy as well as an increase in vessel diameter and length. Axial and circumferential changes are statistically significant following a 20 and 40% overstretch beyond the *in vivo* configuration, respectively. These passive changes would lead to a decrease in vascular resistance and likely play a role in previous reports of stretch-induced cellular dysfunction.
2) A microstructurally-motivated constitutive damage model appropriately captured the biaxial nature of arterial softening; however, it was unable to properly model the magnitude of these changes across all levels of overstretch. It is unclear to whether model discrepancies are due to experimental methods or limitations of the model itself.

7.2 Synopsis of Chapter 4: collagen damage

1) Arterial overstretch induces molecular-level unfolding of collagen. Results provide the first identification of such damage in vasculature tissue. The damage can be effectively detected, localized, and quantified with a collagen hybridizing peptide. This tool can potentially be used to study damage propagation across physical scales and arterial damage in vascular trauma.
2) Stretch-induced damage occurs primarily in fibers aligned with the direction of loading, increases with overstretch severity, and initiates just after the

vessel reaches maximum stiffness. These findings can be used to develop microstructurally-based constitutive models of arterial damage.

7.3 Synopsis of Chapter 5: elastin/endothelial failure

1) Cerebral arteries experience partial disruption of the inner wall prior to catastrophic failure, with most occurring between the stretch at maximum stiffness and the stretch at ultimate stress. The threshold of failure does not change across four stages of ovine development (fetal, newborn, juvenile, adult).
2) Inner wall disruption includes rupture of the internal elastic lamina and endothelium, demonstrating that cerebral arteries can be damaged significantly in the absence of hemorrhage. Such damage, if found *in vivo*, could play a role in the elevated risk of stroke post-TBI.

7.4 Synopsis of Chapter 6: closed-head injury model

1) Cortical hemorrhage can be induced in sheep without inducing skull fracture though a temporal blow with a captive bolt stunner. Loading results in coup and contrecoup contusion, typical of human injury.
2) A craniotomy can be performed without damaging the arachnoid or surface vessels, thus enabling study of impact-induced damage to cortical vessels *ex vivo*.
3) Following closed-head impact, neither collagen nor elastin damage was found in intact blood vessels near the region of hemorrhage, suggesting that vessel

damage is focal. However, investigations are still preliminary as damage was only investigated in arteries and veins greater than 150 um and 300 μm in diameter, respectively, in two sheep.

7.5 Future work

1) In order to develop a better constitutive model of cerebral artery softening, the degree to which repeated loading introduces continuous softening should first be understood. If continuous softening is negligible, then the evolution of damage can be characterized through repeated loading of individual vessels as done by Weisbecker et al. [60]. If continuous softening cannot be neglected, then either existing phenomenological frameworks could be employed [179, 180] or a new microstructurally-motivated model could be developed to incorporate continuous softening and residual strains. Some biaxial characterizations should be conducted at subphysiological pressures in order to better capture the nonlinearity of vessel mechanics.
2) As the present work only loaded isolated vessels quasi-statically, the effect of high rate deformations on mechanical softening and microstructural damage should be explored. Findings, particularly those regarding thresholds of IEL failure and molecular-level unfolding of collagen (detected with CHP) would be particularly meaningful for future investigations of *in vivo* head trauma. Similar studies could also be extended to include tests on small arteries (less than 500 μm in diameter), veins, and branchpoints.
3) Local fiducial markers (microspheres placed on the adventitia) did not always

provide reliable strain measurements, especially when approaching failure. Methods for improved tracking of local strains in light and fluorescence microscopy would be beneficial, especially approaches that can capture layer-specific strains in an intact wall.

4) Now that CHP has been demonstrated as an effective tool for detecting stretch-induced collagen damage in arteries, ways of exploiting this technique to benefit other areas of arterial biomechanics should be explored. Blunt cerebrovascular injury, angioplasty, and aneurysm failure are three potential applications.
5) Due to the focal nature of vascular disruption in our model of closed-head injury, eventual detection of microstructural damage will require either further increasing the severity of trauma or improving detection of damage in smaller vessels. It is recommended that both approaches be explored. Suggestions on how this might be done are outlined in Section 7.5. Alternative injury models such as controlled cortical impact could also be pursued to aid in understanding of how to best detect damage *in vivo*. Once damage is detected, models can be adapted to track injury progression over time.

APPENDIX A

SUMMARY OF EXPERIMENTAL RESULTS (CH. 4)

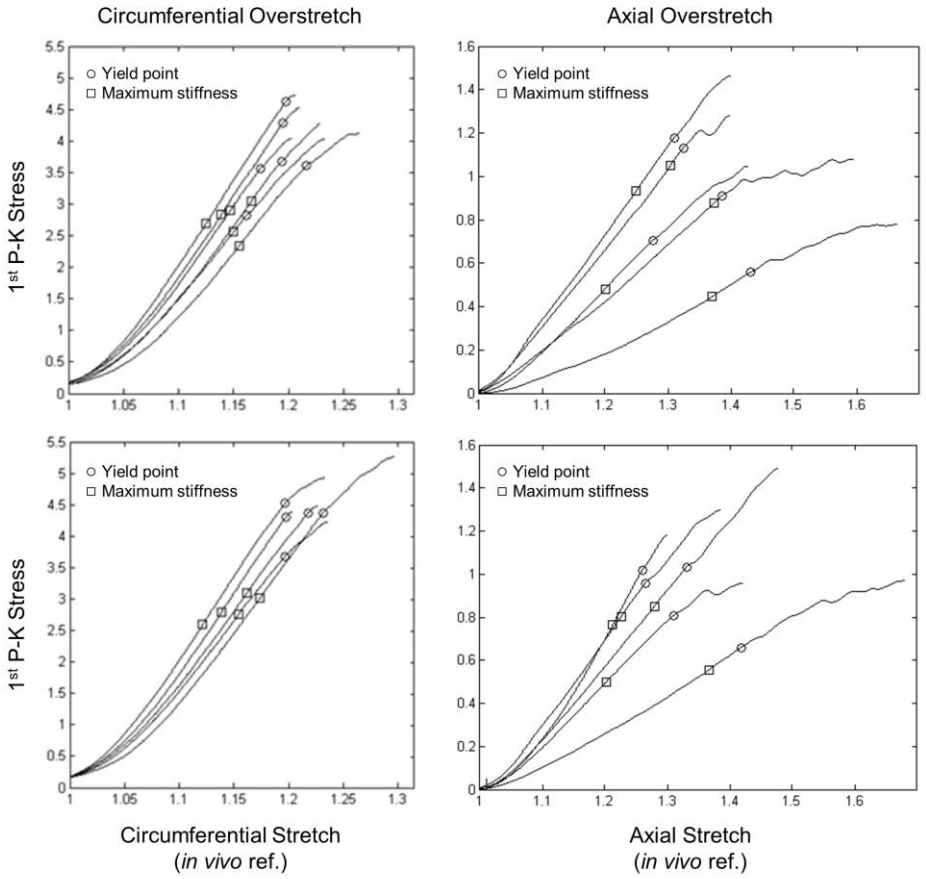

Figure A.1: Identified yield points and points of maximum stiffness. Stress-stretch curves for cases of both circumferential (left panel, n=11) and axial (right panel, n=10) loading are shown. Data are only presented for samples that had an identified yield point (circle), and curves for each loading direction are divided up into two plots for clarity. The point of maximum stiffness is also identified (square). In nearly all axial samples, the calculated yield point fell on a distinct bend or elbow and was often followed by significant undulations. Most of the yield points on circumferential samples also fell on an elbow in the curve; however, changes in slope were more subtle and failure occurred soon after.

Table A.1: Summary of results for all 28 arterial rings loaded circumferentially. The table provides the vessel segment from which each ring was taken (Segment 1: 'C1', Segment 2: 'C2', etc.), the loading group, the ring outer diameter at the pressurized *in vivo* configuration, the maximum circumferential overstretch, the stretch at maximum stiffness (only calculated for samples that yielded, with "N/A" signifying that the sample did not yield), the yield stretch, the ultimate stretch (only calculated for samples pulled to failure), the amount of medial damage (percentage of pixels above the control-specific intensity threshold), the dominant orientation of damaged fibers (relative to the circumferential direction), and the coherency of the damaged fiber orientation (1=highly oriented; 0=isotropic). Measures of damaged fiber anisotropy (Orientation and Coherency) were only calculated for samples having > 0.06% damage (value taken from the circumferential control sample with the greatest % damage, C2-3). All stretch values are relative to the *in vivo* configuration. As stated in Section 4.3.6, '% damage' was quantified by calculating the percentage of pixels having an intensity greater than 2x the average intensity of the corresponding control. For example, the medial image of control ring C2-3 had an average intensity of 859 on a 12-bit scale. Therefore, for rings C2-1 through C2-4 pixels were only quantified as 'damage' if they had an intensity greater than 2*859 = 1718. In the case that there was sufficient tissue to collect more than one control for a given vessel segment (i.e., segment C4 has control rings C4-3 and C4-7), then the two 'average intensity' values were averaged prior to scaling by 2.

Ring Label	Stretch Group	Diam. (mm)	Circum. Overstretch	Stretch at Max Stiff.	Yield Stretch	Ult. Stretch	Medial Damage (%)	Orientation (deg)	Coherency
C4-3	control	1.49	1.00	N/A	N/A	N/A	6.8E-03	N/A	N/A
C2-3	control	1.45	1.01	N/A	N/A	N/A	0.06	N/A	N/A
C4-7	control	1.38	1.01	N/A	N/A	N/A	4.0E-03	N/A	N/A
C5-2	control	1.51	1.01	N/A	N/A	N/A	3.1E-03	N/A	N/A
C1-7	control	1.66	1.01	N/A	N/A	N/A	1.9E-03	N/A	N/A
C1-3	control	1.70	1.01	N/A	N/A	N/A	3.8E-03	N/A	N/A
C3-3	control	1.50	1.01	N/A	N/A	N/A	1.9E-03	N/A	N/A
C1-2	subfail	1.64	1.09	N/A	N/A	N/A	7.5E-03	N/A	N/A
C5-1	subfail	1.49	1.15	N/A	N/A	N/A	6.3E-04	N/A	N/A
C1-6	subfail	1.63	1.15	N/A	N/A	N/A	1.9E-03	N/A	N/A
C5-4	subfail	1.56	1.17	N/A	N/A	N/A	4.7E-04	N/A	N/A
C4-5	subfail	1.45	1.18	N/A	N/A	N/A	0.82	-3.3	0.27
C4-9	subfail	1.37	1.18	N/A	N/A	N/A	0.71	8.9	0.24
C3-2	subfail	1.50	1.19	N/A	N/A	N/A	0.17	-12.3	0.23
C4-6	subfail	1.39	1.19	N/A	N/A	N/A	0.06	-4.8	0.22
C1-5	subfail	1.57	1.19	N/A	N/A	N/A	0.07	1.3	0.19
C2-4	subfail	1.46	1.19	N/A	N/A	N/A	2.3	-5.9	0.35
C4-1	failure	1.46	1.20	1.15	1.19	1.20	0.74	-16.3	0.40
C4-2	failure	1.46	1.20	1.15	1.19	1.20	0.06	N/A	N/A
C4-8	failure	1.39	1.21	1.13	1.20	1.21	4.5	-2.3	0.24
C4-4	failure	1.49	1.21	1.15	1.20	1.21	0.42	4.9	0.27
C1-4	failure	1.61	1.23	1.15	1.22	1.23	3.2	-0.2	0.32
C5-3	failure	1.55	1.23	1.15	1.20	1.23	1.6	-6.1	0.27
C2-1	failure	1.43	1.23	1.14	1.21	1.23	7.1	-4.4	0.28
C5-5	failure	1.58	1.23	1.15	1.20	1.23	4.7	1.2	0.18
C2-2	failure	1.47	1.23	1.14	1.20	1.24	4.6	-7.3	0.32
C1-8	failure	1.67	1.26	1.16	1.21	1.26	3.4	-3.1	0.32
C1-1	failure	1.61	1.30	1.17	1.23	1.30	5.9	-0.4	0.30
mean		1.52		1.15	1.20	1.23		-3.1	0.27
SD		0.09		0.01	0.01	0.03		6.0	0.06

Table A.2: Summary of results for all 21 arterial segments loaded axially. The table provides brain from which each segment was taken (Brain 1: 'A1', Brain 2: 'A2', etc.), the loading group, the segment *in vivo* length, the maximum axial overstretch, the stretch at maximum stiffness (only calculated for samples that yielded, with "N/A" signifying that the sample did not yield, the yield stretch, the ultimate stretch (only calculated for samples pulled to failure), the amount of adventitial damage (percentage of pixels above the control-specific intensity threshold), the dominant orientation of damaged fibers (relative to the circumferential direction), and the coherency of the damaged fiber orientation (1=highly oriented; 0=isotropic). Measures of damaged fiber anisotropy (Orientation and Coherency) were only calculated for samples having > 1.4% damage (value taken from the axial control sample with the greatest % damage, A1-1). Force data for sample A1-2 were accidentally overwritten during testing and, therefore, certain stretch measurements are not reported. All stretch values are relative to the *in vivo* configuration. As stated in Section 4.3.6, '% damage' was quantified by calculating the percentage of pixels having an intensity greater than 2x the average intensity of the corresponding control. For example, the adventitial image of control segment A5-1 had an average intensity of 543 on a 12-bit scale. Therefore, for segments A5-1 through A5-4 pixels were only quantified as 'damage' if they had an intensity greater than 2*543 = 1086. In the case that there was sufficient tissue to collect more than one control for a given brain (i.e., brain A4 has control segments A4-2 and A4-5), then the 'average intensity' values were averaged prior to scaling by 2.

Segment Label	Stretch Group	Reference Length (mm)	Axial Overstretch	Stretch at Max Stiff.	Yield Stretch	Ult. Stretch	Adventitial Damage (%)	Orientation (deg)	Coherency
A1-1	control	3.21	1.05	N/A	N/A	N/A	1.4	N/A	N/A
A2-2	control	4.47	1.05	N/A	N/A	N/A	2.9E-02	N/A	N/A
A3-4	control	5.38	1.05	N/A	N/A	N/A	0.09	N/A	N/A
A4-2	control	5.50	1.05	N/A	N/A	N/A	0.46	N/A	N/A
A4-5	control	5.07	1.05	N/A	N/A	N/A	0.22	N/A	N/A
A5-1	control	4.27	1.05	N/A	N/A	N/A	0.11	N/A	N/A
A4-1	subfail	5.55	1.20	N/A	N/A	N/A	1.5E-02	N/A	N/A
A4-6	subfail	4.84	1.20	N/A	N/A	N/A	4.4E-02	N/A	N/A
A2-1	subfail	5.70	1.30	1.21	1.26	N/A	0.43	N/A	N/A
A4-4	subfail	4.74	1.38	1.23	1.26	N/A	12.7	85.8	0.21
A5-4	subfail	3.49	1.38	N/A	N/A	N/A	0.91	N/A	N/A
A2-3	subfail	4.21	1.40	1.30	1.32	N/A	0.23	N/A	N/A
A3-3	subfail	5.26	1.40	1.25	1.31	N/A	3.3	70.3	0.26
A5-2	subfail	4.57	1.40	N/A	N/A	N/A	0.85	N/A	N/A
A4-3	subfail	4.45	1.42	1.20	1.31	N/A	7.3	79.5	0.12
A5-3	subfail	4.56	1.46	1.20	1.28	N/A	1.2	N/A	N/A
A2-4	subfail	4.08	1.63	1.28	1.33	N/A	10.2	-80.4	0.24
A1-3	failure	5.53	1.67	1.37	1.39	1.59	21.0	-86.1	0.19
A3-2	failure	6.35	1.69	1.37	1.42	1.68	30.7	83.9	0.27
A3-1	failure	5.50	1.69	1.37	1.43	1.66	15.1	86.3	0.22
A1-2	failure	3.65	1.88	-	-	-	39.3	-83.8	0.14
mean		4.78		1.28	1.33	1.65		86.9	0.20
SD		0.81		0.07	0.06	0.0		9.6	0.05

APPENDIX B

THE EFFECT OF VARYING THE PIXEL INTENSITY DAMAGE THRESHOLD ON RESULTS (CH. 4)

The values reported for the collagen damage parameters (λ_C and m, Table 4.1) are a function of the control-specific intensity threshold used. In order to distinguish CHP binding of mechanically damaged collagen from that of remodeling collagen, a control-specific intensity threshold was applied to all confocal images. Pixels with intensities greater than this threshold were classified as mechanically damaged and lower intensity pixels as background signal attributable to collagen remodeling. In early studies, various thresholds were qualitatively evaluated across a range of overstretch levels; however, the threshold utilized (f=2.0 times the average brightness of the corresponding control) was chosen as it qualitatively appeared to minimize false classification of mechanically damaged and remodeling fibers. While f=2.0 seemed most appropriate on average across all samples observed in our preliminary investigation (and was, therefore, the threshold used to report our final results in Table 4.1), f=1.5 and 2.5 were found to be reasonable lower and upper bounds of possible thresholds (Figures B.1 and B.2). As the intensity threshold determines the algorithm's sensitivity and, therefore, ultimately affects the reported collagen damage parameters, data were also reprocessed after completion of the study using intensity thresholds of f=1.5 and 2.5 in order to demonstrate the variability in

the resulting regression parameters (Table B.1). These data demonstrate that the reported stretch threshold for circumferential damage is relatively insensitive to the chosen pixel intensity threshold (λ_C=1.14-1.18) and is somewhat wider for the case of axial loading (λ_C=1.29-1.38). This same behavior can be observed in the tighter confidence intervals reported for the circumferential stretch threshold (Table 4.1). Even considering this variability, as the circumferential (1.20 ± 0.02, mean ± SD) and axial (1.33 ± 0.06) yield stretches span a comparable range, we believe that our primary conclusion of a close association between the yield stretch and the onset of collagen damage still holds. The calculated rate of damage accumulation (m), was found to decrease as 'f' increased, as fewer pixels are classified as damaged. Importantly, though, the threshold of f=2.0 resulted in the strongest R-squared values for both directions of loading – a second confirmation that it was the more ideal intensity threshold for this study.

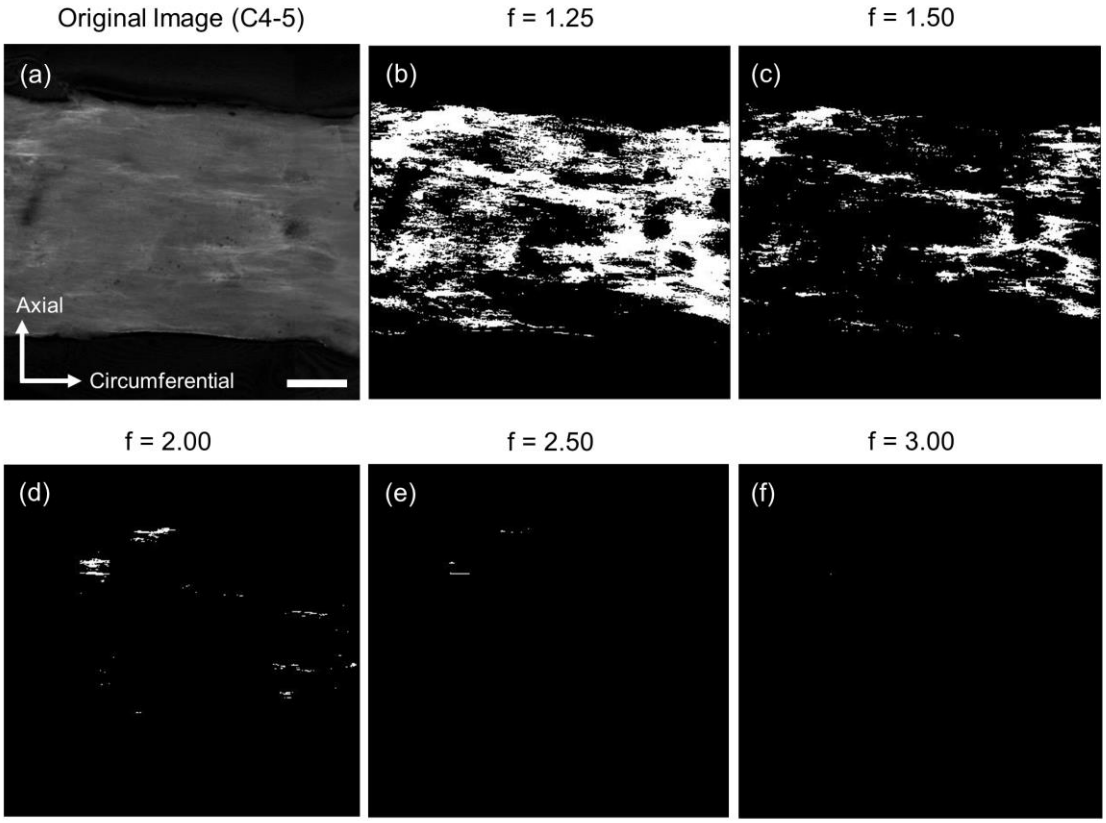

Figure B.1: Effect of varying the pixel-intensity threshold on the measured damage for circumferential loading. a) Confocal image taken within the media of a representative sample (C4-5) loaded circumferentially. The percentage of collagen damage was quantified as the percentage of pixels in the image above a control-specific pixel intensity threshold. The unstretched control sample from the same vessel segment (not shown) had an average pixel intensity of 876 (12-bit scale). Binary images in the remaining panels (b-f) highlight pixels having intensities greater than f*876 for varying values of 'f'. Preliminary qualitative evaluation of several samples across a range of overstretch levels motivated use of f=2.0 for all samples. For this particular sample, it appears that the most appropriate threshold falls between f=1.5 and f=2.0. Scale bar is 200 μm.

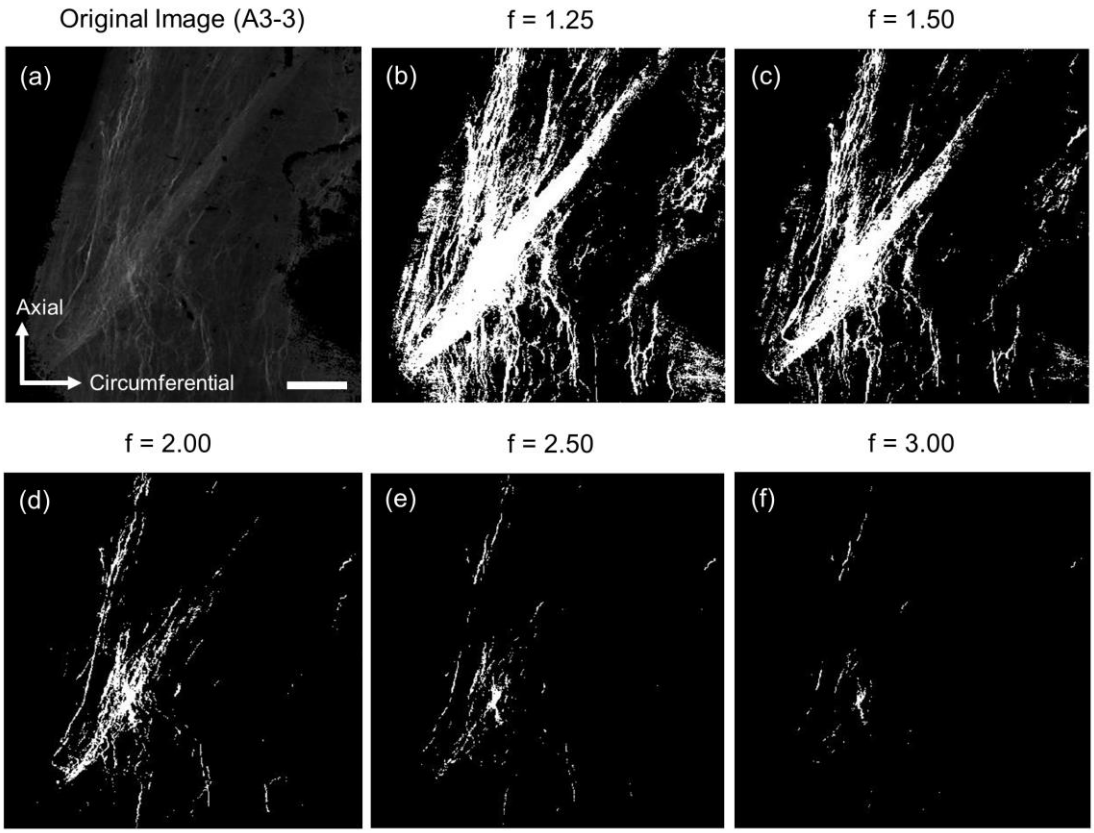

Figure B.2: Effect of varying the pixel-intensity threshold on the measured damage for axial loading. a) Confocal image taken within the adventitia of a representative sample (A3-3) loaded axially. The percentage of collagen damage was quantified as the percentage of pixels in the image above a control-specific pixel intensity threshold. The unstretched control sample from the same sheep brain (not shown) had an average pixel intensity of 479 (12-bit scale). Binary images in the remaining panels (b-f) highlight pixels having intensities greater than f*479 for varying values of 'f'. Preliminary qualitative evaluation of several samples across a range of overstretch levels motivated use of f=2.0 for all samples. For this particular sample, it appears that the most appropriate threshold falls between f=2.0 and f=2.5 as it picks up the fine CHP staining yet ignores the 'background' signal from the lower intensity, large diagonal fibers that were also observed in control samples. Scale bar is 200 μm.

Table B.1: Parameters from the piece-wise linear regression of the damage-stretch data for varying factors, f, above the control-specific intensity thresholds. Previously reported values for f=2.0 (Table 4.1) are included for comparison to the cases of f=1.5 and f=2.5.

Loading Direction	Collagen Damage Threshold (λ_C)			% Damage Per Unit Stretch beyond λ_C (m)			R^2		
	f=1.5	f=2.0	f=2.5	f=1.5	f=2.0	f=2.5	f=1.5	f=2.0	f=2.5
Circum-ferential	1.14	1.17	1.18	177.3	52.8	17.7	0.34	0.55	0.50
Axial	1.29	1.35	1.38	105.7	66.7	35.8	0.75	0.79	0.74

APPENDIX C

MATHEMATIC TRANSFORMATION OF DAMAGED FIBER ANGLES FROM AN UNLOADED STATE TO THE *IN VIVO* CONFIGURATION (CH. 4)

The orientation of damaged fibers was quantified in an unfixed state (on the microscope slide) after overstretch. Therefore, neglecting residual strains, reported angles (Section 4.4.2) best reflect fiber orientations in the unloaded configuration. However, in order to estimate the predamage *in vivo* orientation of these same fibers, additional measurements were made on two failure samples, one from each overstretch direction (axial: A3-1; circumferential: C1-4). Failure samples were used as they have the highest residual strains in the loading direction and, therefore, provide the most extreme case of fibers becoming more diagonal when transformed from the unloaded imaging state to the *in vivo* configuration. Test video and microscopy images were used to calculate the stretch of the vessels in their *in vivo* configuration relative to their postdamage state during imaging under the confocal microscope (unloaded but with some residual strains). These measurements showed that axial sample A3-1 had stretches of $\lambda_Z = 0.94$, $\lambda_C = 1.43$ and circumferential sample C1-4 had stretches of $\lambda_Z = 1.11$, $\lambda_C = 1.22$. Finally, Equation 10 from Wicker et al. [28] was used to transform the previously reported damaged fiber angles in the axial study from 86.9 ± 9.6 (unloaded state with some residual strain) to

85.3 ± 14.3 (*in vivo* configuration) degrees and fiber angles in the circumferential study from -3.1 ± 6.0 to -3.4 ± 6.6. These values show that changes in fiber angles from the *in vivo* configuration to confocal imaging were negligible for samples loaded circumferentially. Fiber angle changes were potentially more pronounced for samples loaded axially as the standard deviation increased from 9.6 to 14.3 degrees. However, given that this distribution is still highly axial, and that this calculation was based on the most extreme case applicable to only half of the samples for which fiber orientations were calculated, we believe that our conclusion still holds, that conclusion being that overstretch primarily damages arterial collagen that is aligned with the direction of loading, with negligible damage to off-axis fibers.

APPENDIX D

JUSTIFICATION FOR THE USE OF NEEDLE STRETCHES IN CHAPTER 4 AND ESTIMATES OF LOCAL STRETCHES (CH. 4)

Despite the application of microspheres on all overstretched samples, the stretches reported in the present work were calculated from a more global measure of needle displacements. The main reason for this was that the correlation between CHP damage and tissue stretch was noisier with microsphere measurements. There are two likely explanations for this. First, some microspheres were observed to move along the surface of the tissue during loading, especially at strains approaching failure. Second, microspheres were only tracked on one side of the tissue, yet CHP damage was quantified around the entire arterial segment. A more ideal approach would be to use local markers to both measure local stretch and to define the boundary for CHP quantification. Unfortunately, too many microspheres were either lost or displaced during the loading and staining process to do so in the present work.

Despite this limitation, an effort was made to estimate local thresholds of tissue damage from global (needle) stretch measurements by applying Equation D.1

$$\lambda_{local} = (\lambda_{needle} - 1)R + 1 \tag{D.1}$$

where R is the average ratio of microsphere strain to needle strain for all non-

control samples (Equation D.2).

$$R = \left(\frac{\lambda_{microsphere} - 1}{\lambda_{needle} - 1} \right)_{avg} \quad \text{(D.2)}$$

The strain ratio, R, was found to be 0.90 ± 0.22 (mean ± SD, n=21) for circumferentially loaded rings and 0.65 ± 0.15 (n=14) for axially loaded segments. Use of an average strain ratio to estimate specific strain measurements was believed to be a reasonable first approximation given that there was no correlation between peak overstretch and the strain ratio at max stretch for either loading group. The fact that both strain ratios are below unity implies that the reported stretch thresholds in Table 4.1 overestimate local stretches. This is due to strain inhomogeneity near the needle attachments, a behavior we have previously described in detail for axial loading [156]. Applying Equation D.1 to the values in Table 4.1 yields more accurate estimates of local damage thresholds (Table D.1). Even with these corrections, though, all of the relative differences between circumferential and axial damage parameters discussed previously still hold true.

It should be emphasized that this limitation regarding the method of strain measurement does not undermine the close association between tissue yielding and the onset of collagen damage as both thresholds, λ_C and λ_Y, scale together (compare Tables 4.1 and D.1). Furthermore, we hypothesize that the structural damage associated with tissue yielding generally occurred within the region where CHP was quantified, as samples pulled to failure most often ruptured between, and not at, needle attachments.

Table D.1: Estimated collagen damage parameters, yield stretches, and stretches at maximum stiffness after accounting for strain inhomogeneities near needle attachments in overstretched samples.

Loading Direction	Stretch at Max Stiffness, λ_{MAX} (mean ± SD)	Yield Stretch, λ_Y (mean ± SD)	Collagen Damage Parameters		
			Damage Threshold, λ_C (95% CI)	% Damage Per Unit Stretch (m) beyond λ_C	R^2
Circumferential	1.14 ± 0.02	1.18 ± 0.02	1.15 (1.13-1.17)	58.7	0.55
Axial	1.18 ± 0.05	1.21 ± 0.04	1.23 (1.19-1.27)	102.8	0.79

REFERENCES

[1] M. Faul, L. Xu, M. Wald, and V. Coronado, "Traumatic brain injury in the United States: Emergency department visits, hospitalizations and deaths 2002–2006," *Atlanta, GA: Centers for Disease Control and Prevention, National Center for Injury Prevention and Control*, 2010.

[2] D. I. Graham, "Neuropathology of head injury," in *Neurotrauma*, R. K. Nrayan, J. E. Wilberger, and J. T. Povlishock, Eds., New York: McGraw-Hill, 1996, pp. 43-59.

[3] D. S. DeWitt and D. S. Prough, "Traumatic cerebral vascular injury: The effects of concussive brain injury on the cerebral vasculature," *Journal of Neurotrauma*, vol. 20, pp. 795-825, 2003.

[4] R. A. Armonda, R. S. Bell, A. H. Vo, G. Ling, T. J. DeGraba, B. Crandall, J. Ecklund, and W. W. Campbell, "Wartime traumatic cerebral vasospasm: Recent review of combat casualties," *Neurosurgery*, vol. 59, pp. 1215-25, Dec 2006.

[5] D. S. DeWitt and D. S. Prough, "Blast-induced brain injury and posttraumatic hypotension and hypoxemia," *Journal of Neurotrauma*, vol. 26, pp. 877-87, Jun 2009.

[6] T. W. Langfitt, W. D. Obrist, T. A. Gennarelli, M. J. O'Connor, and C. A. Ter Weeme, "Correlation of cerebral blood flow with outcome in head injured patients," *Annals of Surgery*, vol. 186, pp. 411-14, 1977.

[7] A. I. Baranova, E. P. Wei, Y. Ueda, M. M. Sholley, H. A. Kontos, and J. T. Povlishock, "Cerebral vascular responsiveness after experimental traumatic brain injury: The beneficial effects of delayed hypothermia combined with superoxide dismutase administration," *Journal of Neurosurgery*, vol. 109, pp. 502-9, 2008.

[8] W. L. Maxwell, A. Irvine, J. H. Adams, D. I. Graham, and T. A. Gennarelli, "Response of cerebral microvasculature to brain injury," *The Journal of Pathology*, vol. 155, pp. 327-35, 1988.

[9] A. Rodríguez-Baeza, F. Reina-de la Torre, A. Poca, M. Martí, and A. Garnacho, "Morphological features in human cortical brain microvessels after head injury: A three-dimensional and immunocytochemical study," *The Anatomical Record Part A: Discoveries in Molecular, Cellular, and Evolutionary Biology*, vol. 273, pp. 583-93, 2003.

[10] P. Dore-Duffy, C. Owen, R. Balabanov, S. Murphy, T. Beaumont, and J. A. Rafols, "Pericyte migration from the vascular wall in response to traumatic brain injury," *Microvascular Research,* vol. 60, pp. 55-69, 2000.

[11] R. D. Bukoski, S. N. Wang, K. Bian, and D. S. DeWitt, "Traumatic brain injury does not alter cerebral artery contractility," *The American Journal of Physiology,* vol. 272, pp. H1406-11, Mar 1997.

[12] E. M. Golding, C. F. Contant, Jr., C. S. Robertson, and R. M. Bryan, Jr., "Temporal effect of severe controlled cortical impact injury in the rat on the myogenic response of the middle cerebral artery," *Journal of Neurotrauma,* vol. 15, pp. 973-84, Nov 1998.

[13] E. M. Golding, M. L. Steenberg, L. Cherian, S. P. Marrelli, C. S. Robertson, and R. M. Bryan, "Endothelial-mediated dilations following severe controlled cortical impact injury in the rat middle cerebral artery," *Journal of Neurotrauma,* vol. 15, pp. 635-44, 1998.

[14] E. M. Golding, M. L. Steenberg, C. F. Contant, Jr., I. Krishnappa, C. S. Robertson, and R. M. Bryan, Jr., "Cerebrovascular reactivity to CO(2) and hypotension after mild cortical impact injury," *The American Journal of Physiology,* vol. 277, pp. H1457-66, Oct 1999.

[15] B. P. Mathew, D. S. DeWitt, R. M. Bryan, R. D. Bukoski, and D. S. Prough, "Traumatic brain injury reduces myogenic responses in pressurized rodent middle cerebral arteries," *Journal of Neurotrauma,* vol. 16, pp. 1177-86, 1999.

[16] D. Mohan and J. Melvin, "Failure properties of passive human aortic tissue, I-uniaxial tension tests," *Journal of Biomechanics,* vol. 15, pp. 887-902, 1982.

[17] W. N. Hardy, M. J. Mason, C. D. Foster, C. S. Shah, J. M. Kopacz, K. H. Yang, A. I. King, J. Bishop, M. Bey, W. Anderst, and S. Tashman, "A study of the response of the human cadaver head to impact," *Stapp Car Crash Journal,* vol. 51, pp. 17-80, 2007.

[18] B. Morrison, K. E. Saatman, D. F. Meaney, and T. K. McIntosh, "In vitro central nervous system models of mechanically induced trauma: A review," *Journal of Neurotrauma,* vol. 15, pp. 911-28, 1998.

[19] J. Chalupnik, C. Daly, and H. Merchant, "Material properties of cerebral blood vessels," Technical Report, University of Washington, Seattle, WA, 1971.

[20] M. C. Lee and R. C. Haut, "Insensitivity of tensile failure properties of human bridging veins to strain rate: Implications in biomechanics of subdural hematoma," *Journal of Biomechanics,* vol. 22, pp. 537-42, 1989.

[21] P. Lowenhielm, "Dynamic properties of the parasagittal bridging veins," *Journal of Legal Medicine,* vol. 74, pp. 55-62, 1974.

[22] A. I. R. Maas, N. Stocchetti, and R. Bullock, "Moderate and severe traumatic brain injury in adults," *The Lancet Neurology,* vol. 7, pp. 728-741, 2008.

[23] K. L. Monson, W. Goldsmith, N. M. Barbaro, and G. T. Manley, "Axial mechanical properties of fresh human cerebral blood vessels," *Journal of Biomechanical Engineering,* vol. 125, pp. 288-294, 2003.

[24] S. B. Lewis, J. W. Finnie, P. C. Blumbergs, G. Scott, J. I. M. Manavis, C. Brown, P. L. Reilly, N. R. Jones, and A. J. McLean, "A head impact model of early axonal injury in the sheep," *Journal of Neurotrauma,* vol. 13, pp. 505-514, 1996.

[25] A. C. Grimmelt, S. Eitzen, I. Balakhadze, B. Fischer, J. Wölfer, H. Schiffbauer, A. Gorji, and C. Greiner, "Closed traumatic brain injury model in sheep mimicking high-velocity, closed head trauma in humans," *Central European Neurosurgery,* vol. 72, pp. 120-26, 2011.

[26] H. M. Duvernoy, S. Delon, and J. L. Vannson, "Cortical blood vessels of the human brain," *Brain Research Bulletin,* vol. 7, pp. 519-79, Nov 1981.

[27] H. Nonaka, M. Akima, T. Nagayama, T. Hatori, Z. Zhang, and F. Ihara, "Microvasculature of the human cerebral meninges," *Neuropathology,* vol. 23, pp. 129-35, Jun 2003.

[28] M. Akima, H. Nonaka, M. Kagesawa, and K. Tanaka, "A study on the microvasculature of the cerebral cortex. Fundamental architecture and its senile change in the frontal cortex," *Laboratory Investigation,* vol. 55, pp. 482-9, Oct 1986.

[29] F. Reina-De La Torre, A. Rodriguez-Baeza, and J. Sahuquillo-Barris, "Morphological characteristics and distribution pattern of the arterial vessels in human cerebral cortex: A scanning electron microscope study," *The Anatomical Record,* vol. 251, pp. 87-96, May 1998.

[30] F. Cassot, F. Lauwers, C. Fouard, S. Prohaska, and V. Lauwers-Cances, "A novel three-dimensional computer-assisted method for a quantitative study of microvascular networks of the human cerebral cortex," *Microcirculation,* vol. 13, pp. 1-18, Jan 2006.

[31] F. Cassot, F. Lauwers, S. Lorthois, P. Puwanarajah, V. Cances-Lauwers, and H. Duvernoy, "Branching patterns for arterioles and venules of the human cerebral cortex," *Brain Research,* vol. 1313, pp. 62-78, Feb 8 2010.

[32] M. J. Cipolla, "The cerebral circulation," in *Integrated systems physiology: From molecule to function,* vol. 1, pp. 1-59, 2009.

[33] J. A. G. Rhodin, "Architecture of the vessel wall," in *Handbook of physiology, the cardiovascular system*. vol. 2, D. F. Bohr, A. D. Somlyo, and H. V. Sparks, Eds., Bethesda: American Physiological Society, 1980, pp. 1-31.

[34] J. D. Humphrey, *Cardiovascular solid mechanics: Cells, tissues, and organs*. New York: Springer, 2002.

[35] A. G. Monea, K. Baeck, E. Verbeken, I. Verpoest, J. V. Sloten, J. Goffin, and B. Depreitere, "The biomechanical behaviour of the bridging vein-superior sagittal sinus complex with implications for the mechanopathology of acute subdural haematoma," *Journal of the Mechanical Behavior of Biomedical Materials,* vol. 32c, pp. 155-65, Jan 4 2014.

[36] P. B. Canham, H. M. Finlay, J. G. Dixon, D. R. Boughner, and A. Chen, "Measurements from light and polarised light microscopy of human coronary arteries fixed at distending pressure," *Cardiovascular Research,* vol. 23, pp. 973-82, 1989.

[37] H. Finlay, L. McCullough, and P. Canham, "Three-dimensional collagen organization of human brain arteries at different transmural pressures," *Journal of Vascular Research,* vol. 32, pp. 301-12, 1995.

[38] T. C. Gasser, R. W. Ogden, and G. A. Holzapfel, "Hyperelastic modelling of arterial layers with distributed collagen fibre orientations," *Journal of the Royal Society Interface,* vol. 3, pp. 15-35, 2006.

[39] B. D. Stemper, N. Yoganandan, and F. A. Pintar, "Mechanics of arterial subfailure with increasing loading rate," *Journal of Biomechanics,* vol. 40, pp. 1806-12, 2007.

[40] K. L. Monson, "Mechanical and failure properties of human cerebral blood vessels," Ph.D, dissertation, Department of Mechanical Engineering, University of California Berkeley, 2001.

[41] M. M. Panjabi, E. Yoldas, T. R. Oxland, and J. J. Crisco III, "Subfailure injury of the rabbit anterior cruciate ligament," *Journal of Orthopaedic Research,* vol. 14, pp. 216-22, 1996.

[42] P. P. Provenzano, D. Heisey, K. Hayashi, R. Lakes, and R. Vanderby, "Subfailure damage in ligament: A structural and cellular evaluation," *Journal of Applied Physiology,* vol. 92, pp. 362-71, 2002.

[43] K. P. Quinn, K. E. Lee, C. C. Ahaghotu, and B. A. Winkelstein, "Structural changes in the cervical facet capsular ligament: Potential contributions to pain following subfailure loading," *Stapp Car Crash Journal,* vol. 51, pp. 169-87, 2007.

[44] S. Duenwald-Kuehl, J. Kondratko, R. S. Lakes, and R. Vanderby, "Damage mechanics of porcine flexor tendon: Mechanical evaluation and modeling," *Annals of Biomedical Engineering,* vol. 40, pp. 1-16, 2012.

[45] M. M. Panjabi and T. W. Courtney, "High-speed subfailure stretch of rabbit anterior cruciate ligament: Changes in elastic, failure and viscoelastic characteristics," *Clinical Biomechanics,* vol. 16, pp. 334-40, 2001.

[46] M. M. Panjabi, P. Moy, T. R. Oxland, and J. Cholewicki, "Subfailure injury affects the relaxation behavior of rabbit ACL," *Clinical Biomechanics,* vol. 14, pp. 24-31, 1999.

[47] B. D. Stemper, N. Yoganandan, G. P. Sinson, T. A. Gennarelli, M. R. Stineman, and F. A. Pintar, "Biomechanical characterization of internal layer subfailure in blunt arterial injury," *Annals of Biomedical Engineering,* vol. 35, pp. 285-91, 2007.

[48] B. D. Stemper, N. Yoganandan, and F. A. Pintar, "Mechanics of arterial subfailure with increasing loading rate," *Journal of Biomechanics,* vol. 40, pp. 1806-12, 2007.

[49] B. D. Stemper, N. Yoganandan, F. A. Pintar, and K. J. Brasel, "Multiple subfailures characterize blunt aortic injury," *The Journal of Trauma and Acute Care Surgery,* vol. 62, pp. 1171-4, 2007.

[50] N. Austin, L. M. DiFrancesco, and W. Herzog, "Microstructural damage in arterial tissue exposed to repeated tensile strains," *Journal of Manipulative and Physiological Therapeutics,* vol. 33, pp. 14-19, 2010.

[51] L. Yahia, J. Brunet, S. Labelle, and C. Rivard, "A scanning electron microscopic study of rabbit ligaments under strain," *Matrix (Stuttgart, Germany),* vol. 10, pp. 58-64, 1990.

[52] S. M. Arribas, C. J. Daly, M. C. González, and J. C. McGrath, "Imaging the vascular wall using confocal microscopy," *The Journal of Physiology,* vol. 584, pp. 5-9, 2007.

[53] G. A. Holzapfel, T. C. Gasser, and R. W. Ogden, "A new constitutive framework for arterial wall mechanics and a comparative study of material models," *Journal of Elasticity,* vol. 61, pp. 1-48, 2000.

[54] J. M. Clark and S. Glagov, "Transmural organization of the arterial media. The lamellar unit revisited," *Arteriosclerosis, Thrombosis, and Vascular Biology,* vol. 5, pp. 19-34, 1985.

[55] M. Faul, L. Xu, M. M. Wald, and V. G. Coronado, "Traumatic brain injury in the United States: Emergency department visits, hospitalizations and deaths 2002-2006," Centers for Disease Control and Prevention, National Center for Injury Prevention and Control, Atlanta, GA, 2010.

[56] W. M. Armstead, "Cerebral hemodynamics after traumatic brain injury of immature brain," *Experimental and Toxicologic Pathology,* vol. 51, pp. 137-42, Feb 1999.

[57] E. D. Bell, J. W. Sullivan, and K. L. Monson, "Subfailure overstretch induces persistent changes in the passive mechanical response of cerebral arteries," *Frontiers in Bioengineering and Biotechnology,* vol. 3, 2015.

[58] L. Horný, E. Gultova, H. Chlup, R. Sedlacek, J. Kronek, J. Veselý, and R. Žitný, "Mullins effect in aorta and limiting extensibility evolution," *Bulletin of Applied Mechanics,* vol. 6, pp. 1-5, 2010.

[59] E. Maher, A. Creane, C. Lally, and D. J. Kelly, "An anisotropic inelastic constitutive model to describe stress softening and permanent deformation in arterial tissue," *Journal of the Mechanical Behavior of Biomedical Materials,* vol. 12, pp. 9-19, 2012.

[60] H. Weisbecker, D. M. Pierce, P. Regitnig, and G. A. Holzapfel, "Layer-specific damage experiments and modeling of human thoracic and abdominal aortas with non-atherosclerotic intimal thickening," *Journal of the Mechanical Behavior of Biomedical Materials,* vol. 12, pp. 93-106, 2012.

[61] H. S. Oktay, "Continuum damage mechanics of balloon angioplasty," Ph.D. dissertation, Department of Mechanical Engineering, University of Maryland, Baltimore, MD, 1993.

[62] H. Weisbecker, C. Viertler, D. M. Pierce, and G. A. Holzapfel, "The role of elastin and collagen in the softening behavior of the human thoracic aortic media," *Journal of Biomechanics,* vol. 46, pp. 1859-65, 2013.

[63] R. G. Pollock, V. M. Wang, J. S. Bucchieri, N. P. Cohen, C.-Y. Huang, R. J. Pawluk, E. L. Flatow, L. U. Bigliani, and V. C. Mow, "Effects of repetitive subfailure strains on the mechanical behavior of the inferior glenohumeral ligament," *Journal of Shoulder and Elbow Surgery,* vol. 9, pp. 427-35, 2000.

[64] S. E. Duenwald, R. Vanderby, and R. S. Lakes, "Viscoelastic relaxation and recovery of tendon," *Annals of Biomedical Engineering,* vol. 37, pp. 1131-40, 2009.

[65] H. Gregersen, J. Emery, and A. McCulloch, "History-dependent mechanical behavior of guinea-pig small intestine," *Annals of Biomedical Engineering,* vol. 26, pp. 850-8, 1998.

[66] J. Emery, J. Omens, and A. McCulloch, "Strain softening in rat left ventricular myocardium," *Journal of Biomechanical Engineering,* vol. 119, pp. 6-12, 1997.

[67] E. D. Bell, A. J. Donato, and K. L. Monson, "Cerebrovascular dysfunction following subfailure axial stretch," *Journal of the Mechanical Behavior of Biomedical Materials,* vol. 65, pp. 627-633, 2017.

[68] K. L. Monson, N. M. Barbaro, and G. T. Manley, "Biaxial response of passive human cerebral arteries," *Annals of Biomedical Engineering,* vol. 36, pp. 2028-41, 2008.

[69] E. D. Bell, R. S. Kunjir, and K. L. Monson, "Biaxial and failure properties of passive rat middle cerebral arteries," *Journal of Biomechanics,* vol. 46, pp. 91-6, 2013.

[70] J. D. Humphrey, "Mechanics of the arterial wall: Review and directions," *Critical Reviews in Biomedical Engineering*, vol. 23, pp. 1-162, 1995.

[71] P. Van Loon, "Length-force and volume-pressure relationships of arteries," *Biorheology*, vol. 14, pp. 181-201, 1977.

[72] K. L. Monson, V. Mathur, and D. A. Powell, "Deformations and end effects in isolated blood vessel testing," *Journal of Biomechanical Engineering*, vol. 133, p. 011005, Jan 2011.

[73] B. K. Wicker, H. P. Hutchens, Q. Wu, A. T. Yeh, and J. D. Humphrey, "Normal basilar artery structure and biaxial mechanical behaviour," *Computer Methods in Biomechanics and Biomedical Engineering*, vol. 11, pp. 539-51, Oct 2008.

[74] B. Wicker, H. Hutchens, Q. Wu, A. Yeh, and J. Humphrey, "Normal basilar artery structure and biaxial mechanical behaviour," *Computer Methods in Biomechanics and Biomedical Engineering*, vol. 11, pp. 539-551, 2008.

[75] M. R. Roach and A. C. Burton, "The reason for the shape of the distensibility curves of arteries," *Canadian Journal of Biochemistry and Physiology*, vol. 35, pp. 681-690, 1957.

[76] J. J. Hu, A. Ambrus, T. W. Fossum, M. W. Miller, J. D. Humphrey, and E. Wilson, "Time courses of growth and remodeling of porcine aortic media during hypertension: A quantitative immunohistochemical examination," *Journal of Histochemistry & Cytochemistry*, vol. 56, pp. 359-70, 2008.

[77] A. Jamal, M. Bendeck, and B. Langille, "Structural changes and recovery of function after arterial injury," *Arteriosclerosis, Thrombosis, and Vascular Biology*, vol. 12, pp. 307-17, 1992.

[78] R. Ogden and D. Roxburgh, "A pseudo–elastic model for the Mullins effect in filled rubber," in *Proceedings of the Royal Society of London A: Mathematical, Physical and Engineering Sciences*, 1999, pp. 2861-77.

[79] S. Margulies, L. Thibault, and T. Gennarelli, "Physical model simulations of brain injury in the primate," *Journal of Biomechanics*, vol. 23, pp. 823-36, 1990.

[80] D. F. Meaney and L. E. Thibault, "Physical model studies of cortical brain deformation in response to high strain rate inertial loading," in *International IRCOBI Conference on the Biomechanics of Impacts*, pp. 215-24, 1990.

[81] M. Ohkawa, N. Fujiwara, M. Tanabe, H. Takashima, K. Satoh, K. Kojima, K. Irie, Y. Honjo, and S. Nagao, "Cerebral vasospastic vessels: Histologic changes after percutaneous transluminal angioplasty," *Radiology*, vol. 198, pp. 179-84, 1996.

[82] W. Castaneda-Zuniga, A. Formanek, M. Tadavarthy, Z. Vlodaver, J. Edwards, C. Zollikofer, and K. Amplatz, "The mechanism of balloon angioplasty," *Radiology,* vol. 135, pp. 565-71, 1980.

[83] G. L. Wolf, R. F. LeVeen, and E. J. Ring, "Potential mechanisms of angioplasty," *Cardiovascular and Interventional Radiology,* vol. 7, pp. 11-17, 1984.

[84] P. D. Chan, J. M. Findlay, B. Vollrath, D. A. Cook, M. Grace, M. H. Chen, and R. A. Ashforth, "Pharmacological and morphological effects of in vitro transluminal balloon angioplasty on normal and vasospastic canine basilar arteries," *Journal of Neurosurgery,* vol. 83, pp. 522-530, 1995.

[85] T. C. Gasser and G. A. Holzapfel, "A rate-independent elastoplastic constitutive model for biological fiber-reinforced composites at finite strains: Continuum basis, algorithmic formulation and finite element implementation," *Computational Mechanics,* vol. 29, pp. 340-60, 2002.

[86] J. D. Humphrey, E. R. Dufresne, and M. A. Schwartz, "Mechanotransduction and extracellular matrix homeostasis," *Nature Reviews Molecular Cell Biology,* vol. 15, pp. 802-12, 2014.

[87] C. Zollikofer, E. Salomonowitz, R. Sibley, J. Chain, W. Bruehlmann, W. Castaneda-Zuniga, and K. Amplatz, "Transluminal angioplasty evaluated by electron microscopy," *Radiology,* vol. 153, pp. 369-74, 1984.

[88] Y. Zubkov, V. Semenutin, G. Benashvili, and J. Findlay, "Cerebral blood flow following angioplasty for vasospasm," *Cerebral Vasospasm Conference.* pp. 325-7, 1993.

[89] Y. Yamamoto, R. R. Smith, and D. H. Bernanke, "Mechanism of action of balloon angioplasty in cerebral vasospasm," *Neurosurgery,* vol. 30, pp. 1-6, 1992.

[90] Y. Li, C. A. Foss, D. D. Summerfield, J. J. Doyle, C. M. Torok, H. C. Dietz, M. G. Pomper, and S. M. Yu, "Targeting collagen strands by photo-triggered triple-helix hybridization," *Proceedings of the National Academy of Sciences,* vol. 109, pp. 14767-72, 2012.

[91] Y. Li and S. M. Yu, "Targeting and mimicking collagens via triple helical peptide assembly," *Current Opinion in Chemical Biology,* vol. 17, pp. 968-75, 2013.

[92] J. L. Zitnay, Y. Li, Z. Qin, B. H. San, B. Depalle, S. P. Reese, M. J. Buehler, S. M. Yu, and J. A. Weiss, "Molecular level detection and localization of mechanical damage in collagen enabled by collagen hybridizing peptides," *Nature Communications,* vol. 8, p. 14913, 2017.

[93] Y. Li, D. Ho, H. Meng, T. R. Chan, B. An, H. Yu, B. Brodsky, A. S. Jun, and S. M. Yu, "Direct detection of collagenous proteins by fluorescently labeled collagen mimetic peptides," *Bioconjugate Chemistry,* vol. 24, pp. 9, 2013.

[94] J. Hwang, Y. Huang, T. J. Burwell, N. C. Peterson, J. Connor, S. J. Weiss, S. M. Yu, and Y. Li, "In situ imaging of tissue remodeling with collagen hybridizing peptides," *ACS Nano,* vol. 11, pp. 9825-35, 2017.

[95] T. L. Willett, R. S. Labow, N. C. Avery, and J. M. Lee, "Increased proteolysis of collagen in an in vitro tensile overload tendon model," *Annals of Biomedical Engineering,* vol. 35, pp. 1961-72, 2007.

[96] T. L. Willett, R. S. Labow, and J. M. Lee, "Mechanical overload decreases the thermal stability of collagen in an in vitro tensile overload tendon model," *Journal of Orthopaedic Research,* vol. 26, pp. 1605-10, 2008.

[97] S. P. Veres and J. M. Lee, "Designed to fail: A novel mode of collagen fibril disruption and its relevance to tissue toughness," *Biophysical Journal,* vol. 102, pp. 2876-84, 2012.

[98] S. P. Veres, J. M. Harrison, and J. M. Lee, "Mechanically overloading collagen fibrils uncoils collagen molecules, placing them in a stable, denatured state," *Matrix Biology,* vol. 33, pp. 54-9, 2014.

[99] P. Van Loon, "Length-force and volume-pressure relationships of arteries," *Biorheology,* vol. 14, pp. 181-201, 1976.

[100] K. S. Nye, M. I. Converse, M. J. Dahl, K. H. Albertine, and K. L. Monson, "Development of mechanical and failure properties in sheep cerebral arteries," *Annals of Biomedical Engineering,* vol. 45, pp. 1-10, 2016.

[101] S. S. Nandikar, M. Converse, and K. Monson, "Computational characterization of blood vessel strain in wire myography," presented at the Biomedical Engineering Western Regional Conference, Salt Lake City, UT, 2017.

[102] R. Rezakhaniha, A. Agianniotis, J. T. Schrauwen, A. Griffa, D. Sage, C. V. Bouten, F. Van de Vosse, M. Unser, and N. Stergiopulos, "Experimental investigation of collagen waviness and orientation in the arterial adventitia using confocal laser scanning microscopy," *Biomechanics and Modeling in Mechanobiology,* vol. 11, pp. 461-473, 2012.

[103] W. C. Navidi, *Statistics for engineers and scientists*. New York: McGraw-Hill, 2006.

[104] K. S. Nye, "Age-related changes in the mechanical properties of arteries," M.S. thesis, Department of Mechanical Engineering, University of Utah, Salt Lake City, UT, 2015.

[105] SAE, "Instrumentation for impact testing," in *Part 1: Electronic Instrumentation, SAE J211-1*, Warrendale, PA, 1995.

[106] J. D. Humphrey, "Mechanics of the arterial wall: Review and directions," *Critical Reviews in Biomedical Engineering*, vol. 23, pp. 1-162, 1994.

[107] P. Fratzl, *Collagen: Structure and mechanics*. New York: Springer Science & Business Media, 2008.

[108] H. M. Finlay, L. McCullough, and P. B. Canham, "Three-dimensional collagen organization of human brain arteries at different transmural pressures," *Journal of Vascular Research*, vol. 32, pp. 301-12, 1995.

[109] A. G. Monea, K. Baeck, E. Verbeken, I. Verpoest, J. Vander Sloten, J. Goffin, and B. Depreitere, "The biomechanical behaviour of the bridging vein–superior sagittal sinus complex with implications for the mechanopathology of acute subdural haematoma," *Journal of the Mechanical Behavior of Biomedical Materials*, vol. 32, pp. 155-65, 2014.

[110] J. M. Peloquin, M. H. Santare, and D. M. Elliott, "Advances in quantification of meniscus tensile mechanics including nonlinearity, yield, and failure," *Journal of Biomechanical Engineering*, vol. 138, p. 021002, 2016.

[111] K. A. Derwin and L. Soslowsky, "A quantitative investigation of structure-function relationships in a tendon fascicle model," *Journal of Biomechanical Engineering*, vol. 121, pp. 598-604, 1999.

[112] K. L. Goh, D. Holmes, Y. Lu, P. P. Purslow, K. Kadler, D. Béchet, and T. J. Wess, "Bimodal collagen fibril diameter distributions direct age-related variations in tendon resilience and resistance to rupture," *Journal of Applied Physiology*, vol. 113, pp. 878-88, 2012.

[113] K. P. Quinn and B. A. Winkelstein, "Cervical facet capsular ligament yield defines the threshold for injury and persistent joint-mediated neck pain," *Journal of Biomechanics*, vol. 40, pp. 2299-2306, 2007.

[114] M. M. Murray, E. Magarian, D. Zurakowski, and B. C. Fleming, "Bone-to-bone fixation enhances functional healing of the porcine anterior cruciate ligament using a collagen-platelet composite," *Arthroscopy: The Journal of Arthroscopic & Related Surgery*, vol. 26, pp. S49-S57, 2010.

[115] G. A. Holzapfel, "Biomechanics of soft tissue," in *The Handbook of Materials Behavior Models*, vol. 3, pp. 1049-63, 2001.

[116] J. D. Humphrey, *Cardiovascular solid mechanics: Cells, tissues, and organs*. New York: Springer Science & Business Media, 2002.

[117] G. A. Holzapfel, C. A. Schulze-Bauer, and M. Stadler, "Mechanics of angioplasty: Wall, balloon and stent," *ASME Applied Mechanics Division-Publications-AMD*, vol. 242, pp. 141-56, 2000.

[118] A. J. Schriefl, T. Schmidt, D. Balzani, G. Sommer, and G. A. Holzapfel, "Selective enzymatic removal of elastin and collagen from human abdominal aortas: Uniaxial mechanical response and constitutive modeling," *Acta Biomaterialia*, vol. 17, pp. 125-36, 2015.

[119] K. P. Quinn and B. A. Winkelstein, "Preconditioning is correlated with altered collagen fiber alignment in ligament," *Journal of Biomechanical Engineering*, vol. 133, p. 064506, 2011.

[120] R. Krams and M. Bäck, *ESC textbook of vascular biology*. New York: Oxford University Press, 2017.

[121] Y. H. Chen, J. H. Kang, and H. C. Lin, "Patients with traumatic brain injury: Population-based study suggests increased risk of stroke," *Stroke*, vol. 42, pp. 2733-9, October 2011.

[122] J. F. Burke, J. L. Stulc, L. E. Skolarus, E. D. Sears, D. B. Zahuranec, and L. B. Morgenstern, "Traumatic brain injury may be an independent risk factor for stroke," *Neurology*, vol. 81, pp. 33-9, July 2013.

[123] C. W. Sliker, "Blunt cerebrovascular injuries: Imaging with multidetector CT angiography," *Radiographics*, vol. 28, pp. 1689-1708, 2008.

[124] B. D. Stemper, N. Yoganandan, and F. A. Pintar, "Methodology to study intimal failure mechanics in human internal carotid arteries," *Journal of Biomechanics*, vol. 38, pp. 2491-6, 2005.

[125] B. D. Stemper, N. Yoganandan, G. P. Sinson, T. A. Gennarelli, M. R. Stineman, and F. A. Pintar, "Biomechanical characterization of internal layer subfailure in blunt arterial injury," *Annals of Biomedical Engineering*, vol. 35, pp. 285-91, Feb 2007.

[126] L. Chàvez, A. Takahashi, T. Yoshimoto, C. C. Su, T. Sugawara, and Y. Fujii, "Morphological changes in normal canine basilar arteries after transluminal angioplasty," *Neurological Research*, vol. 12, pp. 12-6, 1990.

[127] J. L. Steenhuijsen, S. R. Vaartjes, C. J. Poortermans, M. G. Havenith, and H. B. Boom, "Rupture of the arterial wall causes deflection in pressure time course during ex vivo balloon angioplasty," *Catheterization and Cardiovascular Diagnosis*, vol. 42, pp. 92-101, 1997.

[128] Y. C. Fung, *Biomechanics*. New York: Springer Science & Business Media,1993.

[129] B. Starcher, "Elastin and the lung," *Thorax*, vol. 41, p. 577, 1986.

[130] S. Shapiro, S. Endicott, M. Province, J. Pierce, and E. Campbell, "Marked longevity of human lung parenchymal elastic fibers deduced from prevalence of D-aspartate

and nuclear weapons-related radiocarbon," *Journal of Clinical Investigation,* vol. 87, p. 1828, 1991.

[131] M. A. Dubick, R. B. Rucker, C. E. Cross, and J. A. Last, "Elastin metabolism in rodent lung," *Biochimica et Biophysica Acta (BBA)-General Subjects,* vol. 672, pp. 303-6, 1981.

[132] F. Keeley, "The synthesis of soluble and insoluble elastin in chicken aorta as a function of development and age. Effect of a high cholesterol diet," *Canadian Journal of Biochemistry,* vol. 57, pp. 1273-80, 1979.

[133] J. E. Wagenseil and R. P. Mecham, "Vascular extracellular matrix and arterial mechanics," *Physiological Reviews,* vol. 89, pp. 957-89, 2009.

[134] S. L. Sandow, D. J. Gzik, and R. M. Lee, "Arterial internal elastic lamina holes: Relationship to function?," *Journal of Anatomy,* vol. 214, pp. 258-66, 2009.

[135] K. Hutchison and E. Sanders, "Patterns of internal elastic lamina morphology in the canine common carotid artery," *Journal of Vascular Research,* vol. 27, pp. 1-13, 1990.

[136] M. J. Osborne-Pellegrin, "Spontaneous arterial lesions involving breaks in the internal elastic lamina in the rat: Effects of β-aminopropionitrile and familial distribution," *Experimental and Molecular Pathology,* vol. 45, pp. 171-184, 1986.

[137] S. L. Sandow, M. Tare, H. A. Coleman, C. E. Hill, and H. C. Parkington, "Involvement of myoendothelial gap junctions in the actions of endothelium-derived hyperpolarizing factor," *Circulation Research,* vol. 90, pp. 1108-13, 2002.

[138] C. de Wit, B. Hoepfl, and S. E. Wölfle, "Endothelial mediators and communication through vascular gap junctions," *Biological Chemistry,* vol. 387, pp. 3-9, 2006.

[139] S. L. Sandow and M. Tare, "C-type natriuretic peptide: A new endothelium-derived hyperpolarizing factor?," *Trends in Pharmacological Sciences,* vol. 28, pp. 61-7, 2007.

[140] E. B. Smith and E. M. Staples, "Distribution of plasma proteins across the human aortic wall: Barrier functions of endothelium and internal elastic lamina," *Atherosclerosis,* vol. 37, pp. 579-90, 1980.

[141] S. Nyström, "Development of intracranial aneurysms as revealed by electron microscopy," *Journal of Neurosurgery,* vol. 20, pp. 329-37, 1963.

[142] E. R. Lang and M. Kidd, "Electron microscopy of human cerebral aneurysms," *Journal of Neurosurgery,* vol. 22, pp. 554-62, 1965.

[143] S. Cajander and O. Hassler, "Enzymatic destruction of the elastic lamella at the mouth of cerebral berry aneurysm?," *Acta Neurologica Scandinavica,* vol. 53, pp. 171-81, 1976.

[144] W. E. Stehbens, "Histopathology of cerebral aneurysms," *Archives of Neurology,* vol. 8, pp. 272-85, 1963.

[145] W. E. Stehbens, "Ultrastructure of aneurysms," *Archives of Neurology,* vol. 32, pp. 798-807, 1975.

[146] G. Campbell and M. Roach, "Fenestrations in the internal elastic lamina at bifurcations of human cerebral arteries," *Stroke,* vol. 12, pp. 489-96, 1981.

[147] C. Zollikofer, J. Chain, E. Salomonowitz, W. Runge, W. Bruehlmann, W. Castaneda-Zuniga, and K. Amplatz, "Percutaneous transluminal angioplasty of the aorta. Light and electron microscopic observations in normal and atherosclerotic rabbits," *Radiology,* vol. 151, pp. 355-63, 1984.

[148] L. A. Harker, "Role of platelets and thrombosis in mechanisms of acute occlusion and restenosis after angioplasty," *The American Journal of Cardiology,* vol. 60, pp. 20-8, 1987.

[149] R. F. LeVeen, G. L. Wolf, and D. Biery, "Angioplasty-induced vasospasm in rabbit model: Mechanisms and treatment," *Investigative Radiology,* vol. 20, pp. 938-44, 1985.

[150] R. Ross and J. A. Glomset, "Atherosclerosis and the arterial smooth muscle cell," *Science,* vol. 180, pp. 1332-9, 1973.

[151] R. DePalma, "Atherosclerosis in vascular grafts," *Atherosclerosis Review,* vol. 6, pp. 147-77, 1979.

[152] W. Lee and K. Lee, "Advanced coronary atherosclerosis in swine produced by combination of balloon-catheter injury and cholesterol feeding," *Experimental and Molecular Pathology,* vol. 23, pp. 491-9, 1975.

[153] R. Scott, H. Imai, T. Makita, W. Thomas, and J. Reiner, "Lining cell and intimal smooth muscle cell response and Evans blue staining in abdominal aorta of young swine after denudation by balloon catheter," *Experimental and Molecular Pathology,* vol. 33, pp. 185-202, 1980.

[154] P. M. Steele, J. H. Chesebro, A. W. Stanson, D. R. Holmes, M. K. Dewanjee, L. Badimon, and V. Fuster, "Balloon angioplasty. Natural history of the pathophysiological response to injury in a pig model," *Circulation Research,* vol. 57, pp. 105-12, 1985.

[155] E. Pozzati, G. Giuliani, M. Poppi, and A. Faenza, "Blunt traumatic carotid dissection with delayed symptoms," *Stroke,* vol. 20, pp. 412-6, 1989.

[156] K. L. Monson, V. Mathur, and D. A. Powell, "Deformations and end effects in isolated blood vessel testing," *Journal of Biomechanical Engineering,* vol. 133, p. 011005, 2011.

[157] A. I. King, K. H. Yang, and W. N. Hardy, "Recent firsts in cadaveric impact biomechanics research," *Clinical Anatomy,* vol. 24, pp. 294-308, Apr 2011.

[158] W. N. Hardy, C. D. Foster, M. J. Mason, K. H. Yang, A. I. King, and C. Tashman, "Investigation of head injury mechanisms using neutral density technology and high-speed biplanar x-ray," *Stapp Car Crash Journal,* vol. 45, pp. 337-68, 2001.

[159] L. Zhang, K. H. Yang, R. Dwarampudi, K. Omori, T. Li, K. Chang, W. N. Hardy, T. B. Khalil, and A. I. King, "Recent advances in brain injury research: A new human head model development and validation," *Stapp Car Crash Journal,* vol. 45, 2001.

[160] E. G. Takhounts, R. H. Eppinger, J. Q. Campbell, R. E. Tannous, E. D. Power, and L. S. Shook, "On the development of the SIMon finite element head model," *Stapp Car Crash Journal,* vol. 47, pp. 107-33, Oct 2003.

[161] S. Kleiven, "Influence of impact direction on the human head in prediction of subdural hematoma," *Journal of Neurotrauma,* vol. 20, pp. 365-79, Apr 2003.

[162] T. R. Fenton, W. G. Gibson, and J. R. Taylor, "Stress analysis of vasoconstriction at arterial branch sites," *Journal of Biomechanics,* vol. 19, pp. 501-9, 1986.

[163] M. J. Thubrikar, S. K. Roskelley, and R. T. Eppink, "Study of stress concentration in the walls of the bovine coronary arterial branch," *Journal of Biomechanics,* vol. 23, pp. 15-26, 1990.

[164] T. W. MacFarlane, M. R. Roach, and K. Chan, "The geometry of human cerebral bifurcations: Effect of static distending pressure," *Journal of Biomechanics,* vol. 13, pp. 265-77, 1980.

[165] M. R. Roach, "The structure and elastic properties of arterial junctions," *Connective Tissue Research,* vol. 15, pp. 77-84, 1986.

[166] A. J. Rowe, H. M. Finlay, and P. B. Canham, "Collagen biomechanics in cerebral arteries and bifurcations assessed by polarizing microscopy," *Journal of Vascular Research,* vol. 40, pp. 406-15, Jul-Aug 2003.

[167] H. M. Finlay, P. Whittaker, and P. B. Canham, "Collagen organization in the branching region of human brain arteries," *Stroke,* vol. 29, pp. 1595-601, Aug 1998.

[168] A. Takahashi, T. Ushiki, K. Abe, K. Houkin, and H. Abe, "Scanning electron microscopic studies of the medial smooth muscles in human major intracranial arteries," *Archives of Histology and Cytology,* vol. 57, pp. 341-350, Oct 1994.

[169] J. Walmsley, M. Campling, and H. Chertkow, "Interrelationships among wall structure, smooth muscle orientation, and contraction in human major cerebral arteries," *Stroke,* vol. 14, pp. 781-90, 1983.

[170] T. Shiraishi, S. Sakaki, and Y. Uehara, "Architecture of the medial smooth muscle of the arterial vessels in the normal human brain: A scanning electron-microscopic study," *Scanning Microscopy,* vol. 4, pp. 191-9, Mar 1990.

[171] H. D. Stubbe, C. Greiner, H. Van Aken, C. H. Rickert, M. Westphal, H. Wassmann, A. Akcocuk, F. Daudel, M. Erren, and F. Hinder, "Cerebral vascular and metabolic response to sustained systemic inflammation in ovine traumatic brain injury," *Journal of Cerebral Blood Flow and Metabolism,* vol. 24, pp. 1400-8, Dec 2004.

[172] R. W. Byard, L. Gabrielian, S. C. Helps, E. Thornton, and R. Vink, "Further investigations into the speed of cerebral swelling following blunt cranial trauma," *Journal of Forensic Sciences,* vol. 57, pp. 973-5, 2012.

[173] C. Van den Heuvel, P. C. Blumbergs, J. W. Finnie, J. Manavis, N. R. Jones, P. L. Reilly, and R. A. Pereira, "Upregulation of amyloid precursor protein messenger RNA in response to traumatic brain injury: An ovine head impact model," *Experimental Neurology,* vol. 159, pp. 441-450, 1999.

[174] R. W. G. Anderson, C. J. Brown, P. C. Blumbergs, A. J. McLean, and N. R. Jones, "Impact mechanics and axonal injury in a sheep model," *Journal of Neurotrauma,* vol. 20, pp. 961-74, 2003.

[175] R. W. Byard, K. D. Bhatia, P. L. Reilly, and R. Vink, "How rapidly does cerebral swelling follow trauma? Observations using an animal model and possible implications in infancy," *Legal Medicine,* vol. 11, pp. S128-S131, 2009.

[176] A. M. Nahum and R. Smith, "Experimental model for closed head impact injury," SAE Technical Paper 760825, 1976.

[177] P. F. van der Meer, B. Tomson, and A. Brand, "In vivo tracking of transfused platelets for recovery and survival studies: An appraisal of labeling methods," *Transfusion and Apheresis Science,* vol. 42, pp. 53-61, 2010.

[178] K. A. Schwartz, "Platelet antibody: Review of detection methods," *American Journal of Hematology,* vol. 29, pp. 106-14, 1988.

[179] D. Balzani, S. Brinkhues, and G. A. Holzapfel, "Constitutive framework for the modeling of damage in collagenous soft tissues with application to arterial walls," *Computer Methods in Applied Mechanics and Engineering,* vol. 213, pp. 139-51, 2012.

[180] E. Peña, J. A. Peña, and M. Doblaré, "On the Mullins effect and hysteresis of fibered biological materials: A comparison between continuous and discontinuous

damage models," *International Journal of Solids and Structures*, vol. 46, pp. 1727-35, 2009.